



Evidence from the H3 Survey That the Stellar Halo Is Entirely Comprised of Substructure

Rohan P. Naidu¹ , Charlie Conroy¹ , Ana Bonaca¹ , Benjamin D. Johnson¹ , Yuan-Sen Ting (丁源森)^{2,3,4,5,7} , Nelson Caldwell¹ , Dennis Zaritsky⁶ , and Phillip A. Cargile¹

¹ Center for Astrophysics, Harvard & Smithsonian, 60 Garden Street, Cambridge, MA 02138, USA; rohan.naidu@cfa.harvard.edu

² Institute for Advanced Study, Princeton, NJ 08540, USA

³ Department of Astrophysical Sciences, Princeton University, Princeton, NJ 08544, USA

⁴ Observatories of the Carnegie Institution of Washington, 813 Santa Barbara Street, Pasadena, CA 91101, USA

⁵ Research School of Astronomy and Astrophysics, Mount Stromlo Observatory, Cotter Road, Weston Creek, ACT 2611, Canberra, Australia

⁶ Steward Observatory, University of Arizona, 933 North Cherry Avenue, Tucson, AZ 85721-0065, USA

Received 2020 June 12; revised 2020 July 28; accepted 2020 August 11; published 2020 September 21

Abstract

In the Λ CDM paradigm, the Galactic stellar halo is predicted to harbor the accreted debris of smaller systems. To identify these systems, the H3 Spectroscopic Survey, combined with Gaia, is gathering 6D phase-space and chemical information in the distant Galaxy. Here we present a comprehensive inventory of structure within 50 kpc from the Galactic center using a sample of 5684 giants at $|b| > 40^\circ$ and $|Z| > 2$ kpc. We identify known structures including the high- α disk, the *in situ* halo (disk stars heated to eccentric orbits), Sagittarius (Sgr), Gaia–Sausage–Enceladus (GSE), the Helmi Streams, Sequoia, and Thamnos. Additionally, we identify the following new structures: (i) Aleph ($[\text{Fe}/\text{H}] = -0.5$), a low-eccentricity structure that rises a surprising 10 kpc off the plane, (ii) and (iii) Arjuna ($[\text{Fe}/\text{H}] = -1.2$) and I’itoi ($[\text{Fe}/\text{H}] < -2$), which comprise the high-energy retrograde halo along with Sequoia, and (iv) Wukong ($[\text{Fe}/\text{H}] = -1.6$), a prograde phase-space overdensity chemically distinct from GSE. For each structure, we provide $[\text{Fe}/\text{H}]$, $[\alpha/\text{Fe}]$, and orbital parameters. Stars born within the Galaxy are a major component at $|Z| \sim 2$ kpc ($\approx 60\%$), but their relative fraction declines sharply to $\lesssim 5\%$ past 15 kpc. Beyond 15 kpc, $> 80\%$ of the halo is built by two massive ($M_* \sim 10^8\text{--}10^9 M_\odot$) accreted dwarfs: GSE ($[\text{Fe}/\text{H}] = -1.2$) within 25 kpc and Sgr ($[\text{Fe}/\text{H}] = -1.0$) beyond 25 kpc. This explains the relatively high overall metallicity of the halo ($[\text{Fe}/\text{H}] \approx -1.2$). We attribute $\gtrsim 95\%$ of the sample to one of the listed structures, pointing to a halo built entirely from accreted dwarfs and heating of the disk.

Unified Astronomy Thesaurus concepts: [Galaxy stellar halos \(598\)](#); [Galaxy kinematics \(602\)](#); [Milky Way evolution \(1052\)](#); [Galaxy evolution \(594\)](#); [Galaxy formation \(595\)](#); [Milky Way formation \(1053\)](#); [Milky Way Galaxy \(1054\)](#); [Milky Way stellar halo \(1060\)](#)

1. Introduction

The Milky Way’s (MW’s) stellar halo comprises only $\sim 1\%$ of its stellar mass (e.g., Deason et al. 2019; Mackereth & Bovy 2020), and yet it is an object of intense interest because it acts as a time capsule, preserving memory of the Galaxy’s assembly history with high fidelity. As early as Woolley (1957, p. 45), it was realized that “the time of relaxation of stellar motions in this part of the galaxy is at least 10^{12} yr, whereas the stars themselves have not existed in their present form for much more than 10^{10} yr.” In detail, halo stars belonging to the same structure, even when they are scattered across the sky, retain similar coordinates in their integrals of motion (e.g., energy, angular momenta, actions). Further, stars belonging to the same structure share similar chemical abundance patterns (e.g., Freeman & Bland-Hawthorn 2002; Venn et al. 2004; Lee et al. 2015). This expected clustering of halo stars in both integrals of motion and chemistry opens the door to “reconstruct the galactic past” (Eggen et al. 1962).

Thanks to large stellar spectroscopic surveys, e.g., RAVE (Steinmetz et al. 2006), SEGUE (Yanny et al. 2009), LAMOST (Cui et al. 2012), GALAH (De Silva et al. 2015), APOGEE (Majewski et al. 2017), and the Gaia mission (Gaia Collaboration et al. 2018), integrals of motion and chemical abundances have become available for millions of stars in the solar neighborhood.

Strikingly, more than half of the $[\text{Fe}/\text{H}] < -1$ stars in the local halo⁸ appear to originate from a single system, the accreted Gaia–Sausage–Enceladus (GSE) dwarf galaxy (e.g., Belokurov et al. 2018; Haywood et al. 2018; Helmi et al. 2018; Koppelman et al. 2018; Myeong et al. 2018b; Mackereth et al. 2019). However, the most substantive component ($\gtrsim 50\%$) of the local halo, the “*in situ* halo”/“Splash,” likely arose from the heating of the primordial high- α disk by early mergers (e.g., Bonaca et al. 2017, 2020; Haywood et al. 2018; Di Matteo et al. 2019; Belokurov et al. 2020).

While the local halo has provided these vital insights into the Galaxy’s assembly, a complete census of accretion events requires going beyond the solar neighborhood. A number of simulations show that debris from minor mergers, higher-mass but recently accreted galaxies, and galaxies accreted along particular inclinations (e.g., at high angular momentum) are underrepresented in the local halo (e.g., Bullock & Johnston 2005; Amorisco 2017; Fattahi et al. 2020; Pfeffer et al. 2020). As a consequence, studies that rely on local high-energy orbits to deduce the nature of the distant halo are biased against these populations. The disrupting Sagittarius dwarf galaxy (e.g., Ibata et al. 1994; Majewski et al. 2003) is a prime

⁸ By “local halo” we mean the portion of the kinematic halo within a few kiloparsecs from the Sun that is typically selected using 3D Galactocentric velocity (e.g., $|V - V_{\text{LSR}}| > 210 \text{ km s}^{-1}$; Helmi et al. 2018) with a view to avoid the disk.

⁷ Hubble Fellow.

example of a massive structure that is completely absent from the local halo.

Fully characterizing the global extent of structures discovered in local samples also demands pushing farther into the halo. Debris from low-mass structures like Thamnos ($M_\star < 5 \times 10^6 M_\odot$, Koppelman et al. 2019a), which is barely discernible in local samples, might be more apparent at larger distances due to “apocenter pile-up” (Deason et al. 2018) or due to higher contrast once the density of GSE and disk-like stars falls off. Studying massive accreted structures like GSE and the Helmi Streams (Helmi et al. 1999)—e.g., the presence/absence of metallicity gradients, robust stellar masses from star counts, if they even are a single contiguous structure—will also become more tractable with samples spanning their full extent.

Ranging beyond the local halo is also necessary to settle long-standing debates about the origin and nature of the halo. Is the halo largely formed in situ or ex situ (e.g., Eggen et al. 1962 versus Searle & Zinn 1978)? To what radius does the recently discovered in situ component of the halo dominate the halo mass function? Some simulations (e.g., Monachesi et al. 2019) show disk stars, heated by mergers, comprising $\sim 20\%$ of the halo even beyond 50 kpc. Consequently, the extent and relative fraction of the in situ halo should provide an independent constraint on the Galaxy’s accretion history (e.g., Zolotov et al. 2009; Purcell et al. 2010). More generally, the fraction of in situ halo stars (not only the heated disk, but also stars formed from stripped gas from satellites or through cosmological accretion) varies widely across simulations, ranging from negligible to comparable to the accreted mass, and could act as a sensitive constraint on subgrid physics like star formation and feedback prescriptions (e.g., Cooper et al. 2015; Pillepich et al. 2015; Fattahi et al. 2020).

Intertwined questions about the ex situ component persist. Is it built from a handful of massive galaxies ($M_\star \sim 10^8\text{--}10^9 M_\odot$), or a multitude of metal-poor ultra-faints ($M_\star \lesssim 10^5 M_\odot$; e.g., Robertson et al. 2005; Frebel et al. 2010; Deason et al. 2015, 2016; D’Souza & Bell 2018)? How does the metallicity of the halo change as a function of radius? Does the halo transition into a metal-poor ($[\text{Fe}/\text{H}] \sim -2.2$), spherical structure beyond 20 kpc as predicted by local energetic orbits in the popular “dual halo” scenario (e.g., Carollo et al. 2007, 2010; Beers et al. 2012)? Are different accreted galaxies responsible for this shift? Or could this be due to a smooth component from dissolved ancient globular clusters (e.g., Martell et al. 2011; Carretta 2016; Koch et al. 2019)? Is the traditional conception of the distant halo as a metal-poor structure a selection artifact, arising from color cuts designed to avoid the disk, and from metallicity-biased standard candles (e.g., Conroy et al. 2019b)?

Studying the stellar halo also enables new forms of near-field cosmology. For instance, accreted debris from $M_\star = 10^6\text{--}10^7 M_\odot$ galaxies gives us access on a star-by-star level to high-redshift galaxies whose evolution was frozen at the time of infall. This provides a complementary view on issues of the distant universe—for instance, the evolution of the interstellar medium (ISM; e.g., Steidel et al. 2016; Bian et al. 2020), the interplay between reionization and low-mass galaxies (e.g., Barkana & Loeb 1999; Naidu et al. 2020), the shape of high- z star formation histories (e.g., Caplar & Tacchella 2019; Leja et al. 2019)—at a resolution and mass limit even beyond the reach of upcoming Extremely Large Telescopes and the James Webb Space Telescope (e.g., Weisz et al. 2014; Boylan-Kolchin et al. 2015, 2016).

Previous efforts to directly probe the distant halo have had to overcome the challenge of targeting rare, distant stars without the benefit of Gaia parallaxes to filter out nearby contaminants. One common solution has been to use color cuts that implicitly or explicitly select for low metallicities to avoid the disk (e.g., Chiba & Beers 2000; Carollo et al. 2007; Ivezić et al. 2008; Sesar et al. 2011; Xue et al. 2015; Zuo et al. 2017). Another common choice is to rely on rare, standardizable candles like RR Lyrae and blue horizontal branch stars (BHBs) that are inherently metal poor and more abundant in older populations (e.g., Deason et al. 2011; Kafle et al. 2012; Janesh et al. 2016; Cohen et al. 2017; Iorio & Belokurov 2019). Studies based on these tracers have collectively shown the distant Galaxy to display a high degree of substructure, which has been interpreted as support for an accretion origin of the halo (e.g., Bell et al. 2008; Starkenburg et al. 2009; Xue et al. 2011; Schlaufman et al. 2012; Deason et al. 2018). In order to make further progress and ask more detailed questions—which accreted structure dominates at what radius? how far does the in situ halo extend? what is the mass function of accreted material?—we require a homogeneously selected, metallicity-unbiased sample with full 6D phase-space coordinates, chemical information, and an easily interpretable selection function.

The H3 (“Hectochelle in the Halo at High Resolution”) Survey (Conroy et al. 2019a) is fulfilling this need. H3 is a spectroscopic survey of 200,000 stars in high-latitude fields designed to study the distant Galaxy. A defining feature of H3 is a simple, Gaia-based selection function (parallaxes implying $d_{\text{helio}} > 2$ kpc) that, critically, is unbiased in metallicity. With this survey, we aim to search for new structure in the distant halo, trace known structures out to their apocenters, clarify long-standing debates about the nature of the halo, and explore promising avenues for near-field cosmology.

In this work, we present a census of substructure, previously known and unknown, out to 50 kpc and link the results to the questions outlined in this section. In Section 2, we provide details of H3 pertinent to this study (Section 2.1), outline how we compute dynamical quantities (Section 2.2), and correct for the survey selection function (Section 2.3). In Section 3.1, we present an overview of our sample in integrals of motion and chemistry, revealing a high degree of substructure. Section 3.2 forms the bulk of the paper—here we identify and define individual structures, and remark on their chemodynamical properties. Section 3.3 provides a synopsis of all the structures identified. In Section 4, we discuss the implications of the inventory—we chart the relative fractions of structures with distance (Section 4.1), interpret what this means for the origin of the halo (Section 4.2), evaluate the net rotation of the halo (Section 4.3), dissect the halo in chemical space (Section 4.4), and discuss caveats (Section 4.5). A summary of our results is provided in Section 5.

To describe central values of distributions, we generally report the median along with the 16th and 84th percentiles. We use $\langle x \rangle$ to denote the mean of the quantity x and report the corresponding error on the mean as 16th and 84th percentiles estimated via bootstrapping. We use r_{gal} to denote 3D Galactocentric distance, R_{gal} to denote axial distance in Galactocentric cylindrical coordinates, Z_{gal} to denote distance from the plane, and d_{helio} to refer to 3D heliocentric distance. We use V_r , V_ϕ , V_θ to represent velocities in a right-handed spherical coordinate system with origin at the Galactic center.

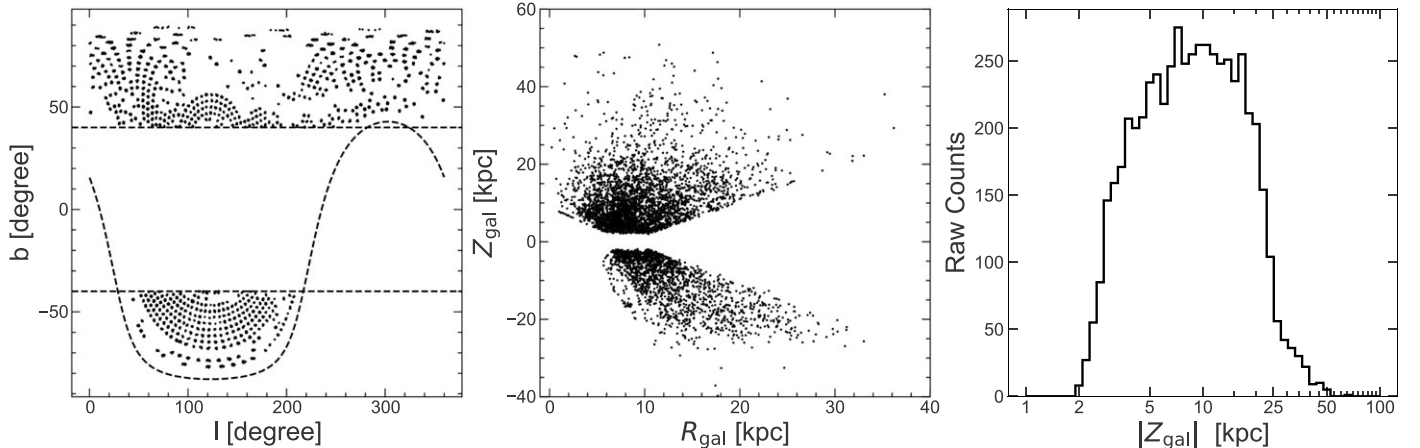


Figure 1. Overview of the H3 Survey. Left: current footprint in Galactic coordinates. Dashed lines demarcate $|b| = 40^\circ$ and decl. $= -20^\circ$. The survey will eventually cover $|b| > 30^\circ$. A majority of fields ($\approx 65\%$) are in the northern Galactic sky due to the location of the survey telescope ($+32^\circ$, AZ, USA). Center: spatial extent of the sample used in this work in cylindrical, Galactocentric coordinates. Right: distribution of distance from the plane. 99.9% of the sample lies at an elevation of > 2 kpc, with a median elevation of ≈ 9 kpc.

That is, prograde stars have negative V_ϕ and L_z . In the context of photometric magnitudes, “ r ” refers to the Pan-STARRS r band (Chambers et al. 2016; Flewelling et al. 2016) that is used in the H3 selection function. Magnitudes are in the AB system (Oke & Gunn 1983). When converting between redshifts and ages, we use a cosmology with $\Omega_M = 0.3$, $\Omega_\Lambda = 0.7$, $H_0 = 70 \text{ km s}^{-1} \text{ Mpc}^{-1}$, i.e., $h = 0.7$. Unless mentioned otherwise, total orbital energy (E_{tot}) is always reported in units of $10^5 \text{ km}^2 \text{ s}^{-2}$ and angular momenta (L_x, L_y, L_z) are reported in units of $10^3 \text{ kpc km s}^{-1}$.

2. Data and Methods

2.1. The H3 Survey

H3 (Conroy et al. 2019a) is the first spectroscopic survey to leverage Gaia parallaxes, π , in its selection of targets. The selection function of the primary sample is composed of the following conditions: (i) $15 < r < 18$, (ii) $\pi - 2\sigma_\pi < 0.5$, implying $d_{\text{helio}} > 2$ kpc, (iii) $|b| > 30^\circ$, to avoid the disk, and (iv) decl. $> -20^\circ$, observable from the MMT located in Arizona, USA (see Figure 1). This simple selection function ensures a view of the halo that is free from metallicity biases due to color cuts or metal-poor stellar tracers (e.g., BHBs, RR Lyrae). While H3 will eventually cover $|b| > 30^\circ$ and the survey selection function requires Gaia parallaxes consistent with $d_{\text{helio}} > 2$ kpc, the data presented in this paper are at $|b| > 40^\circ$ and also limited to $d_{\text{helio}} > 3$ kpc (for reasons outlined in Section 2.3).

Complementing the primary selection, we target a small number ($\approx 6\%$ of the final sample used in this work) of color-selected K giants ($\approx 5\%$, cuts from Conroy et al. 2018), BHBs ($\approx 1\%$, cuts from Deason et al. 2014), and RR Lyrae (seven in number, sourced from Sesar et al. 2017b). We take care to appropriately weight these specially targeted stars while accounting for the selection function in Section 2.3. Inspection of stellar parameters of the BHBs reveals that while their distances and radial velocities are robust, their abundances are not reliable, so they are omitted from plots featuring $[\text{Fe}/\text{H}]$ and $[\alpha/\text{Fe}]$.

The key outputs from the survey are radial velocities precise to $\lesssim 1 \text{ km s}^{-1}$, $[\text{Fe}/\text{H}]$ and $[\alpha/\text{Fe}]$ abundances precise to $\lesssim 0.1$ dex, and spectrophotometric distances precise to $\lesssim 10\%$

(see Cargile et al. 2020 for details on the stellar parameter pipeline). Combined with Gaia proper motions (signal-to-noise ratio, $S/N > 3$ for $> 90\%$ of the sample), H3 thus provides the full 6D phase space and 2D chemical space for the sample stars. The survey is ongoing: $\approx 125,000$ targets have been observed as of 2020 March and they form the basis of this work.

In this paper we focus on an $S/N > 3$ subsample whose stellar parameters are deemed robust (“flag = 0” in v2.4 of the survey catalogs but also allowing for BHBs and RR Lyrae). We work only with the primary parallax-selected and secondary color-selected K giant/BHB/RR Lyrae samples described earlier ($\text{xfit_rank} = 1$ or 2), leaving out the fainter and higher parallax filler targets. We restrict our sample to the 6799 giants ($\log g < 3.5$) to ensure a relatively uniform view of the halo. The dwarfs, while numerous, are complete only out to $d_{\text{helio}} \sim 10$ kpc and would require significant selection function corrections (see Section 2.3 for details) to be interpreted on the same footing as the giants used in this study. Visual inspection of the spectra and corner plots of the stellar parameters suggest metallicities below -3 are less reliable at $S/N \approx 3$ so we remove the 23 stars that would have otherwise made it into our sample. We further limit this sample per the considerations in Sections 2.2 and 2.3.

2.2. Computing Phase-space Quantities

We adopt the Galactocentric frame implemented in Astropy v4.0 (Astropy Collaboration et al. 2013, 2018), which has the following parameters: $R_0 = 8.122$ kpc (Gravity Collaboration et al. 2019), $[V_{\text{R},\odot}, V_{\phi,\odot}, V_{\text{Z},\odot}] = [-12.9, 245.6, 7.78] \text{ km s}^{-1}$ (Drimmel & Poggio 2018), and $Z_\odot = 20.8$ pc (Bennett & Bovy 2019). This frame is right handed, i.e., prograde (retrograde) orbits have $L_z < 0$ ($L_z > 0$).

Potential-related quantities (actions, eccentricities, energies) are computed using gala v1.1 (Price-Whelan 2017; Price-Whelan et al. 2017) with its default MilkyWayPotential. This potential, based on Bovy (2015), is composed of a Hernquist (1990) nucleus ($m = 1.7 \times 10^9 M_\odot$, $a = 1$ kpc) and bulge ($m = 5 \times 10^9 M_\odot$, $a = 1$ kpc), a Miyamoto & Nagai (1975) disk ($m = 6.8 \times 10^{10} M_\odot$, $a = 3$ kpc, $b = 0.28$ kpc), and a spherical Navarro et al. (1997) dark matter halo ($m = 5.4 \times 10^{11} M_\odot$, $a = 15.62$ kpc), where m , a , and b are

the characteristic mass and scale radii of these models, respectively. The mass enclosed within 200 kpc is $9.9 \times 10^{11} M_{\odot}$ consistent with recent estimates (e.g., Zaritsky et al. 2020 and references therein). We also show the final summary plots in the McMillan (2017) potential in Appendix B, both to ease comparison with studies that use this potential (e.g., Koppelman et al. 2019a; Myeong et al. 2019) and to demonstrate that the features described in this paper are not specific to our choice of the Galactic potential.

Orbits are computed using the Dormand & Prince (1978) explicit integration scheme, which belongs to the Range–Kutta family of ordinary differential equation solvers, with time steps of 1 Myr and a total integration time of 25 Gyr. Eccentricities are computed from these orbits as $e = \frac{r_{\text{apo}} - r_{\text{peri}}}{r_{\text{apo}} + r_{\text{peri}}}$, where r_{apo} and r_{peri} are the orbital apocenter and pericenter, respectively. Actions ($J_R, J_{\phi}, J_z, J_{\text{tot}} = \sqrt{J_{\phi}^2 + J_z^2 + J_R^2}$) are estimated from the computed orbits as per the torus-mapping method described in Sanders & Binney (2016). We test the robustness of the computed actions by checking that (a) J_{ϕ} converges to J_z within 5%, as expected in an axisymmetric potential like the one adopted here, and (b) actions calculated using 75% of the orbit and 100% of the orbit differ by no more than 1%. In the few cases ($\approx 5\%$) where these conditions are not met (typically long-period orbits for stars at > 20 kpc), we recompute the actions by extending the 25 Gyr integration period by $2 \times$, up to 200 Gyr (this is a choice made purely for numerical stability to collect a statistical number of orbital periods for long-period orbits). After this, only a small number of bound stars (≈ 50), mostly with $J_z \approx 0$, fail our tests (as expected for very eccentric orbits with $J_R \sim J_{\text{tot}}$; Figure 3 of Sanders & Binney 2016). and we exclude them from any analysis involving actions.

The error budget on phase-space quantities is dominated by uncertainties in spectrophotometric distances and Gaia proper motions (PMs). For an illustration of how measurement errors distort substructure in $E - L_z$ we point readers to Appendix A. Because $E - L_z$ is a key diagram in the analysis to follow, we limit the sample to stars that satisfy (i) $(|E_{\text{tot}}|/\sigma_{E_{\text{tot}}} > 3) \wedge (|L_z|/\sigma_{L_z} > 3)$, or (ii) $(\sigma_{E_{\text{tot}}} < 0.1 \times 10^5 \text{ km}^2) \wedge (\sigma_{L_z} < 0.5 \times 10^3 \text{ kpc km s}^{-1})$, where “ \wedge ” stands for the Boolean “and” operator. Condition (i) is a relative error cut, and condition (ii) ensures we do not discriminate against low $|L_z|$ stars that comprise a large fraction of the halo. A total of 1024 stars, a majority of which have uncertain Gaia PMs ($S/N < 3$), are excised due to these cuts. The excised stars lie at larger distances, including some of our most distant giants, and ≈ 300 of them judging by their PMs are likely members of the Sagittarius stream. The excised stars have a metallicity distribution function (MDF) similar to the sample used in this work, except they have fewer metal-rich disk stars (because the excised stars lie at larger distances). We expect improvement in the PM S/N for these stars from future data releases of the Gaia mission. This leaves us with a current sample of 5752 giants.

2.3. Correcting for the H3 Selection Function

Every spectroscopic survey has a selection function that can be thought of as the conditional probability $p(\text{obs.} | \theta)$ that a star with parameters θ (l, b, d_{helio} , age, $[\text{Fe}/\text{H}]$, $[\alpha/\text{Fe}]$...) will be observed by the survey (for a comprehensive overview, see Everall & Das 2020). In general, the survey selection function represents a biased view of the underlying population. For instance, in a purely magnitude-limited survey, $p(\text{obs.})$ is

higher for nearby stars, so if one compares the fractions of two accreted structures with different mean heliocentric distances, raw star counts would provide a biased picture. In order to obtain an unbiased view, one must correct for the selection function by using weights that are proportional to $p(\text{obs.} | \theta)^{-1}$. In what follows, we outline how these weights are computed for our sample.

The H3 selection function can be decomposed into three independent components: (i) where we point the telescope ($|b| > 30^\circ$, $\text{decl.} > -20^\circ$), i.e., the “window selection,” (ii) the sample definition ($15 < r < 18$, $\pi - 2\sigma_{\pi} < 0.5$), i.e., the “magnitude selection” and (iii) the fraction of stars from the input sample that end up with spectra, which leads to a “targeting selection.”

Window selection: H3 is limited to $|b| > 30^\circ$ by design and to $\text{decl.} > -20^\circ$ by geography. Any structures that are anisotropically distributed on the sky will require some correction for the survey window function. However, correction for the window is difficult as it requires a model for the underlying anisotropy. In this work, we limit ourselves to demonstrating the existence of various substructures and commenting on their relative contribution to the high-latitude Galaxy sampled within our survey fields.

Magnitude selection: the H3 selection function imposes a magnitude cut ($15 < r < 18$), which introduces a bias against distant and intrinsically less-luminous sources. We also limit the sample in this work to $S/N > 3$, which further discriminates against fainter sources. Further, by restricting the sample only to giants ($\log g < 3.5$), we are excluding bright, nearby dwarfs that satisfy the magnitude and parallax selections. These effects are illustrated in the top panel of Figure 2 for an example MIST v2.0 isochrone (10 Gyr, $[\text{Fe}/\text{H}] = -1$, $[\alpha/\text{Fe}] = 0$; Choi et al. 2016; A. L. Dotter et al. 2020, in preparation).

To correct for this, we sample from an isochrone matched to each star’s derived parameters (age, $[\text{Fe}/\text{H}]$, $[\alpha/\text{Fe}]$, A_V) using a Kroupa (2001) IMF and calculate $f_{\text{mag}}(d_{\text{helio}})$, the fraction of $\log g < 3.5$ stars at the star’s distance that fall at $15 < r < 18$. We shrink the magnitude range according to the $S/N > 3$ cutoff for each field, which varies with observing conditions. For the subsample of color-selected rare stars (K giants and BHs, $\approx 6\%$ of the sample), instead of calculating $f_{\text{mag}}(d_{\text{helio}})$ using $15 < r < 18$, we use the appropriate color cuts and magnitude limits.

The correction weights ($1/f_{\text{mag}}$) for the example isochrone are plotted as a function of d_{helio} in the bottom panel of Figure 2. The curve has a “U” shape with a steep rise below 4 kpc and above 35 kpc. The number density of stars predicted by the IMF is high close to the main-sequence turnoff and falls off precipitously as one goes up the red giant branch. At $d_{\text{helio}} = 4\text{--}35$ kpc, the sections of the red giant branch with the highest number density as well as the red clump are almost entirely contained within $15 < r < 18$, and so at these distances the correction factor is fairly flat. Importantly, this distance range is where the bulk of our sample ($> 90\%$) lies. This means the H3 giants (even without any applied corrections) provide a relatively unbiased view of the halo at these distances.

Targeting selection: of all the stars that satisfy our selection function, we assign fibers to ≈ 200 per field. In fields closer to the dense galactic plane, the fraction of stars that are assigned a fiber is lower compared to higher latitudes—that is, at low $|b|$

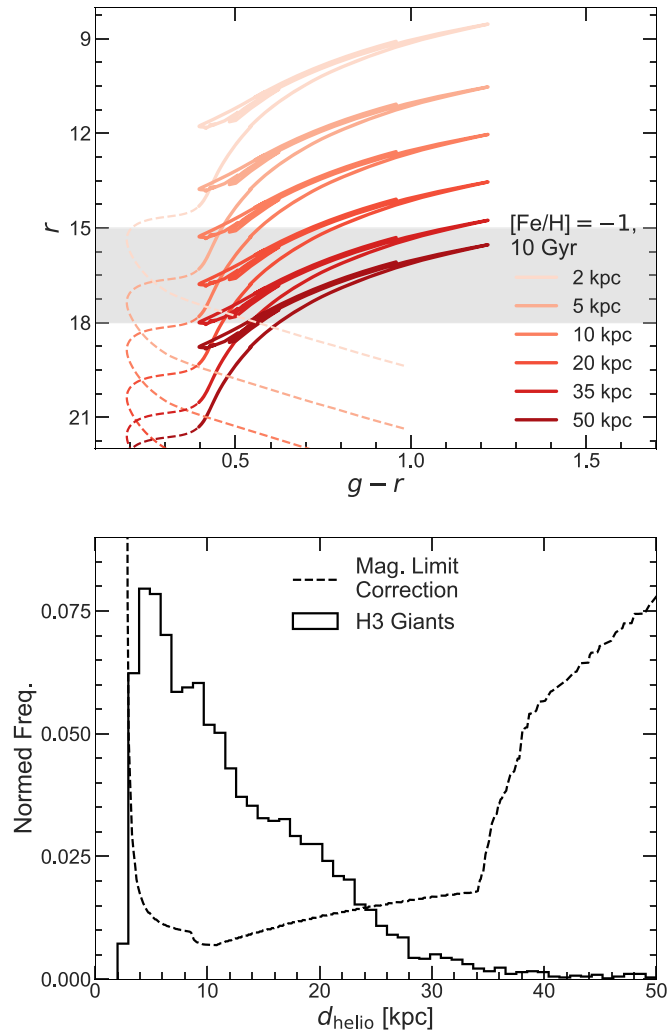


Figure 2. Correcting for the magnitude selection in the H3 selection function. Top: an $[\text{Fe}/\text{H}] = -1$, 10 Gyr isochrone at different distances, with giants ($\log g < 3.5$) highlighted with solid lines. At $d_{\text{helio}} \sim 4\text{--}35$ kpc, the silver band representing the survey magnitude limit ($15 < r < 18$) almost completely contains the sections of the red giant branch that have a high number density. Therefore, the stars at these distances require little correction for the magnitude limit. Bottom: correction weights as a function of heliocentric distance (dashed line) overplotted on the distance distribution for stars in this work. The weights are derived using isochrones and assuming a Kroupa (2001) IMF (see Section 2.3) and are remarkably flat for the bulk of the sample. The rise at 35 kpc coincides with the red clump moving out of our magnitude range.

the stars in our sample represent a larger underlying population. Another targeting bias arises from the higher fiber assignment rank we award to the small number (<1 per field on average) of rare, color-selected BHBs and K giants that we complement our main parallax-selected sample with. The higher rank means that fibers are assigned to all possible BHBs and K giants in a field before the other sources. As a result, the median fiber assignment probability for these stars is slightly higher than the main parallax-selected sample ($\approx 85\%$ versus $\approx 65\%$). Correcting for both these effects is straightforward. For a given field we compute f_{target} (rank), the fraction of stars of a given rank that ended up with $\text{S/N} > 3$ spectra out of all the stars of that rank that satisfied our selection function. For stars of the same rank, f_{target} is completely independent of stellar properties and hence can be simply multiplied with f_{mag} to produce the total weight.

We note that our approach here is conceptually similar to previous work (e.g., Bovy et al. 2014; Das et al. 2016; Stonkutė et al. 2016; Vickers & Smith 2018; Everall & Das 2020). We excise all 68 stars at $d_{\text{helio}} < 3$ kpc from our sample due to their very high weights (see Figure 2), and because we are interested in the distant Galaxy, leaving us with a final sample of 5684 stars. In the summary plots where we interpret the relative fractions of various substructures (Figures 19–21) and in Table 1, we employ weights equal to $(f_{\text{mag}} f_{\text{target}})^{-1}$. In all other figures, we display raw counts. The distinction between raw and weighted quantities is made explicit throughout the text.

3. Results

3.1. Overview of the High-latitude Galaxy

We begin with a general overview of the data in chemistry and integrals of motion (E – L_z , actions, eccentricity) to motivate the selection criteria for various structures in the sections to come. Figure 3 introduces the projections of the phase space and chemistry we will use frequently. Figure 4 provides an E – L_z “map” that identifies structure that will be presented in subsequent sections. We do this so readers can see the entire landscape at once, which will be helpful as we discuss individual structures in depth. Figures 5–7 present a high-level overview of features in E – L_z , actions, and chemistry.

In Figure 3, the top left panel shows E – L_z , which we use as our primary workspace. It has long been recognized that groups of stars accreted together display coherence in their energies and in the z component of their angular momentum, even when they are thoroughly dispersed in configuration space (e.g., Helmi & de Zeeuw 2000; Brown et al. 2005; Gómez et al. 2010, 2013; Simpson et al. 2019). In the second panel, we display V_r versus V_ϕ —in this space, stars on disk-like orbits intuitively occupy the region around the assumed rotation velocity of the Sun. This is also the space in which GSE was discovered by Belokurov et al. (2018) as an overdensity of stars around $V_\phi = 0$ that is also prominent in our data. In the third panel, we depict a summary of actions in the form of $(J_z - J_R)/J_{\text{tot}}$ versus J_ϕ/J_{tot} following Binney & Tremaine (2008) and Vasiliev (2019). Generally, stars on very radial or eccentric orbits are confined to the bottom half of this diagram while stars on polar or circular ($J_R = 0$) orbits occupy the top half of this diagram. Circular, in-plane disk orbits have $J_z = J_R = 0$, and $J_\phi/J_{\text{tot}} = -1$. Purely planar ($J_z = 0$) orbits, which would also occupy the bottom half of this diagram, are underrepresented in our $|Z_{\text{gal}}| > 2$ kpc sample. A similar diagram was used by Myeong et al. (2019) to discover the retrograde, accreted Sequoia structure and is a useful way to isolate GSE because it is largely confined to $J_z < J_R$ orbits. Eccentricities (bottom-left panel of Figure 3) are similarly useful in that GSE is almost completely confined to $e > 0.7$. Plotting eccentricity versus r_{gal} also shows abrupt changes in the density of stars around the pericenter/apocenter of various structures.

While actions are useful, we favor E – L_z while defining selections in part because this space is simpler to understand. Further, a large body of local halo studies has primarily deployed energy, eccentricities, and angular momenta, and we seek to draw direct connections and build on it (e.g., Helmi et al. 2017; Belokurov et al. 2018; Koppelman et al. 2019a). A high degree of overlap of multiple accreted structures is

Table 1
Summary of Substructure in the $|b| > 40^\circ$, $|Z_{\text{gal}}| > 2$ kpc Milky Way

Substructure	N_{raw}	frac.	[Fe/H]	[α /Fe]	ecc.	r_{gal} (kpc)	$ Z_{\text{gal}} $ (kpc)	$(J_z - J_R)/J_{\text{tot}}$	E_{tot} ($10^5 \text{ km}^2 \text{ s}^{-2}$)	L_z ($10^3 \text{ kpc km s}^{-1}$)
Gaia–Sausage–Enceladus	2684	0.42	−1.15	0.21	0.84	17.72	12.88	−0.50	−1.04	−0.01
Sagittarius	675	0.24	−0.96	0.12	0.54	32.31	24.13	0.51	−0.67	−1.51
High- α Disk + In Situ Halo	950	0.15	−0.54	0.34	0.48	9.00	3.53	−0.03	−1.34	−0.94
Arjuna	139	0.02	−1.20	0.24	0.55	22.91	16.66	0.16	−0.91	1.73
Metal-weak Thick Disk	144	0.02	−1.12	0.32	0.47	8.60	4.25	0.04	−1.38	−0.9
Aleph	122	0.02	−0.51	0.19	0.13	11.06	3.51	0.07	−1.13	−2.36
Wukong	111	0.01	−1.58	0.24	0.56	12.75	9.55	0.42	−1.18	−0.59
Helmi Streams	91	0.01	−1.28	0.15	0.46	17.17	13.55	0.47	−1.03	−1.14
Sequoia	72	0.01	−1.59	0.14	0.56	15.55	11.02	0.16	−1.02	1.31
I’itoi	65	0.01	−2.39	0.38	0.47	12.37	7.46	0.09	−1.04	1.35
Thamnos	32	0.01	−1.90	0.29	0.46	8.68	5.11	0.41	−1.35	0.46
Unclassified Debris (disk like)	208	0.02	−1.16	0.22	0.53	8.63	4.72	0.13	−1.36	−0.52
Unclassified Debris (halo like)	463	0.06	−1.20	0.19	0.60	18.25	14.19	0.40	−1.04	−0.03

Note. All quantities—with the exception of N_{raw} —are corrected for the selection function (see Section 2.3). The reported values are medians of their respective distributions. The listed substructures were defined via selections in phase space and chemistry, and so the reported values for those quantities used in the selection must be interpreted with care. For example, the [Fe/H] and [α /Fe] reported for Arjuna, Sequoia, Wukong, and Thamnos are the peaks of their distributions and not the medians, because these structures are selected using their MDFs in a way that biases the median.

expected in $E - L_z$ and other projections of phase space (e.g., Font et al. 2006; Jean-Baptiste et al. 2017; Pfeffer et al. 2020), which we resolve when possible using chemistry (bottom-center and bottom-right panels of Figure 3). Stars belonging to the same structure are expected to show coherent MDFs and distinct chemical evolutionary tracks in the [Fe/H] versus [α /Fe] plane that are a function of their mass, star formation history, and formation redshift (discussed further in Section 4.4).

In Figure 5, we show $E - L_z$ in bins of metallicity and color-coded by [α /Fe]. The most metal-rich stars define two sequences: one at higher energy, lower [α /Fe] (Aleph), and the other at lower energy, higher [α /Fe] (the high- α disk) that extends to $L_z \sim 0$ orbits (the in situ halo). At $-0.75 < [\text{Fe}/\text{H}] < -0.5$, two structures appear, one centered at $L_z \sim 0$ (GSE) and the other at high energy, $L_z \sim -2$, $E_{\text{tot}} \sim -0.75$ (Sgr). The density of the $L_z \sim 0$ population (GSE) peaks in the $-1.25 < [\text{Fe}/\text{H}] < -1$ panel. High-energy retrograde stars only begin to appear at $[\text{Fe}/\text{H}] < -0.75$ and are almost entirely absent from the higher metallicity bins. Several smaller clumps appear in various [Fe/H] intervals. From this figure, it is already clear that a very small fraction of the halo within 50 kpc is metal poor ($[\text{Fe}/\text{H}] \leq -1.75$).

Figure 6 is similar to Figure 5, but here we separate the stars by actions. Stars with $J_z > J_R$, on polar or circular orbits, are limited to the top row and stars with $J_z < J_R$, on radial or eccentric orbits, are limited to the bottom row. The most prograde structure ($L_z < -2$) is α -poor and confined to the first two panels (Aleph). The high-energy population at $L_z \sim -2$, $E_{\text{tot}} \sim -0.75$ is also confined to the top row (Sgr). A prominent structure centered at $L_z \sim 0$ appears largely at $J_z < J_R$ and dominates the bottom row (GSE). The other disk-like prograde population that extends to $L_z \sim 0$ is spread across the top and bottom rows (high- α disk and in situ halo), as are the high-energy retrograde halo stars.

Figure 7 depicts [α /Fe] versus [Fe/H], binned by actions and angular momenta and color-coded by eccentricity. This figure is particularly rich in structure and underscores the power of combining chemistry with dynamics. We highlight a few prominent populations apparent in this figure. There is a

highly circular (shaded black), metal-rich ($[\text{Fe}/\text{H}] < -0.5$), $J_z > J_R$ population completely contained within the top-left panel (Aleph). Adjacent to it, at lower [Fe/H] and [α /Fe], appears an agglomeration of more eccentric stars that is also confined purely to the top-left panel (Sgr). The most α -rich population is dispersed across the first two columns and has orbits ranging from highly eccentric to circular and extends from prograde to radial L_z (high- α disk + in situ halo). Among the $J_z < J_R$ orbits, we see a well-populated sequence largely contained within the bottom-center panel (GSE).

Through these figures, we have demonstrated the distant halo to be highly structured in chemodynamical space, with various populations appearing preferentially in certain regions of metallicity and orbital space. We now proceed to define and characterize these individual structures in detail.

3.2. Substructure Inventory

In what follows, we provide a detailed inventory of the $|b| > 40^\circ$, $d_{\text{helio}} > 3$ kpc MW, one component at a time. We provide relevant background on each component, justify our selection, and comment on any noteworthy features. We support this discussion with a corresponding six-panel figure for each component that situates it in chemodynamical space. Each six-panel figure follows the layout introduced in Figure 3, with the top-right panel changing across figures to highlight a particular projection of chemodynamical space most relevant for the structure under discussion. We emphasize that the primary goal of this work is a high-level inventory. This means we focus on cleanly selecting various components rather than on a thorough characterization and analysis of their nature, which we defer to forthcoming work.

We first outline our overall strategy. We begin by selecting the most coherent, well-defined structures in chemodynamical space—Sagittarius, Aleph, the high- α disk, and the in situ halo. Having accounted for the eccentric stars of the in situ halo and Sgr, we assign the remaining highly eccentric ($e > 0.7$) stars to GSE. Next, we isolate other known halo structures in the literature (the Helmi Streams, Thamnos, Sequoia). While investigating Sequoia in the high-energy retrograde halo, we identify a relatively metal-poor (I’itoi) and metal-rich

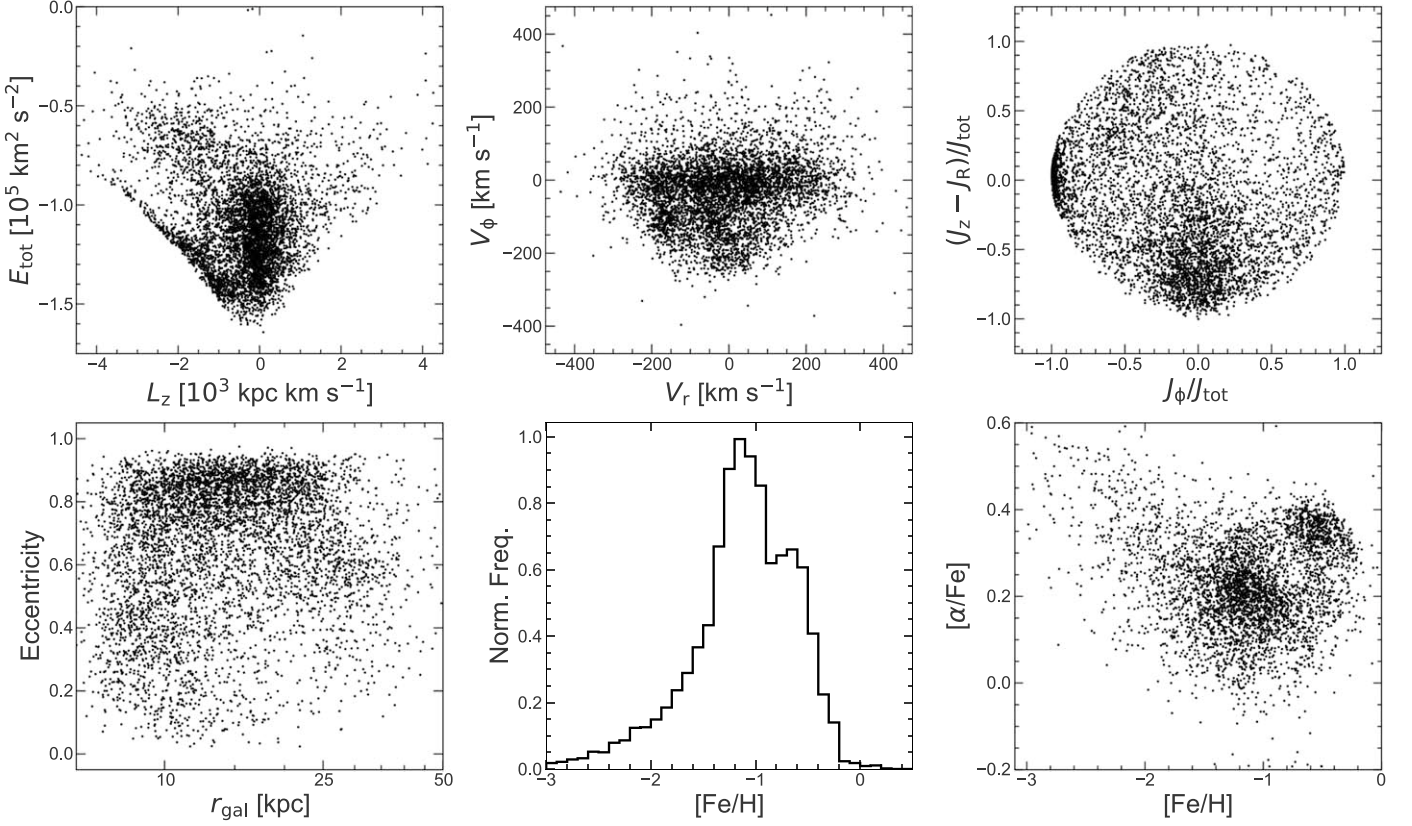


Figure 3. Overview of sample in phase space and chemistry. Top left: total energy (E_{tot}) vs. the z component of the angular momentum (L_z). Stars belonging to the same physical structure are expected to cluster in integrals of motion such as energy and angular momentum (L_z , in particular, in an axisymmetric potential). Top center: azimuthal velocity (V_ϕ) vs. radial velocity (V_r). Disk-like populations appear at negative V_ϕ around our assumed $V_{\phi,\odot} = -245.6 \text{ km s}^{-1}$. Top right: summary of actions. Structures with strong vertical action (J_z) occupy the top half of the diagram while those with a strong radial action (J_R) occupy the bottom half. Prograde stars fall in the left hemisphere and retrograde stars in the right. Bottom left: eccentricity vs. Galactocentric distance. In this space, stars from the same accreted object have similar eccentricities because they are on similar orbits and show density breaks around their apocenters. Bottom center: metallicity distribution function (MDF). The bins are 0.1 dex in size, corresponding to the typical uncertainty in $[\text{Fe}/\text{H}]$ (< 0.1 dex). Bottom right: α -abundance ($[\alpha/\text{Fe}]$) vs. iron abundance ($[\text{Fe}/\text{H}]$). We only show $S/N > 5$ stars in this and all such subsequent panels to improve clarity. Distinct stellar populations are expected to follow chemical evolutionary tracks corresponding to their star formation history and mass.

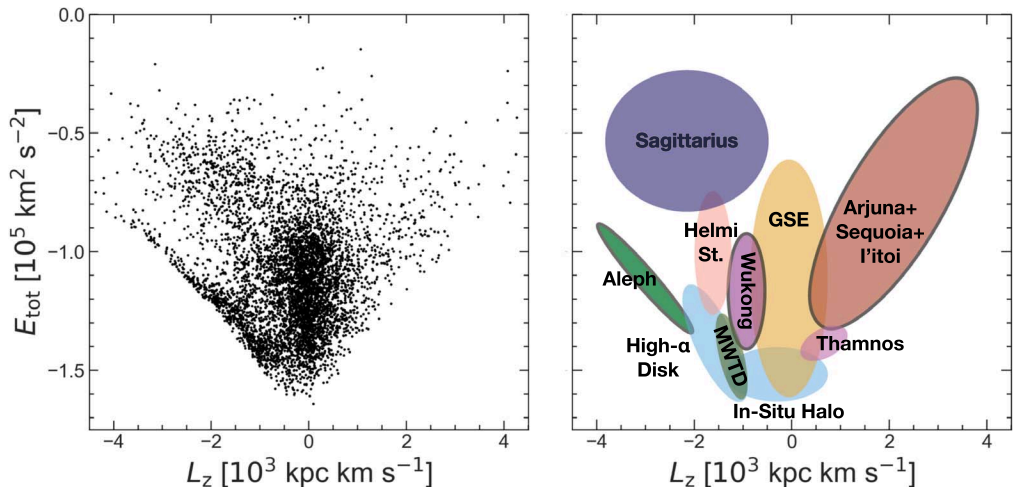


Figure 4. An overview of structure in $E-L_z$. Left panel same as Figure 3. In the right panel, we provide a schematic of the various structures we will identify in this work (structures highlighted with solid boundaries, except for Sequoia, are new)—Sagittarius (“Sgr,” Section 3.2.1, Figure 8), Aleph (Section 3.2.2, Figure 9), the high- α disk and in situ halo (Section 3.2.3, Figure 10), Gaia-Sausage-Enceladus (“GSE,” Section 3.2.4, Figure 11), the Helmi Streams (“Helmi St.,” Section 3.2.5, Figure 12), Thamnos (Section 3.2.6, Figure 13), Arjuna, Sequoia, and I’itoi (Section 3.2.7, Figure 14), Wukong (Section 3.2.8, Figure 15), and the metal-weak thick disk (MWTD; Section 3.2.9, Figure 16). There is significant overlap among these structures in chemodynamical space, so in defining and discussing them sequentially, it is impossible to avoid referring to objects that are yet to be introduced. We provide this schematic to build a common frame of reference and so readers may notice these structures in figures to come.

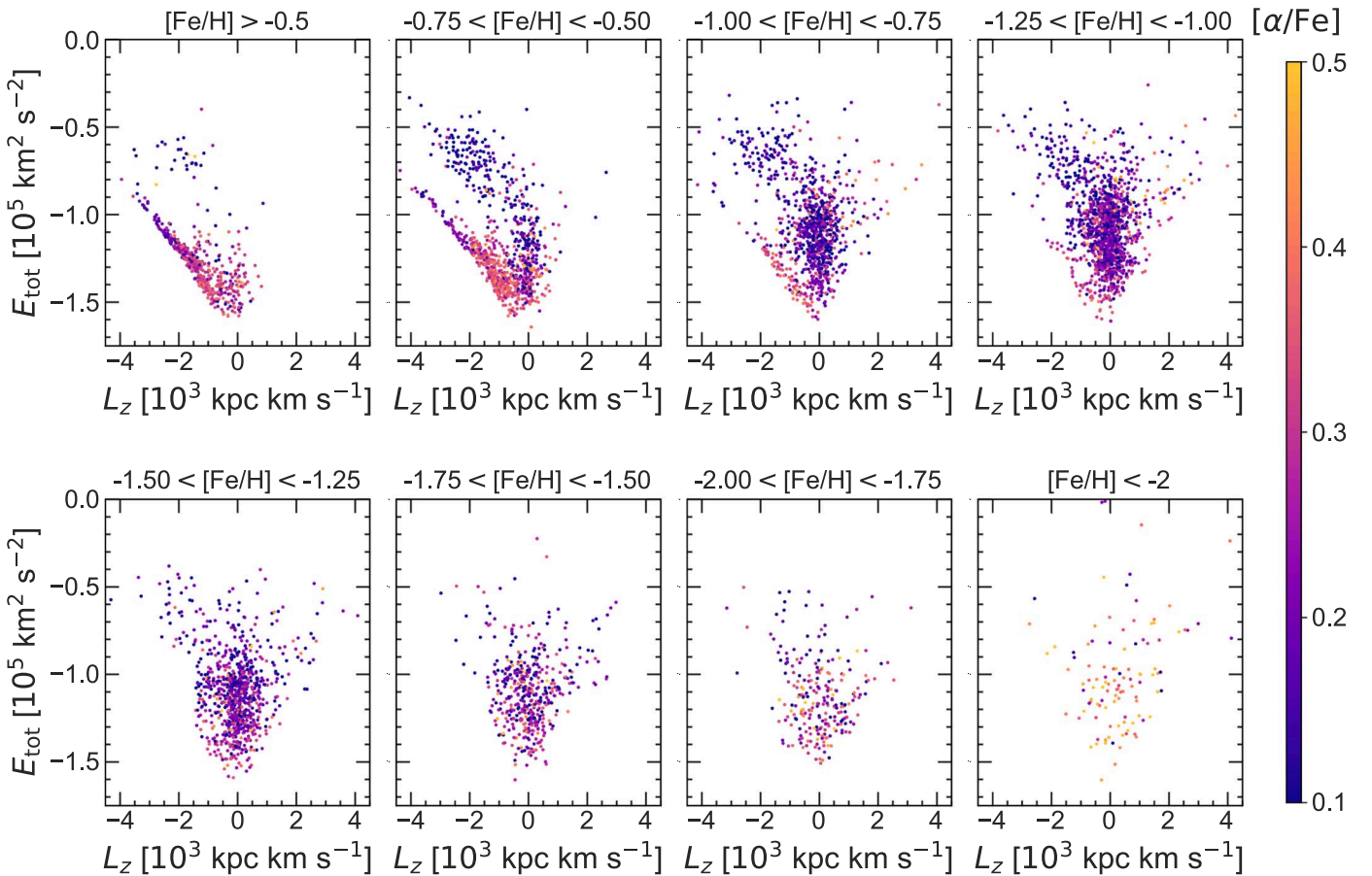


Figure 5. $E-L_z$ binned by $[\text{Fe}/\text{H}]$, color-coded by $[\alpha/\text{Fe}]$, ordered by decreasing $[\text{Fe}/\text{H}]$. The most metal-rich bin is largely composed of stars on disk-like orbits with negative L_z that extend smoothly to eccentric, $L_z \sim 0$ orbits. The most prograde stars ($L_z \lesssim -2$) define an α -poor sequence confined to the first two panels. Two populations, one centered at $L_z \sim 0$ and another at $E_{\text{tot}} \sim -0.75$, emerge in the second panel and comprise the bulk of the stars in the remaining panels. High-energy retrograde stars appear at $[\text{Fe}/\text{H}] < -0.75$. The very metal-poor bins at $[\text{Fe}/\text{H}] < -1.75$ are sparsely populated but still clumpy. The most metal-poor bins are not biased to particularly high energies (i.e., larger distances).

population (Arjuna) in the same $E-L_z$ region. After subtracting out all these structures, we turn to a remaining prograde $E-L_z$ overdensity (Wukong). We also highlight a metal-poor, α -rich, rotationally supported population that we identify as the metal-weak thick disk (MWTD). The remaining stars are labeled unclassified debris.

While selecting a structure, we exclude all the previously defined structures. This choice ensures that new structures (Arjuna, Itoi, Wukong) that appear toward the end of our inventory have reduced overlap with previously identified ones. We often rely on chemistry in our selections due to the high degree of overlap expected for accreted structures in integrals of motion (e.g., Font et al. 2006; Jean-Baptiste et al. 2017; Pfeffer et al. 2020). For instance, the low-eccentricity tail of GSE ($e < 0.7$) is a major contaminant in purely phase-space selections of lower-mass objects, but we are able to exclude it by appealing to chemistry. As much as possible, we incorporate insights from the existing literature in our selections—for instance, for the Helmi Streams and Thamnos, we use literature definitions as our starting point, and for Sequoia we are guided by previous studies of its chemistry.

Instead of using clustering algorithms (e.g., Fraix-Burnet & Davoust 2015; Yuan et al. 2018, 2020b; Koppelman et al. 2019a; Mackereth et al. 2019; Necib et al. 2020; Ostdiek et al. 2020), we take an artisanal approach, making simple, physically motivated, easily reproducible selections. Through

extensive experimentation, we have found that clustering algorithms (e.g., DBSCAN, HDBSCAN, k-means) either fracture the space into too many clusters or assign the entire sample to Sagittarius, GSE, the high- α disk, and Aleph (i.e., the structures apparent by eye in Figures 5, 6, 7). In the case of a high degree of fracturing, we then had to consider one at a time the nature of each mini cluster, akin to Yuan et al. (2020b), whose algorithm applied to $[\text{Fe}/\text{H}] < -1.8$ stars in LAMOST yielded 57 distinct groups, almost all of which they coalesced back into GSE and Sequoia. A downside of our approach compared to clustering methods is the deterministic assignment of every star as belonging to one structure or another instead of assigning membership probabilities and marginalizing over them (also discussed in Section 4.5).

3.2.1. Sagittarius

The stream of debris associated with the Sagittarius (Sgr) dwarf spheroidal galaxy (Ibata et al. 1994) provides the clearest demonstration of the hierarchical build-up of the stellar halo. In recent years, Sgr debris has been traced out to ~ 100 kpc, showing surprising features (e.g., Belokurov et al. 2014; Hernitschek et al. 2017; Sesar et al. 2017a; Li et al. 2019) and inspiring a new generation of numerical models (e.g., Dierickx & Loeb 2017; Laporte et al. 2018; Fardal et al. 2019) that builds on earlier work (e.g., Johnston et al. 1995; Law et al. 2005;

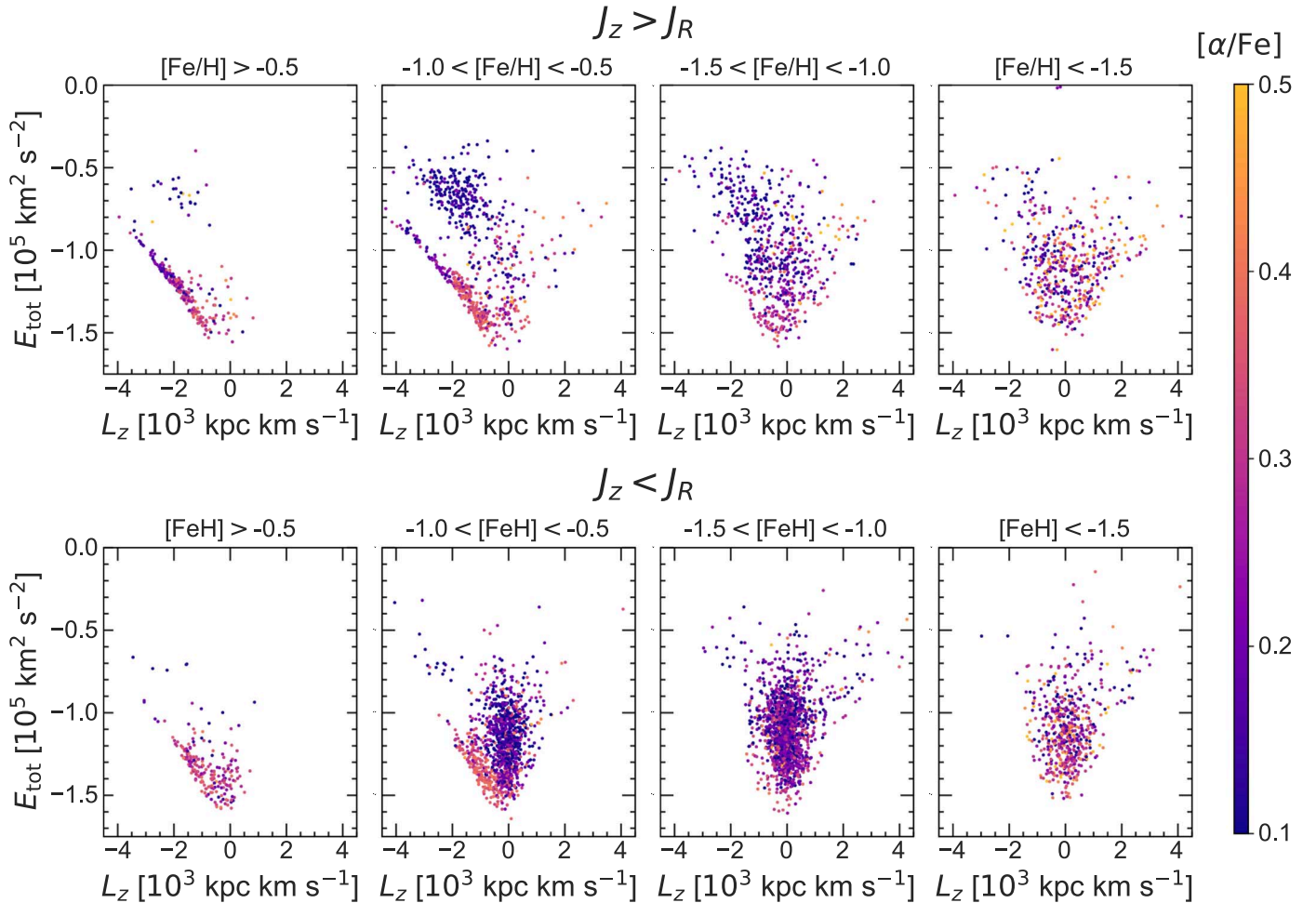


Figure 6. $E - L_z$ binned by $[\text{Fe}/\text{H}]$ and actions, color-coded by $[\alpha/\text{Fe}]$. Top: stars with $J_z > J_R$, which rise to high elevations off the plane. Some populations (the highly prograde α -poor sequence, the stars at $E_{\text{tot}} \sim -0.75$) are completely confined to $J_z > J_R$ orbits, while others (e.g., the high-energy retrograde stars) show no such preference and are equally distributed between $J_z > J_R$ and $J_z < J_R$. Bottom: stars with $J_z < J_R$ that are on radial or eccentric orbits. The most metal-rich bins show α -rich, disk-like stars that extend to eccentric orbits at $L_z \approx 0$. At lower metallicity, a dense cloud of α -poor stars appears at $L_z \sim 0$, with retrograde structure appearing at $[\text{Fe}/\text{H}] < -1$.

Law & Majewski 2010). In tandem, its chemistry is beginning to be resolved in ever greater detail by large spectroscopic efforts (e.g., Alfaro-Cuello et al. 2019; Li et al. 2019; Hayes et al. 2020) that are building on earlier efforts (e.g., Bellazzini et al. 2006; Chou et al. 2007; Monaco et al. 2007; Carlin et al. 2012; Gibbons et al. 2017).

Before Gaia, studies made the best of incomplete phase-space data to select Sgr stream stars, typically relying on heuristics such as distance from the orbital plane (e.g., Newberg et al. 2003; Belokurov et al. 2014; Lancaster et al. 2019). However, with full phase-space information, clean selections that fully exploit the highly coherent Sgr features are now possible (e.g., Li et al. 2019; Yang et al. 2019; Hayes et al. 2020). Sgr is a high-energy, prograde overdensity in $E - L_z$, and owing to its polar orbit, its angular momentum is concentrated in L_y . Capitalizing on this, we define Sgr stars as those which satisfy

$$L_y < -0.3L_z - 2.5 \times 10^3 \text{ kpc km s}^{-1}. \quad (1)$$

We verify that this simple criterion selects $>99.5\%$ of the star particles in a version of the Law & Majewski (2010) model that is matched to the current H3 footprint with a 10% distance uncertainty (see Johnson et al. 2020 for more detailed

comparisons with models). The selected 612 stars are shown in Figure 8—Sgr comprises the majority of our distant stars. Additionally, we identified 63 stars that do not satisfy Equation (1) but have PMs highly aligned with stars selected by Equation (1). Closer inspection revealed that the distances to these stars are incorrect, due to confusion between the red clump and red giant branch (Mackereth et al. 2017; Masseron & Hawkins 2017). When the distances to these stars are doubled, they satisfy Equation (1). In our pipeline, this confusion arises for low- $[\alpha/\text{Fe}]$ stars (<0.1) where Sgr is the dominant structure. These stars have a similar magnitude distribution to those selected by Equation (1), so when computing relative fractions (e.g., in Table 1 and Figure 18), we adjust our Sgr numbers upwards by 10% (i.e., 63/612) but do not show these stars in projections of phase space.

A detailed characterization of Sgr in H3 is forthcoming (Johnson et al. 2020). Here we only remark on prominent features in the MDF, which displays two peaks in $[\text{Fe}/\text{H}]$ separated by ≈ 0.4 dex. This is consistent with the picture in Hayes et al. (2020, their Figure 7), who find different mean metallicities in the leading and trailing arms and a similarly multipeaked MDF. There may also be a link to the complex

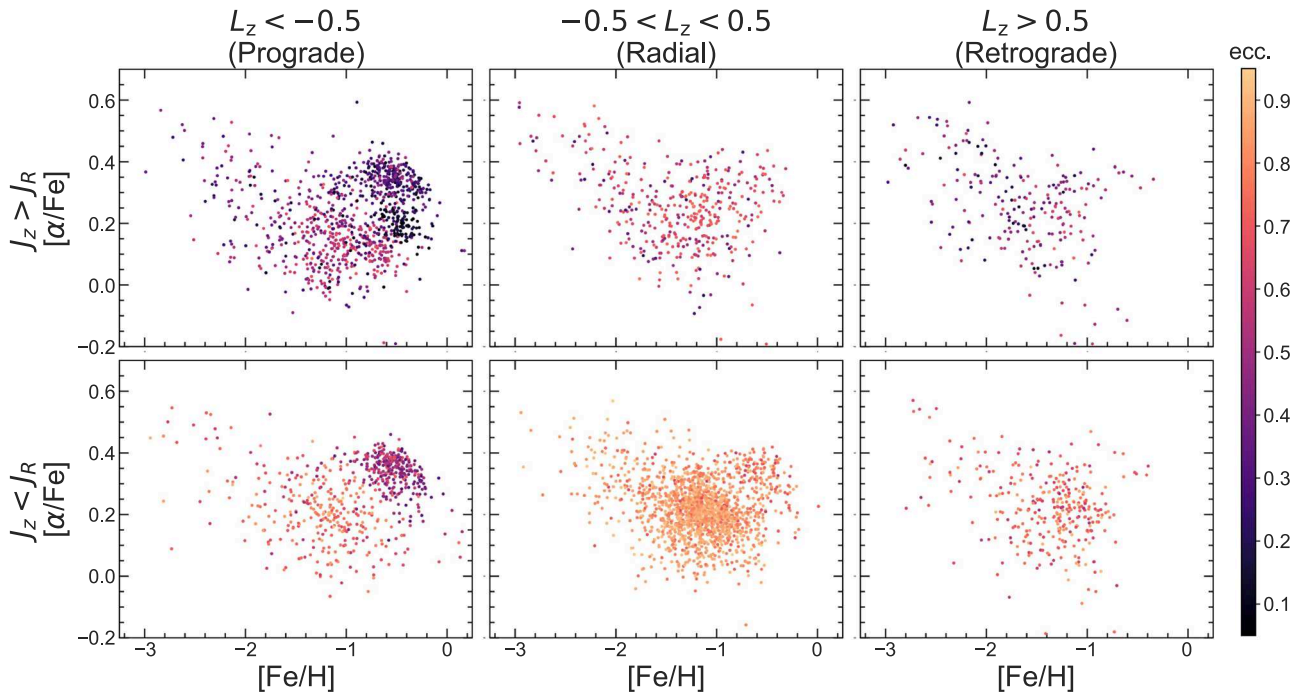


Figure 7. $[\alpha/\text{Fe}]$ vs. $[\text{Fe}/\text{H}]$ color-coded by eccentricity and binned by orbit type— $L_z/[10^3 \text{ kpc km s}^{-1}] < -0.5$ (prograde, left), $-0.5 < L_z/[10^3 \text{ kpc km s}^{-1}] < 0.5$ (radial, center), $L_z/[10^3 \text{ kpc km s}^{-1}] > 0.5$ (retrograde, right), $J_z > J_R$ (top), $J_z < J_R$ (bottom). The morphology of chemical space varies strongly with orbit type. We highlight some prominent groups: (i) a metal-rich ($[\text{Fe}/\text{H}] > -1$), α -rich ($[\alpha/\text{Fe}] > 0.25$) population spread across the first two columns (the high- α disk and in situ halo), (ii) a highly circular ($e < 0.2$), metal-rich ($[\text{Fe}/\text{H}] > -0.75$) population completely confined to the top-left panel (Aleph), (iii) a more eccentric ($e \sim 0.5$), relatively α -poor population adjacent to Aleph in the top-left panel (Sgr), (iv) a highly eccentric ($e > 0.7$), well-populated chemical sequence in the bottom-center panel (GSE), and (v) an $[\text{Fe}/\text{H}] \sim -1.2$ retrograde population in the bottom-right panel (Arjuna).

star formation history and distinct chemical populations recently shown to exist in the core of the Sgr dwarf (Alfaro-Cuello et al. 2019). Stars in the metal-poor ($[\text{Fe}/\text{H}] \lesssim -2$) tail are highly aligned with Sgr in angular momenta as well as in Gaia proper motions (that are independent of the measured distances and radial velocities) and will be a point of focus of Johnson et al. (2020).

3.2.2. Aleph

Aleph⁹ is a hitherto unknown prograde substructure. We discovered Aleph in $[\alpha/\text{Fe}]-[\text{Fe}/\text{H}]$ as a sequence below the high- α disk at similar $[\text{Fe}/\text{H}]$. Examining the dynamics of these stars, we found them to be highly coherent and on circular orbits (Figure 7), comprising the most prograde stars of our sample at higher energy than the high- α disk in $E-L_z$ (Figure 6). Another characteristic feature of Aleph that clearly differentiates it from the canonical disk populations is its significant vertical action, which is seen prominently in Figure 7, where Aleph is completely confined to the top-left panel depicting prograde, $J_z > J_R$ stars. The classic α -rich and α -poor disk sequences typically have $J_z < J_R$ (e.g., Sanders & Binney 2016; Beane et al. 2019; Ting & Rix 2019).

We define Aleph stars as follows:

$$\begin{aligned}
 & (V_\phi < -175 \text{ km s}^{-1}) \wedge (V_\phi > -300 \text{ km s}^{-1}) \\
 & \wedge (|V_r| < 75 \text{ km s}^{-1}) \\
 & \wedge ([\text{Fe}/\text{H}] > -0.8) \wedge ([\alpha/\text{Fe}] < 0.27) \\
 & \wedge (\text{excluding all previously defined structures}). \quad (2)
 \end{aligned}$$

The resulting population is shown in Figure 9. In our sample, Aleph is localized spatially ($r_{\text{gal}} = 11.1^{+5.7}_{-1.6} \text{ kpc}$), with stars extending to 25 kpc. It is a metal-rich ($[\text{Fe}/\text{H}] = -0.51$), relatively alpha-poor ($[\alpha/\text{Fe}] = 0.19$), rapidly rotating ($V_\phi \approx -210 \text{ km s}^{-1}$) structure on a highly circular orbit ($e = 0.13 \pm 0.06$) with a strong vertical action ($\langle J_z \rangle \approx 190 \text{ kpc km s}^{-1}$) and orbits that rise to $|Z_{\text{gal}}| \approx 10 \text{ kpc}$. All quoted values have been weighted by the selection function.

The low eccentricity and chemistry of Aleph suggest an origin within the Galactic disk. Interestingly, in our sample, Aleph is mostly confined to the Galactic anticenter, where several overdensities linked to the excitation of the outer disk (e.g., Monoceros, A13, TriAnd1, TriAnd2) have been observed (e.g., Newberg et al. 2002; Ivezić et al. 2008; Price-Whelan et al. 2015; Li et al. 2017; Bergemann et al. 2018), though our sample is at $|b| > 40^\circ$, at slightly higher latitudes than these features. Several of Aleph’s properties—the radial extent, chemical nature, rotational velocity—are also similar to recently reported features of outer disk stars in Lian et al. (2020). It is possible that the Lian et al. (2020) APOGEE sample is the in-plane view of Aleph, while we are sampling it at higher latitudes. A detailed exploration of Aleph’s nature is the subject of ongoing work.

Aleph is coincident with the enigmatic GC Palomar 1 (Pal 1, red star in Figure 9) in integrals of motion, is at very similar elevation ($Z = 3.6 \text{ kpc}$) and similar metallicity ($[\text{Fe}/\text{H}] \approx -0.5$) but is less α -enhanced (Pal 1: $[\alpha/\text{Fe}] \approx 0$, Aleph: $[\alpha/\text{Fe}] \approx 0.2$). We adopt Pal 1 phase-space coordinates from Baumgardt et al. (2019) and abundances from Sakari et al. (2011). Since its discovery, Pal 1 has been recognized as a curiosity—its high elevation resembles halo GCs but its young

⁹ Named for its prominence in $[\alpha/\text{Fe}]-[\text{Fe}/\text{H}]$; see Figure 7.

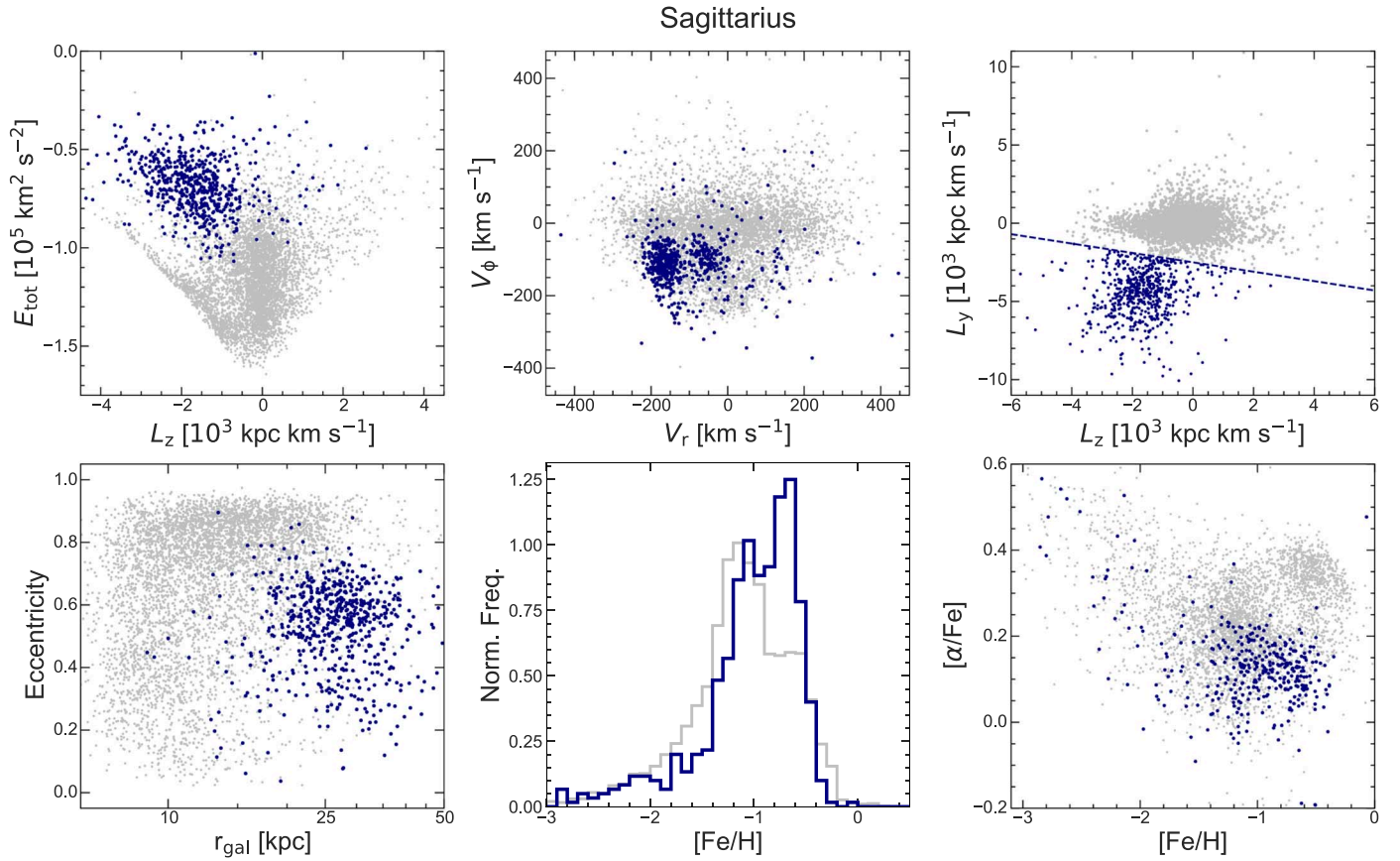


Figure 8. Sagittarius in chemodynamical space. Sgr stars are colored navy blue, and the rest of the sample is shown in gray. Panels are as in Figure 3, except for the top right, which shows the selection plane of L_z – L_y . Because of its relatively recent accretion, Sgr is highly coherent in phase space (first four panels). It forms a striking sequence in L_z – L_y extending to very negative L_y (top-right panel), allowing us to make a clean selection using L_y . The leading and trailing arms are visible in V_r – V_ϕ (top center) at $V_r \approx -50, -175 \text{ km s}^{-1}$. The MDF is multipeaked, with an extended tail to lower metallicity. In $[\text{Fe}/\text{H}]$ vs. $[\alpha/\text{Fe}]$, Sgr is α poor compared to the halo overall, as expected for a galaxy accreted relatively recently that has had more time for enrichment via Type Ia supernovae.

age and high metallicity have proven puzzling (4–7 Gyr, and among the youngest, most metal-rich, and faintest of MW GCs; e.g., van den Bergh & Mackey 2004; Sakari et al. 2011; Sarajedini et al. 2011).

For decades, authors have speculated about its origin, wondering whether it may be an unusually old open cluster, may have a peculiar IMF, or may have been accreted with a dwarf galaxy (e.g., Rosenberg et al. 1998; Niederste-Ostholt et al. 2010). In recent years, the accretion origin has gained currency. Other young (5–8 Gyr), low surface brightness GCs (e.g., Terzan 7, Pal 12, and Whiting 1) have been associated with Sgr, i.e., they are of extragalactic origin (e.g., Carraro et al. 2007; Koposov et al. 2007; Law & Majewski 2010; Johnson et al. 2020). Sakari et al. (2011) analyzed neutron capture elements in four stars in Pal 1 and found them to be distinct from MW field stars, which led them to argue Pal 1 was accreted along with a dwarf galaxy. Pal 1 also does not lie on the in situ branch of MW GCs in the age–metallicity relation (Forbes & Bridges 2010; Forbes 2020; Kruijssen et al. 2020; but see Massari et al. 2019). Whether or not Pal 1 was accreted or born in situ, the similarity between Pal 1 and Aleph in chemodynamical space suggests a common origin.

3.2.3. High- α Disk and In Situ Halo

It has long been known that stars on disk-like orbits lie on one of two chemical sequences characterized by low or high values of $[\alpha/\text{Fe}]$ (e.g., Edvardsson et al. 1993; Fuhrmann 1998;

Chen et al. 2000; Bensby et al. 2003; Adibekyan et al. 2012). With Gaia data, it was realized that the high- α population extends to higher eccentricities than a conventional disk-like population. This high- α , high-eccentricity population has been dubbed the “in situ halo” and later as the “Splash” (e.g., Bonaca et al. 2017, 2020; Haywood et al. 2018; Di Matteo et al. 2019; Amarante et al. 2020; Belokurov et al. 2020). Simultaneously, a link between the accretion of GSE, the formation of the high- α disk, and the creation of the in situ halo has been proposed (e.g., Helmi et al. 2018; Gallart et al. 2019; Belokurov et al. 2020; Bonaca et al. 2020). Characterizing this component of the halo is thus critical to understanding the Galaxy’s earliest epoch.

We define the high- α disk and in situ halo stars relying purely on chemistry:

$$[\alpha/\text{Fe}] > 0.25–0.5 ([\text{Fe}/\text{H}] + 0.7) \wedge (\text{excluding all previously defined structures}). \quad (3)$$

In Figure 10, we see these stars form a kinematic population that extends continuously from rotationally supported orbits (forming a locus at lower $|V_\phi|$ than Aleph) to highly eccentric ones. In E – L_z the high- α disk forms a more diffuse track slightly steeper than Aleph, which extends into high-eccentricity orbits with $L_z \sim 0$. The continuity of the distribution in phase space supports scenarios in which the ancient, rotationally supported high- α disk was dynamically heated, perhaps by a merger. The in situ halo extends to $r_{\text{gal}} \approx 25 \text{ kpc}$, but we

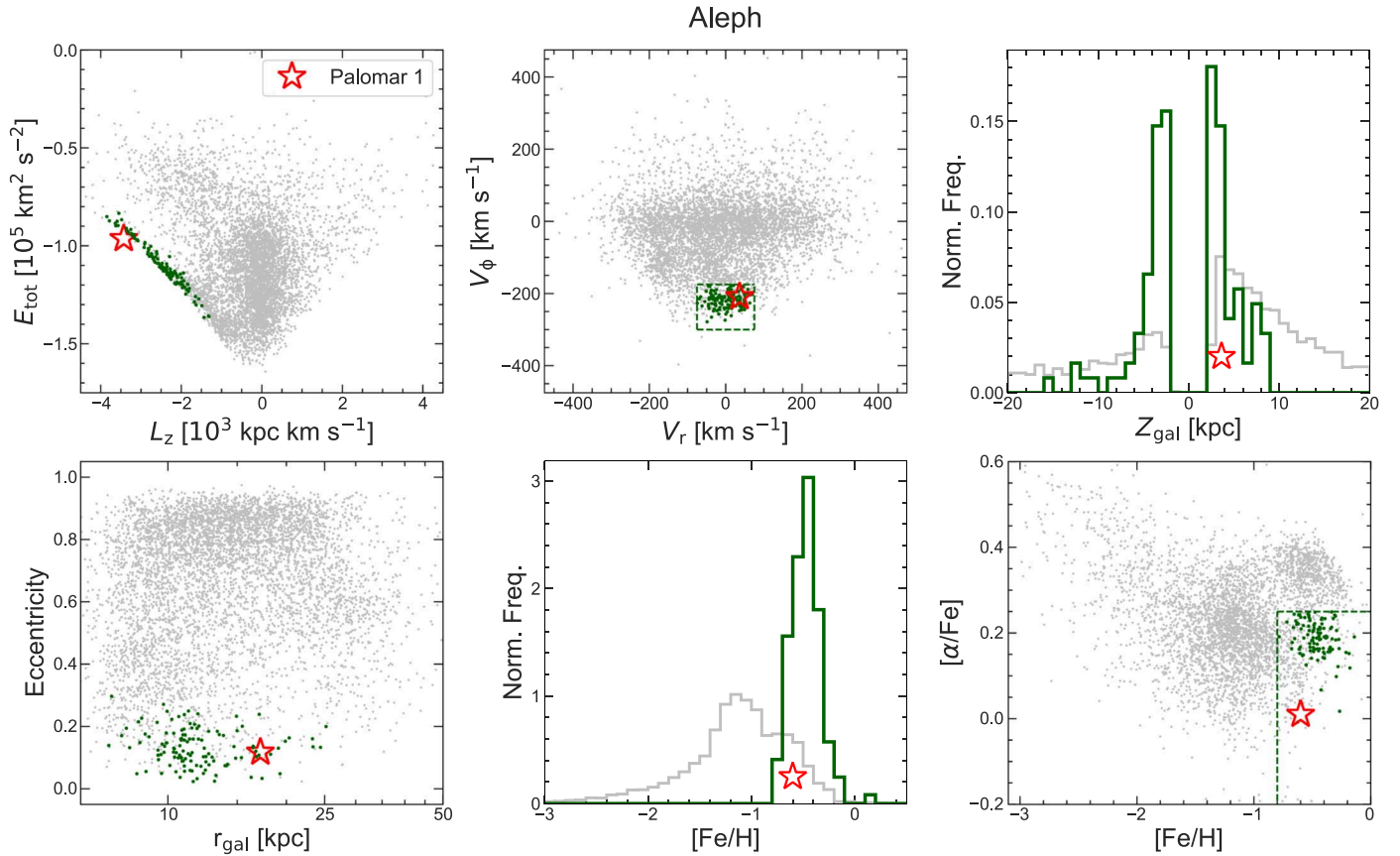


Figure 9. Aleph (dark green) in chemodynamical space. Panels are as in Figure 3, except for the top right, which shows the distribution of Z_{gal} . Dashed green lines indicate the selection planes (V_r – V_ϕ , and $[\alpha/\text{Fe}]$ vs. $[\text{Fe}/\text{H}]$). The globular cluster Palomar 1 is represented in red. Aleph is rapidly rotating, circular ($e < 0.3$), metal rich, and relatively α poor. It is at higher energy than the high- α disk and is clearly distinct in chemistry (see also the top-left panel of Figure 7). Aleph extends up to ≈ 10 kpc off the plane. Palomar 1 and Aleph share many chemodynamical properties in common, suggesting a possible association.

caution that the stars at $|Z| > 15$ kpc lie very close to the selection boundary in chemistry and may belong to other structures. We discuss the physical origin of the in situ halo further in Section 4.2.

This selection excludes the metal-poor tail of the high- α disk and the in situ halo (e.g., Carollo et al. 2019) which lies in a region of $[\text{Fe}/\text{H}]$ versus $[\alpha/\text{Fe}]$ coincident with GSE and other accreted structures. We will return to these stars in the sections dealing with the MWTD (Section 3.2.9) and the unclassified debris (Section 3.2.10).

3.2.4. Gaia–Sausage–Enceladus (GSE)

We define “GSE” as the highly radial population that comprises the bulk of the accreted local halo. This population was identified in various ways by Belokurov et al. (2018), Koppelman et al. (2018, 2019a), Myeong et al. (2018b), Haywood et al. (2018), Helmi et al. (2018), Mackereth et al. (2019), and Helmi (2020). Different selections result in differing degrees of contamination with overlapping structures (see discussion in Evans 2020).

We select GSE stars by excluding previously defined structures and requiring $e > 0.7$. The eccentricity selection is motivated by the dense cloud of stars at $e > 0.7$ seen in eccentricity versus r_{gal} , whose density sharply drops off at ≈ 30 kpc (corresponding to the proposed apocenter of GSE; Deason et al. 2018; Lancaster et al. 2019). Our GSE selection is

therefore simply

$$(e > 0.7) \wedge (\text{excluding all previously defined structures}). \quad (4)$$

This selection is very similar in spirit to the V_r – V_ϕ selection in Belokurov et al. (2018), where this structure was discovered, as borne out by the second panel of Figure 11. The morphology of selected stars in E – L_z is reasonable for a massive dwarf ($M_{\text{halo}} \gtrsim 10^{11} M_\odot$), the bulk of whose debris is predicted to be radialized to low $|L_z|$ orbits (Bullock & Johnston 2005; Amorisco 2017; Pfeffer et al. 2020, Appendix A). This selection is by no means perfect—it is incomplete in that it misses the low-eccentricity tail of GSE at $e < 0.7$ that manifests as a strong peak at $[\text{Fe}/\text{H}] \approx -1.2$ in subsequent plots. And it is impure, as suggested by the structure along the margins of GSE in E – L_z —for instance, $e > 0.7$ stars from Wukong (discussed in Section 3.2.8) are apparent at $L_z/[10^3 \text{ kpc km s}^{-1}] \sim -0.5$. A subtle sequence corresponding to residue from Wukong also appears under the GSE sequence in $[\text{Fe}/\text{H}]$ versus $[\alpha/\text{Fe}]$. However, the very well-behaved, unimodal MDF inspires confidence that this selection overwhelmingly comprises GSE stars.

The MDF is narrow—corrected for the selection function, 85% of stars are contained within 0.9 dex in $[\text{Fe}/\text{H}]$ —and reminiscent of some local dwarfs (e.g., Leo I and Fornax, Kirby et al. 2013). Like Leo I and Fornax, the GSE MDF is well fit by a simple, analytical, chemical evolution model, namely the “Best Accretion Model” (Lynden-Bell 1975) used

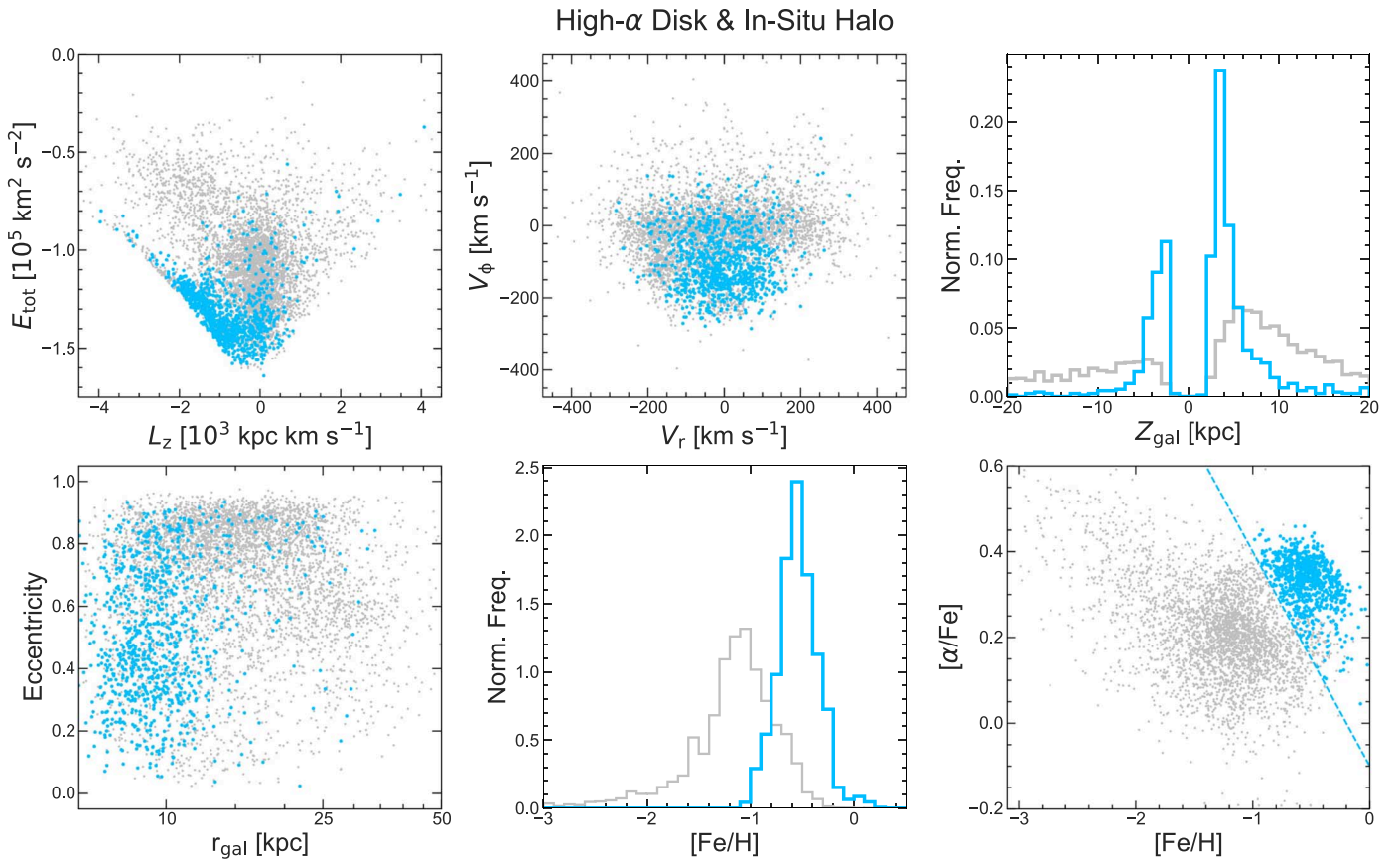


Figure 10. High- α disk and in situ halo (light blue) in chemodynamical space. Panels are as in Figure 3, except for the top right, which shows the distribution of Z_{gal} – $[\text{Fe}/\text{H}]$ vs. $[\alpha/\text{Fe}]$ is the selection plane. Stars with chemistry resembling the high- α disk span the full range of eccentricities. In E – L_z , the rotationally supported stars form the diffuse, inclined sequence while the eccentric stars have $L_z \sim 0$. In V_r – V_ϕ , the low-eccentricity stars lie at negative V_ϕ while the eccentric stars lie on the $V_\phi \sim 0$ locus coincident with GSE. The in situ halo extends all the way out to a remarkable $r_{\text{gal}} \approx 25$ kpc and $|Z_{\text{gal}}| \approx 20$ kpc.

in Kirby et al. (2011, 2013), that explains all features, including the extended metal-poor tail (dotted line in MDF panel of Figure 11). This model is a generalization of traditional leaky box models, allowing for the accretion of fresh gas and has two parameters— M , the ratio between the final mass and initial gas mass of the system, and p , the effective yield (i.e., a measure of the fraction of metals produced by stars the system retains)—for which we find best-fit values of $p = 0.085$, $M = 3.28$ (slightly different from Conroy et al. 2019b who found $p = 0.08$, $M = 2.1$ for a differently selected, $\text{S/N} > 5$ kinematic halo sample at $-0.5 < L_z/[10^3 \text{ kpc km s}^{-1}] < 1$). As in the case of both Fornax and Leo I in Kirby et al. (2013), the data falls off more steeply than the model on the metal-rich side of the MDF.

Our estimate of GSE’s metallicity ($[\text{Fe}/\text{H}] = -1.15^{+0.24}_{-0.33}$, weighted) is ≈ 0.1 – 0.2 dex higher than most of the literature (e.g., Helmi et al. 2018; Mackereth et al. 2019; Matsuno et al. 2019; Sahlholdt et al. 2019; Vincenzo et al. 2019) and more in line with the recent $[\text{Fe}/\text{H}] = -1.17 \pm 0.34$ estimate of Feuillet et al. (2020). To convert $[\text{Fe}/\text{H}] = -1.15$ to a mass estimate, we use the mass–metallicity relation from local dwarfs (Kirby et al. 2013) and account for the redshift evolution of the relation—i.e., higher masses at higher redshift at fixed $[\text{Fe}/\text{H}]$ (e.g., Steidel et al. 2014; Zahid et al. 2014; Sanders et al. 2015; Ma et al. 2016a; Torrey et al. 2019). Assuming the trend from the FIRE simulations, Ma et al. (2016b), which agrees well with observations out to $z \sim 3$, produces $M_* = 4$ – $7 \times 10^8 M_\odot$ for accretion redshifts between

$z = 1.3$ (Kruijssen et al. 2020) and $z = 2$ (Bonaca et al. 2020). This is in excellent agreement with recent estimates from GSE’s GC age–metallicity relation (≈ 2 – $4 \times 10^8 M_\odot$; Kruijssen et al. 2020), star counts of $[\text{Fe}/\text{H}] < -1$, $e > 0.7$ APOGEE red giants (≈ 2 – $5 \times 10^8 M_\odot$; Mackereth & Bovy 2020), and the integrated star formation rate of a chemical evolution model ($\approx 6 \times 10^8 M_\odot$; Fernández-Alvar et al. 2018; Helmi et al. 2018).

We are also in a position to address the mean rotational velocity of GSE, which is of interest because it informs the initial configuration of the merger. We find $\langle V_\phi \rangle = 1.04^{+1.26}_{-1.25} \text{ km s}^{-1}$, $\langle L_z \rangle = 4.7^{+20.1}_{-10.5} \text{ kpc km s}^{-1}$ with errors estimated via bootstrap resampling including fully propagated errors from distance and PM samples, and weighting for the selection function. This measurement places a very strong constraint on the lack of net rotation of GSE. This conclusion is in excellent agreement with Belokurov et al. (2020), who report $\langle V_\phi \rangle \sim 0$ for the “Sausage” component in their velocity ellipsoid fits for a local sample drawn from Sanders & Das (2018) with $6.5 < R_{\text{gal}} < 10$ kpc. The magnitude of rotation we measure is much lower than Mackereth et al. (2019), who find $L_z = 176 \text{ kpc km s}^{-1}$ using 673 APOGEE stars at $|Z| < 10$ kpc with spectrophotometric distances uncertain on the $\sim 15\%$ level, and Helmi (2020), who report $\langle V_\phi \rangle (d_{\text{helio}} < 1 \text{ kpc}) = 21.1 \pm 1.8 \text{ km s}^{-1}$ using 6 stars and $\langle V_\phi \rangle (d_{\text{helio}} < 2 \text{ kpc}) = 16.1 \pm 2.8 \text{ km s}^{-1}$ using 23 stars from the Gaia RVS sample cross-matched with APOGEE $[\text{Fe}/\text{H}] \geq -1.3$ stars. We caution that this measurement is sensitive to the assumed

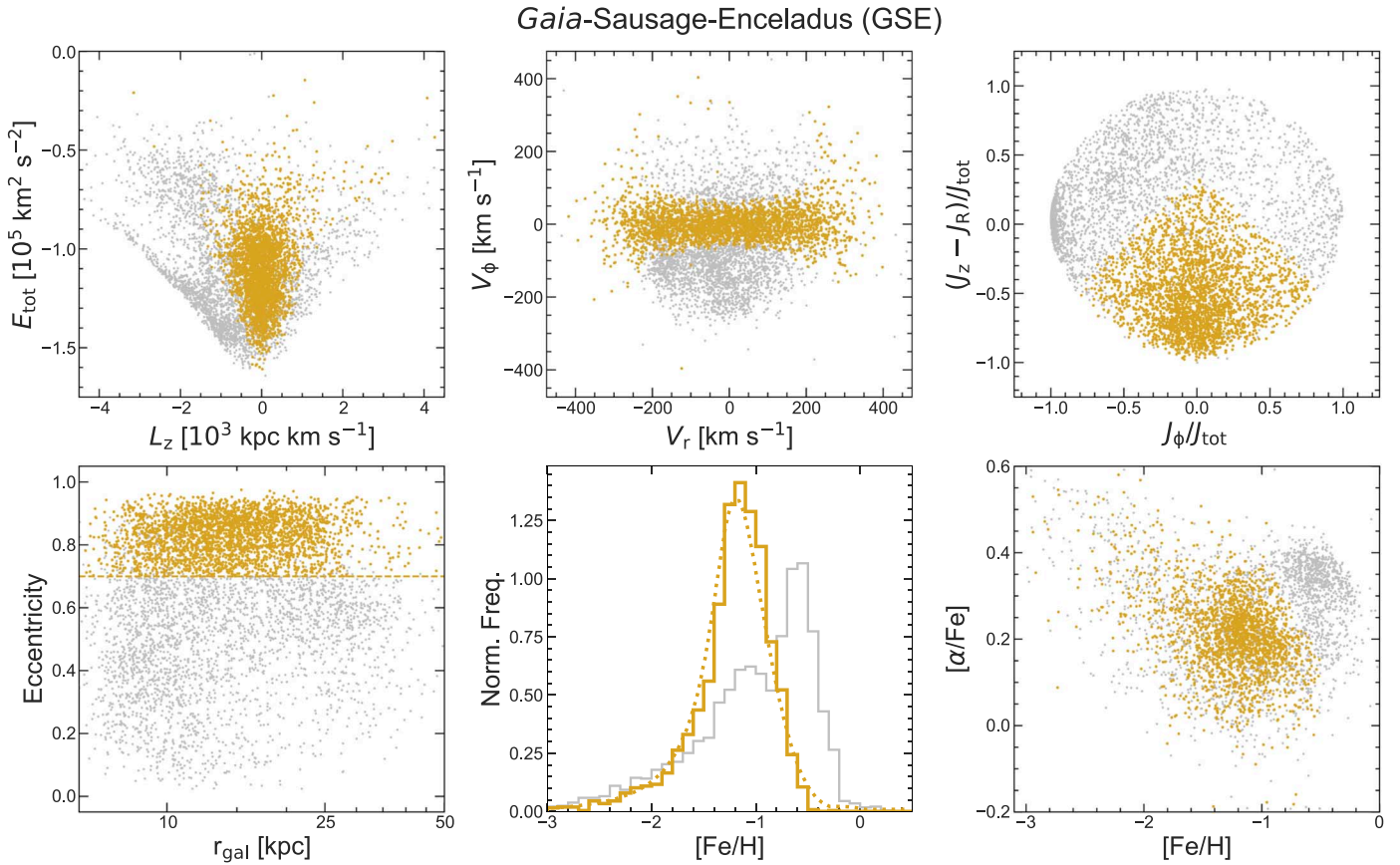


Figure 11. Gaia–Sausage–Enceladus (GSE, gold) in chemodynamical space. Panels are as in Figure 3, except for the top right, which shows the distribution of stars in action space. GSE is selected on eccentricity ($e > 0.7$) motivated by the dense population of stars in the bottom-left panel. The smooth, unimodal MDF is well fit by a simple chemical evolution model (dotted line in the MDF panel) that also reproduces the tail to low [Fe/H]. The highly eccentric GSE stars map to various projections of phase space as overdensities at $L_z \sim 0$, $V_\phi \sim 0$, and $J_z - J_R < 0$.

solar motion and that the mentioned GSE samples have all been selected differently. We also observe that including Sequoia, Arjuna, or Arjuna and Sequoia (retrograde structures discussed in Section 3.2.7) in GSE results in $\langle V_\phi \rangle = [3.7^{+1.3}_{-1.3}, 7.0^{+1.6}_{-1.5}, 9.4^{+1.7}_{-1.6}] \text{ km s}^{-1}$, respectively. Despite these caveats, it is clear that GSE is far from highly retrograde. We further discuss the rotation of the halo in Section 4.3.

3.2.5. Helmi Streams

The Helmi Streams were among the first bona fide accreted substructures discovered in the halo via integrals of motion as opposed to on-sky streams (Helmi et al. 1999). Koppelman et al. (2019a, 2019b), Koppelman & Helmi (2020) provide an updated view of these streams using Gaia DR2 data.

While a prominent $E - L_z$ overdensity corresponding to the Helmi Streams appears among the H3 dwarfs, it is not as readily apparent in the giants, though there is a hint of a vertical spur at $L_z/[10^3 \text{ kpc km s}^{-1}] \sim -1.5$ in, e.g., Figure 4. To select the Helmi Streams, we rely on the $L_z - L_\perp$ selection in Koppelman et al. (2019a, “Box B,” their Figure 2):

$$\begin{aligned} & (-1.7 < L_z/[10^3 \text{ kpc km s}^{-1}] < -0.75) \\ & \wedge (1.6 < L_\perp/[10^3 \text{ kpc km s}^{-1}] < 3.2) \\ & \wedge (\text{excluding all previously defined structures}). \end{aligned} \quad (5)$$

The selected stars are shown in Figure 12. Orbits of the Helmi Streams in local samples (Helmi 2020, their Figure 12) rise to high latitudes and extend out to $R_{\text{gal}} \approx 25 \text{ kpc}$ —this is

borne out in Figure 12. The large spread in eccentricity mirrors the large spread in eccentricities of GCs attributed to Helmi Streams (HS) from considerations of the GC age–metallicity relation (Massari et al. 2019; Forbes 2020; Kruijssen et al. 2020). In the MDF, we see a broad distribution, consistent with the complex population with an extended star formation history modeled in Koppelman et al. (2019b). The distribution in [Fe/H] versus $[\alpha/\text{Fe}]$ traces the typical trend of decreasing $[\alpha/\text{Fe}]$ with increasing [Fe/H] expected in halo populations. Assuming accretion redshifts of $z \sim 0.5–1.1$, i.e., 5–8 Gyr ago (Koppelman et al. 2019b) and a (weighted) mean metallicity of $[\text{Fe}/\text{H}] \approx -1.3$, we estimate the Helmi Streams to have a stellar mass of $M_\star \approx 0.5–1 \times 10^8 M_\odot$ via the Kirby et al. (2013) MZR and its expected evolution to higher redshifts (Ma et al. 2016b), in excellent agreement with Koppelman et al. (2019b).

3.2.6. Thamnos

The Thamnos structure was recently discovered in Koppelman et al. (2019a). These authors found two overdensities in chemodynamical space (“Thamnos 1” and “Thamnos 2”) that they attribute to the same progenitor. An overdensity corresponding to their proposed structure appears in our $E - L_z$ diagrams as a jagged ridge along the retrograde edge of GSE (at $E_{\text{tot}}/[10^5 \text{ km}^2 \text{ s}^{-2}] \approx -1.4$). This ridge resembles the corrugations of a single massive satellite producing multiple overdensities in $E - L_z$ and other phase-space diagrams (Jean-Baptiste et al. 2017).

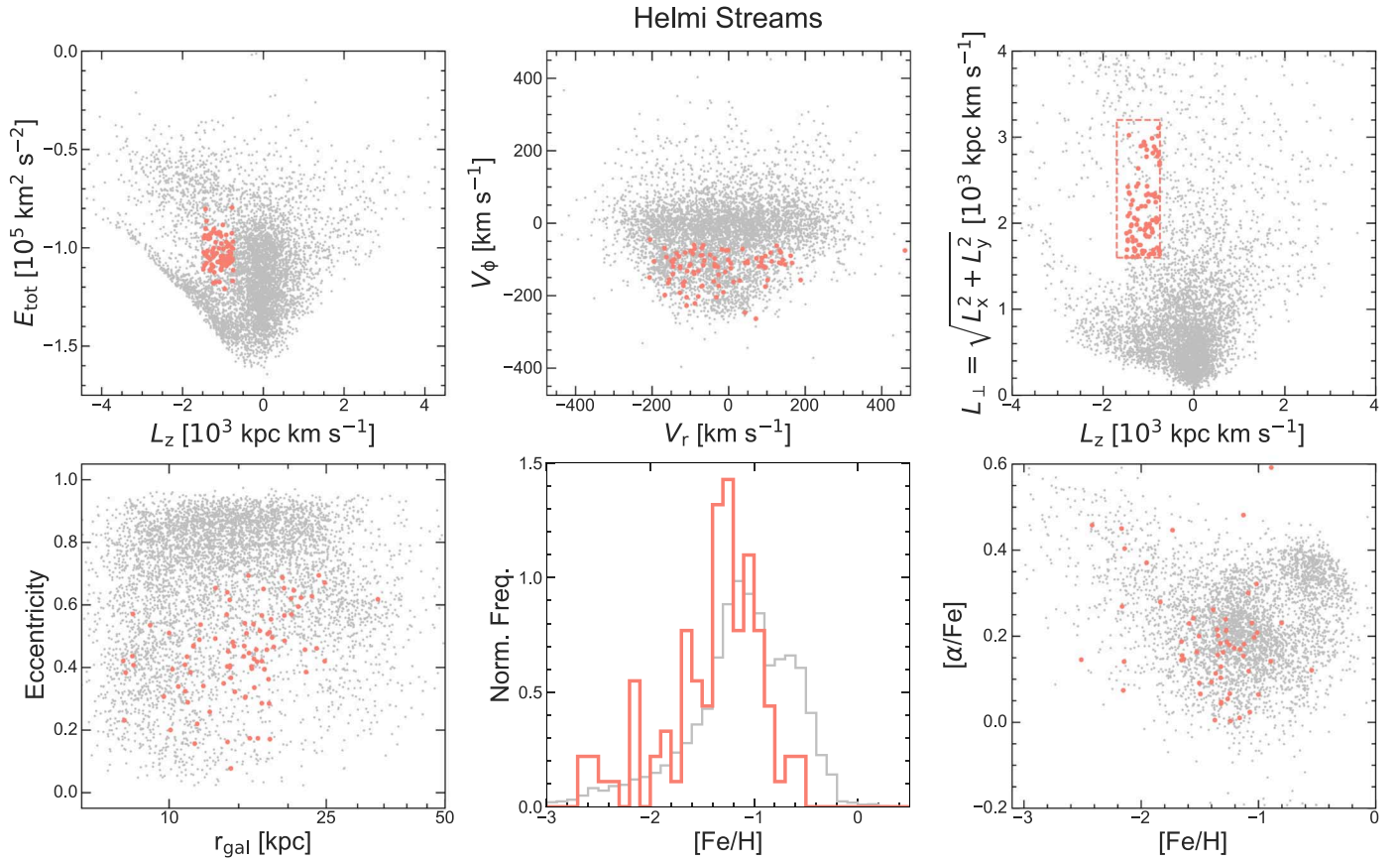


Figure 12. The Helmi Streams (salmon pink) in chemodynamical space. Panels are as in Figure 3, except for the top right, which shows the HS selection plane $L_z - L_{\perp}$. We follow Koppelman et al. (2019b) to define our selection. The Helmi Streams extend to ≈ 25 kpc, in line with expectations from orbit integration of high-energy stars in local studies (Helmi 2020). The multimodal MDF and complex $[\text{Fe}/\text{H}]$ vs. $[\alpha/\text{Fe}]$ morphology suggest a complex star formation history and/or more than one subpopulation.

To distinguish whether Thamnos is a remnant of a distinct satellite or a part of GSE, it is important to verify that the chemistry of Thamnos is distinct from GSE, particularly because of the small sample (~ 20) of Thamnos stars with abundances in Koppelman et al. (2019a), the majority of which overlap with GSE within error bars (their Figure 4).

To define our Thamnos selection, we begin by selecting all stars at $(L_z > 0.2) \wedge (-1.5 < E_{\text{tot}} < -1.3)$. The $E - L_z$ selection is motivated by the contours for Thamnos provided in Koppelman et al. (2019a) as well as the overdensity we see in that region. In this energy range, we expect high contamination primarily from GSE. The resulting MDF depicted with a dashed line in Figure 13 shows a strong peak at $[\text{Fe}/\text{H}] = -1.9$ that we attribute to Thamnos as well as a second peak corresponding to GSE's metallicity of $[\text{Fe}/\text{H}] \approx -1.2$. We further refine the Thamnos selection informed by this MDF by restricting the selection to $[\text{Fe}/\text{H}] < -1.6$, where we see a break. This results in a final selection of 32 stars that produces a clean $[\text{Fe}/\text{H}]$ – $[\alpha/\text{Fe}]$ sequence. To summarize, the Thamnos selection is

$$\begin{aligned}
 & (0.2 < L_z / [10^3 \text{kpc km s}^{-1}] < 1.5) \\
 & \wedge (-1.5 < E_{\text{tot}} / [10^5 \text{km}^2 \text{s}^{-2}] < -1.3) \\
 & \wedge ([\text{Fe}/\text{H}] < -1.6) \\
 & \wedge (\text{excluding all previously defined structures}). \quad (6)
 \end{aligned}$$

Koppelman et al. (2019a) estimate Thamnos' stellar mass to be $< 5 \times 10^6 M_{\odot}$ by comparing its extent in $E - L_z$ against a suite of simulations. Thamnos lies at lower energy than GSE, which is unexpected for a system of such low stellar mass if it were accreted at $z \sim 0$, as its would be shredded in the outer reaches of the halo (e.g., Amorisco 2017; Pfeffer et al. 2020). This suggests that it was accreted very early when the Galaxy was not very massive or perhaps simultaneously with GSE at $z \sim 1.3$ –2 (Bonaca et al. 2020; Kruijssen et al. 2020). Now that we have a good handle on the metallicity ($[\text{Fe}/\text{H}] = -1.9$), we can provide a complementary mass–metallicity relation (MZR) constraint on the mass. Using the $z = 0$ Kirby et al. (2013) relation for $[\text{Fe}/\text{H}]$ produces a mass $2 \times 10^5 M_{\odot}$, but this is a strict lower limit. This is because we must account for the redshift evolution of the MZR. Assuming the trend from the FIRE simulations (Ma et al. 2016b), which agree well with observations out to $z \sim 3$ and predict a ~ 1 dex increase in mass for an $[\text{Fe}/\text{H}] = -1.9$ galaxy between $z = 0$ and $z = 1.5$, we find $M_{\star} \approx 2 \times 10^6 M_{\odot}$ for Thamnos, in good agreement with Koppelman et al. (2019a).

Thamnos is potentially a very exciting object because of its very low stellar mass that we estimate here, and because it lies so deep in the potential. Put another way, the debris from Thamnos lies only at $d_{\text{helio}} \approx 6$ kpc (weighted), can be easily targeted using our clean sample, and thus offers a unique view of galaxy evolution (e.g., stellar abundances) in a mass regime

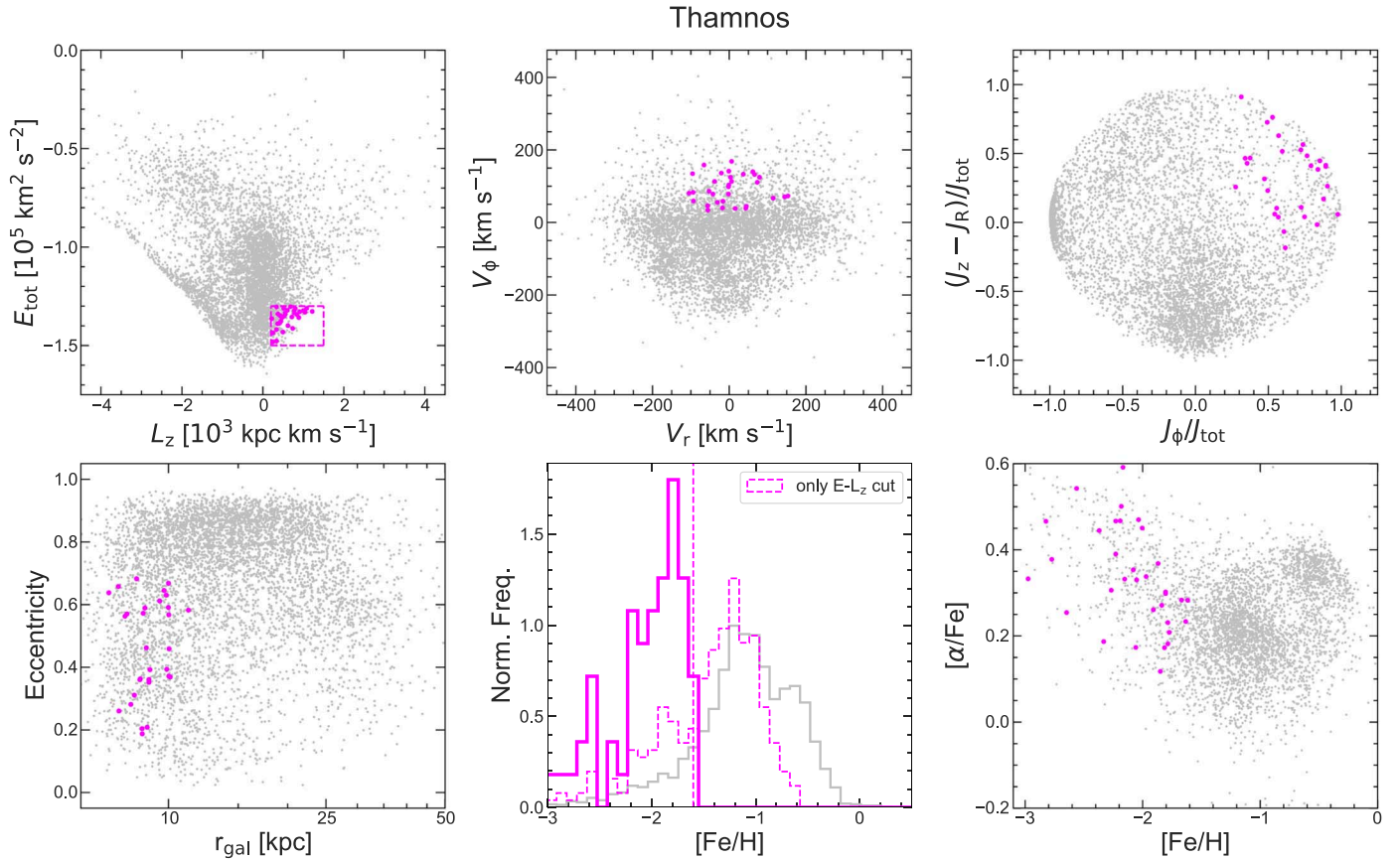


Figure 13. Thamnos (fuchsia) in chemodynamical space. Panels are as in Figure 11. The initial selection is in $E - L_z$ with a further cut in $[\text{Fe}/\text{H}]$ to refine the sample. The MDF for only the $E - L_z$ cut is shown in dashed lines—two populations corresponding to GSE ($[\text{Fe}/\text{H}] = -1.2$) and Thamnos ($[\text{Fe}/\text{H}] = -1.9$) are visible. In the final panel, we see a metal-poor, α -rich sequence as expected for a low-mass dwarf galaxy accreted at high-redshift.

that will be out of reach even for the James Webb Space Telescope at high redshift (e.g., Weisz et al. 2014; Boylan-Kolchin et al. 2015, 2016).

3.2.7. The High-energy Retrograde Halo: Arjuna, Sequoia, and I'itoi

Studies of the local stellar halo have found a wealth of retrograde substructure (e.g., Helmi et al. 2017; Myeong et al. 2018a, 2018c, 2018d, 2019; Koppelman et al. 2019a; Matsuno et al. 2019; Yuan et al. 2020b). Debris of the Sequoia dwarf galaxy (Myeong et al. 2018c, 2019; Matsuno et al. 2019) dominates the local retrograde halo at higher energies while Thamnos (Koppelman et al. 2019a) resides at lower energy. In this section, we turn our attention to the high-energy retrograde halo (i.e., at higher energies than Thamnos) that we select as follows:

$$\begin{aligned}
 (\eta > 0.15) \wedge (L_z/[10^3 \text{ kpc km s}^{-1}] > 0.7) \\
 \wedge (E_{\text{tot}}/[10^5 \text{ km}^2 \text{ s}^{-2}] > -1.25) \\
 \wedge (\text{excluding all previously defined structures}). \quad (7)
 \end{aligned}$$

The circularity, $\eta = L_z/|L_{z,\text{max}}(E_{\text{tot}})|$, where $L_{z,\text{max}}(E_{\text{tot}})$ is the maximum L_z achievable for an orbit of energy E_{tot} . We compute $L_{z,\text{max}}(E_{\text{tot}})$ by assuming a perfectly circular orbit with the star's r_{gal} and total 3D velocity. The circularity condition, $\eta > 0.15$, ensures a generous selection of retrograde orbits, $L_z/[10^3 \text{ kpc km s}^{-1}] > 0.7$ reduces contamination from GSE, and the energy limit avoids Thamnos. The stars satisfying this selection are shown in Figure 14.

A prominent peak in the high-energy retrograde MDF appears exactly where expected for Sequoia at $[\text{Fe}/\text{H}] \approx -1.6$ (Matsuno et al. 2019; Monty et al. 2019; Myeong et al. 2019). More surprisingly, two other distributions are apparent in the MDF—one centered at $[\text{Fe}/\text{H}] \approx -1.2$, and another spanning very low metallicity at $[\text{Fe}/\text{H}] < -2$. Furthermore, these stars occupy a complex distribution in $[\text{Fe}/\text{H}] - [\alpha/\text{Fe}]$ that is suggestive of multiple populations. We name the metal-rich population “Arjuna”¹⁰ and the metal-poor sequence “I’itoi.”¹¹ Based on the peaks and breaks in the MDF, we define Arjuna stars as those with $[\text{Fe}/\text{H}] > -1.5$, Sequoia stars as those with $-2 < [\text{Fe}/\text{H}] < -1.5$, and the remaining stars at $[\text{Fe}/\text{H}] < -2$ as belonging to I’itoi.

Contrary to expectations from local studies (e.g., Koppelman et al. 2019a; Myeong et al. 2019), Sequoia is not the dominant component of the high-energy retrograde halo—it has fewer than half as many stars as Arjuna. This raises the question as to why Arjuna was missed in the local studies that found Sequoia. The answer may lie in its spatial extent—Arjuna lies at larger distances compared to Sequoia (median $r_{\text{gal}} \sim 25$ kpc versus ~ 15 kpc, weighted), and stars with apocenters of 25 kpc are

¹⁰ Arjuna is named for the legendary archer from the Indian epic, the Mahabharata. Arjuna extends to high energy, mirroring Sagittarius (Latin for archer) on the prograde side.

¹¹ I’itoi (pronounced “ee ee thoy”) is named for the “man in the maze” who features in creation legends of the Tohono O’odham people. Our survey telescope, the MMT Observatory, stands on the ancestral lands of the Tohono O’odham. Further, I’itoi is said to reside in a cave adjacent to a mountain, paralleling the location of I’itoi in $E - L_z$ with respect to GSE (Enceladus is entombed within Mt. Etna in Sicily).

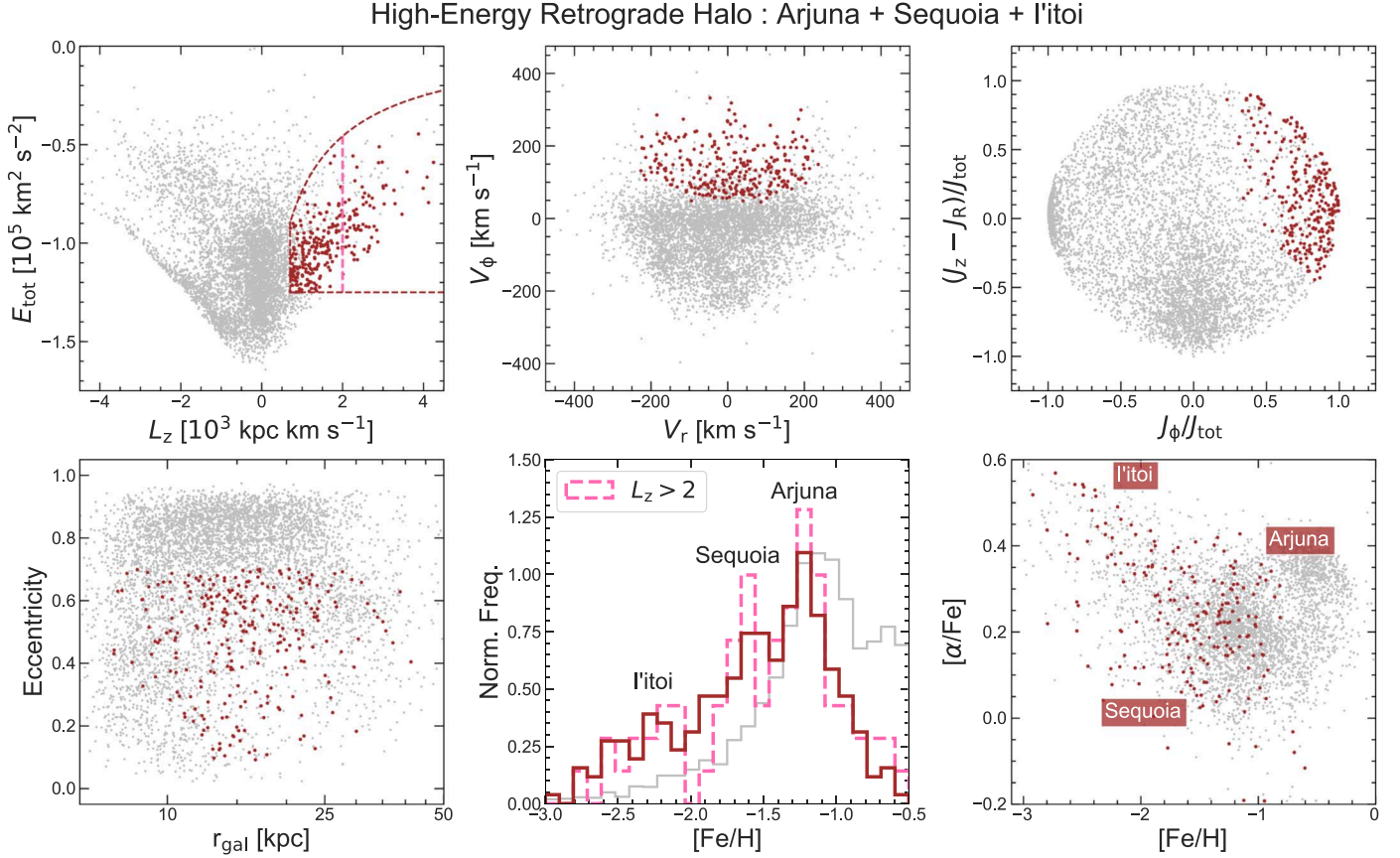


Figure 14. The high-energy retrograde halo (brown) in chemodynamical space. Panels are as in Figure 11. Brown dashed lines in the $E-L_z$ panel depict the selection (see Equation (7)). The resulting MDF shows three peaks at $[\text{Fe/H}]$ of $-1.2, -1.6, <-2$ that we identify as Arjuna, Sequoia, and I'itoi, respectively. Imposing a conservative $L_z/[10^3 \text{ kpc km s}^{-1}] > 2$ selection also produces a similarly shaped MDF with a more pronounced I'itoi peak (dashed pink). We display a summary of actions (top right) similar to the diagram in which Sequoia was discovered (Myeong et al. 2019). Those authors identified Sequoia as belonging to the bottom-right quadrant of this action diagram. In the bottom-left panel, we see that Arjuna, Sequoia, and I'itoi are quite eccentric ($\langle e \rangle \approx 0.5-0.6$) and extend to ≈ 40 kpc.

relatively rare in the solar neighborhood compared to those with apocenters of 15 kpc.

Given that Arjuna may prove to be a massive component of the halo, and because of its similarity in $[\text{Fe/H}]$ to GSE, it is important to discuss possible connections to GSE. Recent work has also cast doubt on the status of Sequoia as a dwarf galaxy and argued that it may be debris from the outer reaches of GSE (Koppelman et al. 2019a; Helmi 2020). We explore this issue in Figure 14. We show that even when restricting the retrograde selection to very high $L_z/[10^3 \text{ kpc km s}^{-1}] > 2$, far from the $L_z \approx 0$ overdensity defined by GSE, the peaks in the MDF associated with Arjuna and Sequoia remain. None of the existing studies of GSE show a significant $[\text{Fe/H}] \approx -1.2$ population at such high L_z , with stars outnumbering those from Sequoia (e.g., Belokurov et al. 2018; Koppelman et al. 2019a; Mackereth et al. 2019; Myeong et al. 2019; Helmi 2020). So Arjuna may either be a hitherto unknown extension of GSE to highly retrograde orbits (such high L_z extensions exist for the largely eccentric debris of massive, $M_\star > 10^8 M_\odot$, accreted galaxies in the Bullock & Johnston 2005 halos), or it may be the debris of a distinct dwarf galaxy. As for Sequoia, any attempt to tie both Arjuna and Sequoia to GSE must account for $L_z/[10^3 \text{ kpc km s}^{-1}] > 2$ components of GSE as well as the spread in abundances (e.g., by appealing to a steep metallicity gradient or multiple populations). More detailed modeling of a GSE-like merger (in the vein of Bignone et al. 2019; Vincenzo et al. 2019; Elias et al. 2020) is required to understand if it is

possible for a single progenitor to simultaneously populate such disparate regions of phase space as well as chemistry.

The proximity of I'itoi and Thamnos in $[\text{Fe/H}]$ versus $[\alpha/\text{Fe}]$ may indicate these structures are related—however, I'itoi is prominent at $L_z/[10^3 \text{ kpc km s}^{-1}] > 2$ and Thamnos' mass argues against such a wide extent in $E-L_z$ (Koppelman et al. 2019a, their Figure 5). This is because low-mass structures are typically compact and experience similar dynamical friction across all their stars, compared to larger structures like GES. I'itoi may also be the metal-poor tail of Arjuna and/or Sequoia—more work needs to be done to differentiate these three structures in phase space as well. This will be particularly challenging due to the error vector in $E-L_z$ and similar spaces that dramatically scatter structures with high angular momentum (see Appendix A), highlighting the importance of leveraging chemistry in this region of phase space. We defer detailed characterization of these structures to forthcoming work.

3.2.8. Wukong

Here we present Wukong,¹² a hitherto unknown prograde structure, that appears as a pair of overdensities in $E-L_z$

¹² Named for Sun Wukong, the celestial Monkey King from the *Journey to the West*. Sun Wukong is imprisoned under a mountain by the Buddha for his uprising against Heaven and is later set free by the scholar Tripitaka. We play the role of the scholar here, setting Wukong free from underneath Gaia-Sausage-Enceladus (Enceladus is entombed within Mt. Etna in Sicily).

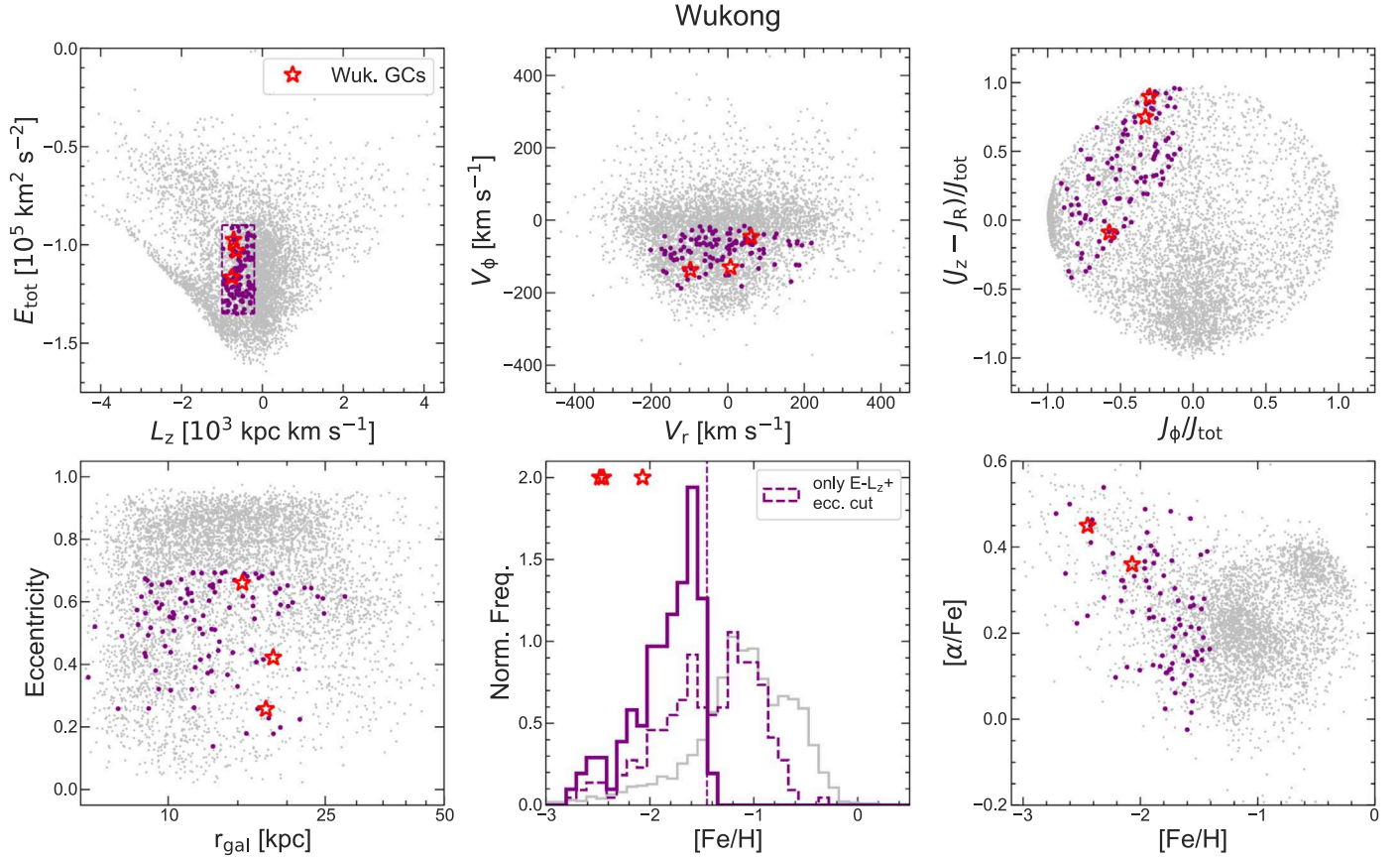


Figure 15. Wukong (purple) in chemodynamical space. Panels are as in Figure 11. Wukong is initially selected in $E-L_z$ (box in top-left panel). A further cut is made in $[\text{Fe}/\text{H}]$ based on the break in the resulting MDF (dashed histogram) at $[\text{Fe}/\text{H}] \approx -1.45$. Wukong stars have high J_z , show a broad spread in eccentricity characteristic of more massive accreted structures like Sequoia and the Helmi Streams, and are contained within ≈ 25 kpc. Three metal-poor GCs—ESO 280-SC06 ($[\text{Fe}/\text{H}] = -2.5$), NGC 5024 ($[\text{Fe}/\text{H}] = -2.1$), NGC 5053 ($[\text{Fe}/\text{H}] = -2.5$)—satisfy our Wukong selection and are shown as red stars in all panels ($[\alpha/\text{Fe}]$ is not available for ESO 280-SC06).

$(E_{\text{tot}}/[10^5 \text{ km}^2/\text{s}^2] = -1.1, -1.3)$, lining the prograde margin of GSE. In Appendix B, we show these clumps to be even more pronounced in the McMillan (2017) potential. We select Wukong as follows:

$$\begin{aligned}
 & (-1 < L_z/[10^3 \text{ kpc km s}^-1] < -0.2) \\
 & \wedge (-1.35 < E_{\text{tot}}/[10^5 \text{ km}^2/\text{s}^2] < -0.9) \\
 & \wedge ([\text{Fe}/\text{H}] < -1.45) \\
 & \wedge (\text{excluding all previously defined structures}). \quad (8)
 \end{aligned}$$

The conditions in $E-L_z$ draw a box around the overdensities and extend it inwards toward GSE. The $[\text{Fe}/\text{H}]$ selection is motivated by the MDF resulting from the $E-L_z$ cut (dashed histogram in MDF panel of Figure 15) that shows multiple peaks at $[\text{Fe}/\text{H}] = -1.2$ (GSE), -1.6 , -1.9 , and a break at ≈ -1.45 . This leaves us with a sample of 111 Wukong stars that form a sequence in $[\text{Fe}/\text{H}]$ versus $[\alpha/\text{Fe}]$.

Three metal-poor GCs—NGC 5024 ($[\text{Fe}/\text{H}] = -2.1$), NGC 5053 ($[\text{Fe}/\text{H}] = -2.5$), ESO 280-SC06 ($[\text{Fe}/\text{H}] = -2.5$)—satisfy all the selection criteria in Equation (8) and may have been accreted along with Wukong (phase-space parameters from Baumgardt et al. 2019 and abundances from Boberg et al. 2015, 2016; Simpson & Martell 2019). Massari et al. (2019) attribute NGC 5024, NGC 5053 to the Helmi Streams and ESO 280-SC06 to GSE. We note, however, that none of these GCs satisfy the Helmi Streams selection from Koppelman et al. (2019b) that we also use in this work (Equation (5)) and that ESO 280-

SC06 ($[\text{Fe}/\text{H}] = -2.5$, $e = 0.66$) has properties only marginally consistent with the GSE stars in the sample. That multiple GCs with metallicities consistent with Wukong are aligned with it in phase space is a promising sign that it is a genuine structure.¹³

3.2.9. Metal-weak Thick Disk

The metal-poor tail of the high- α disk was not included in our earlier selection of the high- α disk and in situ halo in chemical space (Figure 10). MWTD¹⁴ stars are expected to fall right next to the high- α disk in $[\text{Fe}/\text{H}]$ versus $[\alpha/\text{Fe}]$. They are more metal poor than the high- α disk but are at similar α and are rotationally supported—i.e., prograde and with strong J_ϕ (top-left panel of Figure 7). This motivates the MWTD selection:

$$\begin{aligned}
 & (-2.5 < [\text{Fe}/\text{H}] < -0.8) \wedge (0.25 < [\alpha/\text{Fe}] < 0.45) \\
 & \wedge (J_\phi/J_{\text{tot}} < -0.5) \\
 & \wedge (\text{excluding all previously defined structures}). \quad (9)
 \end{aligned}$$

The stars that satisfy these cuts are shown in Figure 16. They are mostly clustered very close to the high- α disk in $[\text{Fe}/\text{H}]$

¹³ As this paper was being reviewed, Yuan et al. (2020a) independently reported Wukong using SDSS+LAMOST RR Lyrae and BHs as a “low-mass stellar debris stream,” LMS-1, that they associated with NGC 5024 and NGC 5053.

¹⁴ Following previous work, we refer to this population as the MWTD. However, given our selection, it might be more appropriate to refer to this structure as the “metal-weak high- α disk.”

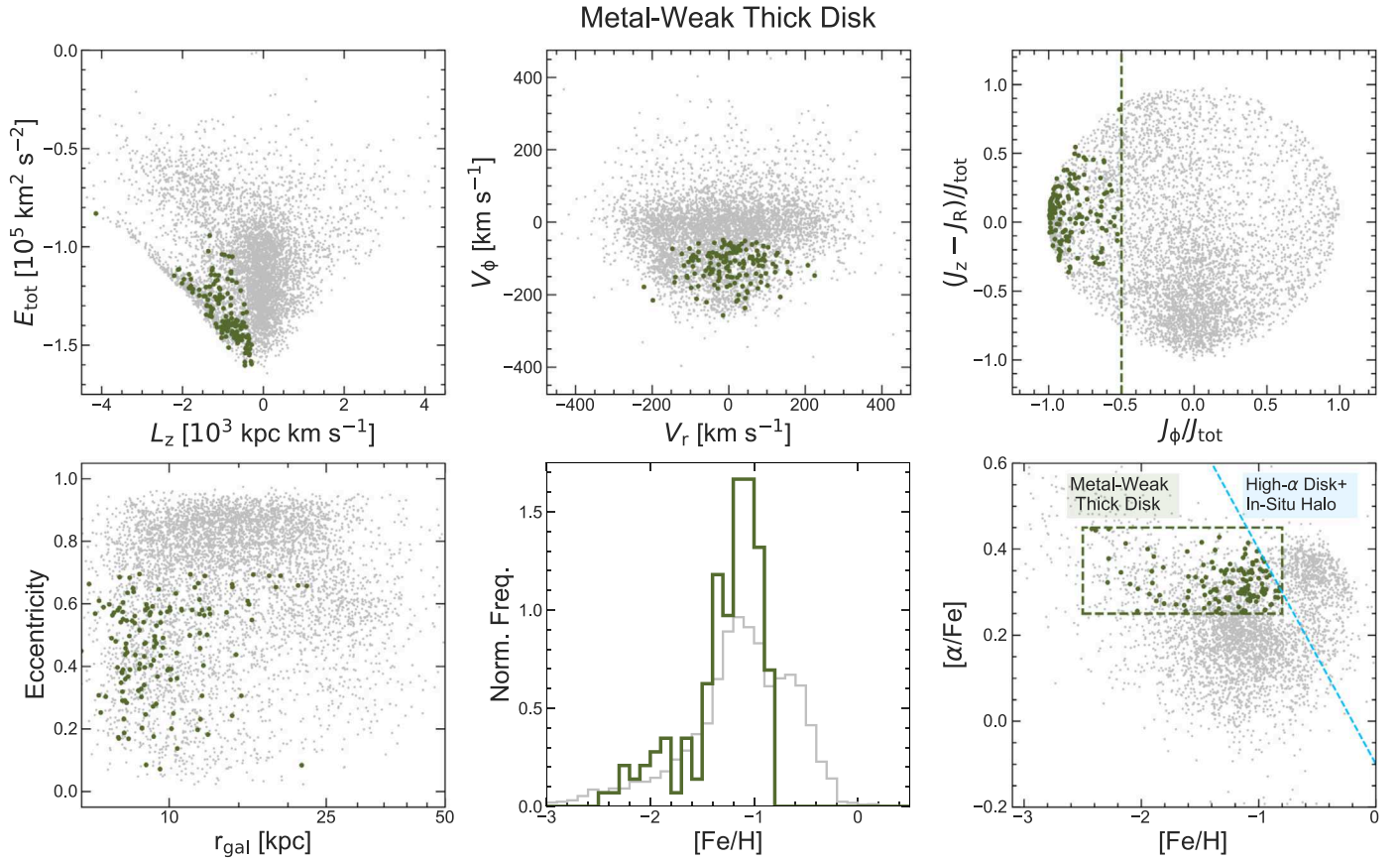


Figure 16. The metal-weak thick disk (MWTD, olive green) in chemodynamical space. Panels are as in Figure 11. MWTD stars are selected to be rotationally supported (top right) and to lie at similar $[\alpha/\text{Fe}]$ but lower $[\text{Fe}/\text{H}]$ than the high- α disk (bottom right) following Carollo et al. (2019). The resulting stars show a broad range of eccentricities and follow the locus of the high- α disk and in situ halo in $E-L_z$ and V_r-V_ϕ .

versus $[\alpha/\text{Fe}]$ at $[\text{Fe}/\text{H}] \approx -0.8$. These stars support the finding of Carollo et al. (2019) that while the MWTD may be a prominent component of the $|\text{Z}_{\text{gal}}| < 3$ kpc Galaxy, it is only a minor component at larger distances (weighted fraction of <5% at $|\text{Z}_{\text{gal}}| > 3$ kpc).

3.2.10. Unclassified Debris

We have assigned 92% (weighted) of our sample to the aforementioned structures. This leaves us with 8% (weighted) that we designate as “unclassified debris.” The unclassified debris is depicted in Figure 17.

A prograde population that closely follows the contours of the high- α disk/in situ halo in $E-L_z$ is evident at $E_{\text{tot}} < -1.3$, $|L_z| < 1$ (compare with Figure 10). There is also an overlapping population, extending to higher energies ($E_{\text{tot}} \approx -0.8$) with a high degree of rotational support ($J_\phi/J_{\text{tot}} < -0.75$). These disk-like stars did not meet the high- α disk/in situ halo and MWTD cuts. These stars are either (i) the eccentric, metal-poor tail of the high- α disk (or the low-eccentricity tail of GSE) that did not meet the rotational support criteria of the MWTD, or (ii) rotationally supported stars that fall outside our high- α disk and MWTD chemistry selection boxes. We designate these stars as “disk-like” unclassified debris, and they constitute 2% (weighted) of the total sample.

Then there are “halo-like” stars at higher energy clustered around various selection boxes. Most of these stars have eccentricities between 0.6 and 0.7 (5% of the total sample, weighted). This concentration in eccentricity is noteworthy

because we select GSE stars with a hard cut at $e > 0.7$. This, and the prominent peak in the MDF at GSE’s metallicity, strongly suggests these stars are $e < 0.7$ members of GSE. The clumps of unclassified debris stars that appear at the locations of Thamnos and Wukong in $E-L_z$ bear this out: these stars satisfied the phase-space selections for these structures, but had GSE-like metallicity and were excluded via cuts on the MDF (see dashed MDFs in Figures 13, 15). This aspect of our work may be improved with more probabilistic methods of assigning membership that do not impose discontinuous selection boxes as we have done here (e.g., Yuan et al. 2020b).

Some of the prograde, high-energy “halo-like” stars (<1% of the entire sample, weighted) are also clustered in a selection box corresponding to the Helmi Streams. These stars have similar L_z and energies but do not satisfy the L_\perp condition we imposed. These stars are plausible members of the Helmi Streams.

Taking into account these likely associations, we are left with $\approx 1\%$ (weighted) of the total sample as being either unclassified or unassociated. These stars may belong to low-mass structures that we sample too few stars from to detect coherent features. Or these stars may simply have bad stellar or orbital parameters. Either way, it is clear that we have identified the vast majority of structure in the halo as viewed by H3.

3.3. Summary of Structure

In this section we present a synopsis of the structures identified in this work.

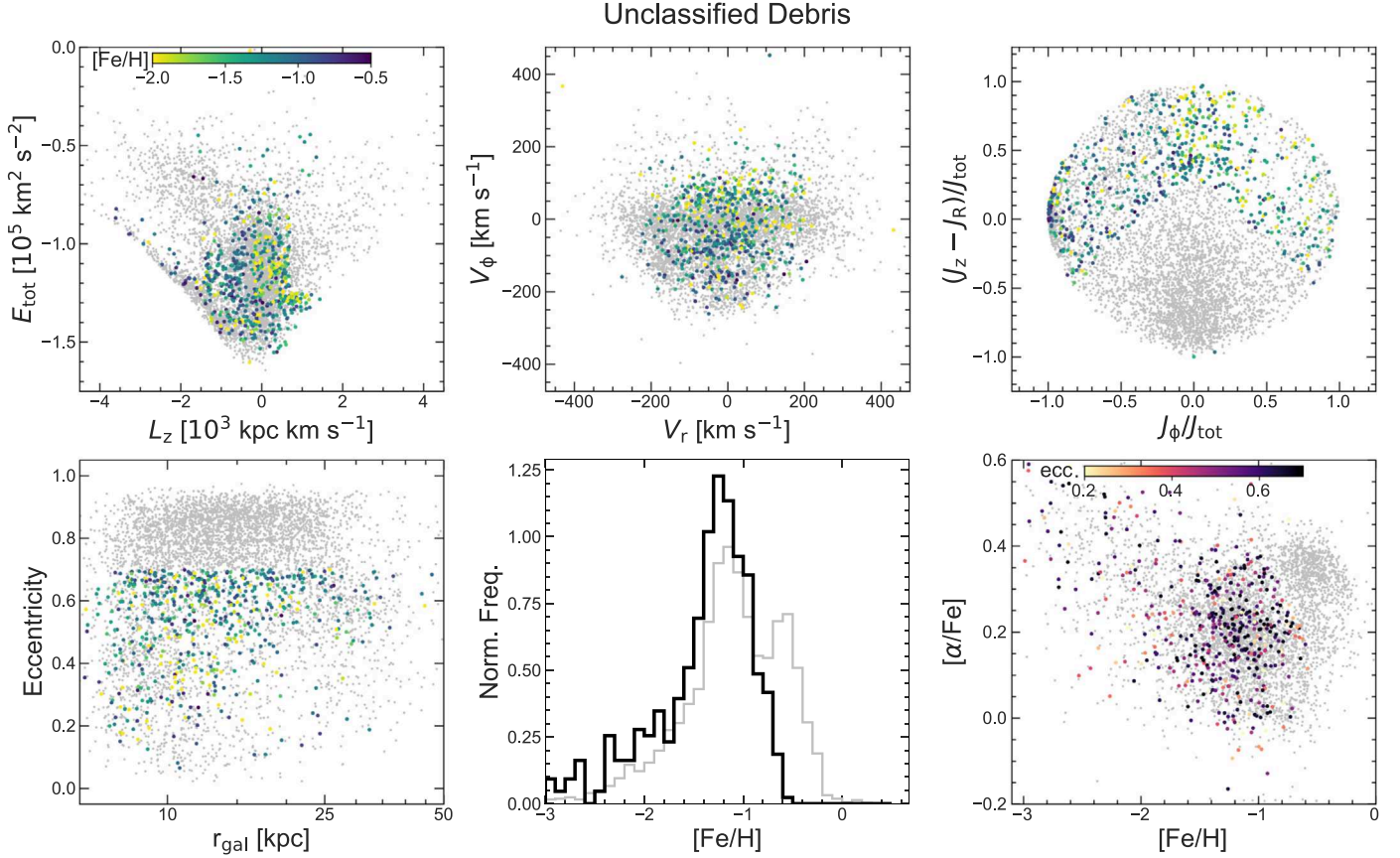


Figure 17. Unclassified debris in chemodynamical space. Panels are as in Figure 11. The projections of phase space are color-coded by $[Fe/H]$ except for the final panel, which is color-coded by eccentricity. $\approx 30\%$ of these stars have very negative J_ϕ/J_{tot} indicating some degree of rotational support. These stars are also clustered at $E < -1.3$ in $E-L_z$, following the contours of the high- α disk and in situ halo (see Figure 10). These disk-like stars are likely metal-poor members of the high- α disk and in situ halo that evaded our earlier selection of those populations. 70% of the remaining unclassified stars have eccentricities between 0.5 and 0.7. These high-eccentricity stars are similar to GSE (which was defined to have $e > 0.7$), Arjuna ($e \approx 0.6$), and Sequoia ($e \approx 0.6$) in $[Fe/H]$ vs. $[\alpha/Fe]$, and have an MDF similar to GSE (bottom center), which strongly suggests these are stars from these structures that were missed in our earlier selections. There are overdensities in $E-L_z$ at the locations of Thamnos and Wukong—these stars satisfy the phase-space selections for these structures but not the chemistry cuts and have MDFs resembling GSE, i.e., they may represent the lower eccentricity tail of GSE (see dashed MDFs in Figures 13, 15). There is also a set of stars at $L_z \approx -1.5$ in $E-L_z$ that closely follows the contours of the Helmi Streams (Figure 12) but did not satisfy the L_\perp selection.

1. *Gaia–Sausage–Enceladus* ($f = 0.42^{15}$): the radial, head-on merger that dominates the metal-poor local halo, GSE is largely contained within ≈ 30 kpc and displays a narrow MDF ($[Fe/H] = -1.15^{+0.24}_{-0.33}$, weighted) reminiscent of the local dwarfs Leo I and Fornax. Its metallicity and proposed accretion redshifts imply a stellar mass of $4\text{--}7 \times 10^8 M_\odot$. Its mean rotation is consistent with zero: $\langle V_\phi \rangle = 1.04^{+1.26}_{-1.25} \text{ km s}^{-1}$, $\langle L_z \rangle = 4.7^{+20.1}_{-10.5} \text{ kpc km s}^{-1}$. (Section 3.2.4, Figure 11).
2. *Sagittarius* ($f = 0.24$): one of the first known streams, Sgr displays a uniquely high $|L_y|$ that allows for a clean selection leveraging full 6D phase space. Its MDF is multipeaked with a pronounced metal-poor tail. (Section 3.2.1, Figure 8).
3. *High- α Disk and In Situ Halo* ($f = 0.15$): a major component of the local Galaxy, the high- α disk, and its high-eccentricity tail (the “in situ” halo) extend out to $|Z_{\text{gal}}| \approx 15$ kpc. Their eccentricity distribution is continuous, ranging from very circular to highly eccentric, supporting scenarios in which the primordial high- α disk

was disturbed by a merger event (likely GSE). (Section 3.2.3, Figure 10).

4. *Arjuna, Sequoia, I’itoi* ($f = 0.02, 0.01, 0.01$): the constituents of the high-energy retrograde halo—Arjuna ($[Fe/H] = -1.2$), Sequoia ($[Fe/H] = -1.6$), and I’itoi ($[Fe/H] < -2$)—are eccentric ($e \approx 0.5\text{--}0.6$) and extend to highly retrograde orbits ($L_z/[10^3 \text{ kpc km s}^{-1}] > 2$). Arjuna is the dominant component with $\gtrsim 2 \times$ the stars as Sequoia and may be a distinct accreted structure or a hitherto unknown, highly retrograde extension of GSE. (Section 3.2.7, Figure 14).
5. *Metal-weak thick disk* ($f = 0.02$): the metal-poor extension of the high- α disk is only a minor component of the $|Z| > 3$ kpc halo ($\lesssim 5\%$) as suggested by local studies. (Section 3.2.9, Figure 16)
6. *Aleph* ($f = 0.02$): a highly circular structure ($e = 0.13 \pm 0.06$) that rises ≈ 10 kpc off the plane. It is significantly enriched compared to typical halo structures ($[Fe/H] = -0.5$, $[\alpha/Fe] = 0.2$) and may be associated with the enigmatic globular cluster Palomar 1. Whether it is an in situ or ex situ structure is under investigation. (Section 3.2.2, Figure 9)
7. *Wukong* ($f = 0.01$): comprising the “prograde shards” of the halo, Wukong ($[Fe/H] = -1.7$) spans a wide range in

¹⁵ Fraction of stars assigned to the structure, weighted to account for the selection function.

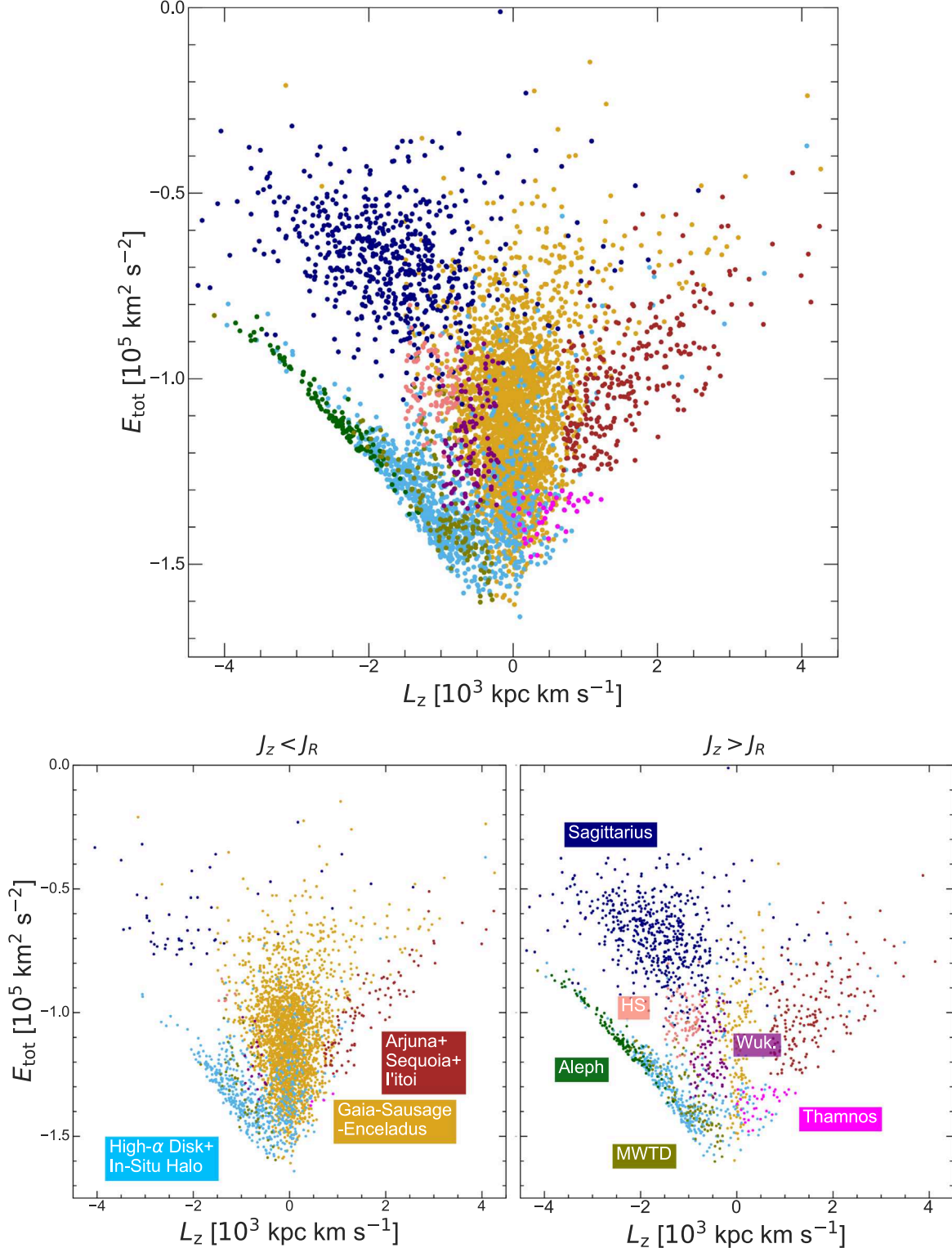


Figure 18. Top: E – L_z diagram depicting all the structures identified in this work. Bottom: E – L_z split by actions with stars on radial ($J_z < J_R$) orbits on the left and polar, circular ($J_z > J_R$) orbits on the right. We abbreviate the Helmi Streams as “HS” and Wukong as “Wuk.” to avoid crowding.

energy and eccentricity reminiscent of massive structures like Sequoia and the Helmi Streams and is likely associated with the metal-poor GCs NGC 5024, NGC 5053, and ESO 280-SC06. (Section 3.2.8, Figure 15).

8. *Helmi Streams* ($f = 0.01$): among the first halo structures discovered in integrals of motion, the Helmi Streams

show a complex chemical population consistent with an extended star formation history, have a stellar mass of $\approx 0.5\text{--}1 \times 10^8 M_\odot$, and rise ≈ 25 kpc off the plane, as expected from local samples. (Section 3.2.5, Figure 12)

9. *Thamnos* ($f = 0.01$): A recently discovered structure whose existence we confirm, Thamnos is among the most

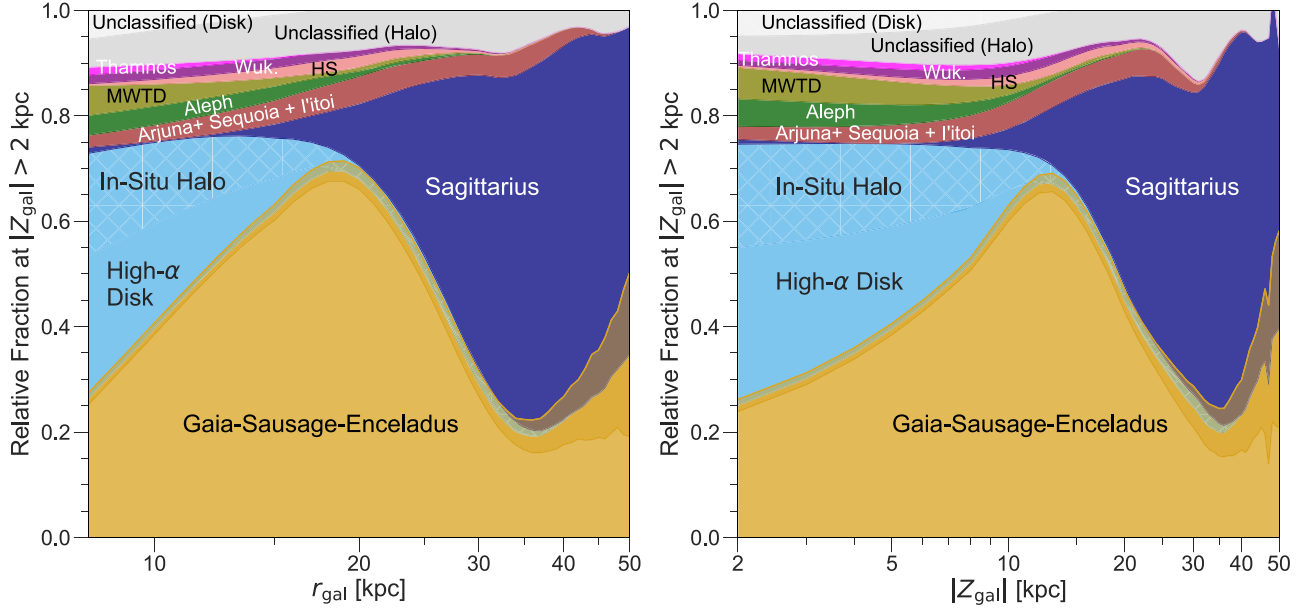


Figure 19. Relative fractions of structures as a function of total Galactocentric distance, r_{gal} (left) and distance from the plane, $|Z_{\text{gal}}|$ (right). Fractions have been corrected for the H3 Survey selection function. The high- α disk is defined to lie at $e < 0.5$ and the in situ halo at $e > 0.5$, though note these stars define a continuous distribution in eccentricity. Poisson error intervals are shown only for GSE to minimize crowding. GSE, the high- α disk and in situ halo, and Sgr together account for $\gtrsim 75\%$ of all stars at all distances. The high- α disk and in situ halo are prominent in the solar neighborhood and close to the plane, but their fraction rapidly declines to $< 5\%$ by $|Z_{\text{gal}}| \approx 10 \text{ kpc}$ ($r_{\text{gal}} \approx 15 \text{ kpc}$). GSE is the dominant component within $|Z_{\text{gal}}| \approx 10\text{--}20 \text{ kpc}$ ($r_{\text{gal}} \approx 15\text{--}25 \text{ kpc}$) while the majority of stars at larger distances belong to Sgr. None of the other components contribute more than $\approx 5\%$ at any distance. Note that the unclassified halo debris is mostly comprised of the low-eccentricity tail ($e < 0.7$) of GSE (Section 3.2.10).

metal-poor structures in the halo ($[\text{Fe}/\text{H}] = -1.9$, $[\alpha/\text{Fe}] = 0.3$). With a stellar mass that we estimate to be $\approx 2 \times 10^6 M_{\odot}$, it is remarkable that Thamnos lies so deep in the potential ($r_{\text{gal}} = 9 \text{ kpc}$), which makes it an exciting and accessible ($d_{\text{helio}} = 6 \text{ kpc}$) target for near-field cosmology. (Section 3.2.6, Figure 13).

We have assigned 92% (weighted) of our sample to these structures. Their properties are summarized in Table 1. In Figure 18, we depict the various structures we have identified in E – L_z , and in E – L_z split by actions. As we have shown in this section, these populations that are clumped in E – L_z not only occupy similar regions of phase space, but also often define distinct chemical populations. Almost the entire halo can be accounted for as the superposition of these populations.

Examining the remaining 8%, the “unclassified debris” (Section 3.2.10, Figure 17), 2% are “disk-like” and likely eccentric, metal-poor members of the high- α disk and in situ halo. The remaining 5% have higher energy “halo-like” orbits. A large fraction of these ($\approx 4\%$ of the sample) are plausible members of GSE and the Helmi Streams. Within the survey footprint, any remaining unidentified systems must comprise, in aggregate, no more than $\approx 1\%$ of the high-latitude Galaxy within 50 kpc.

4. Discussion

4.1. Relative Fractions of Substructure and the Mass Function of Accreted Structure

We are now in a position to examine which components of the halo are dominant at different distances. We depict the relative fractions of substructure, corrected for the selection function, as a function of Galactocentric distance and distance from the plane in Figure 19. Fractions are computed in running 5 kpc bins and smoothed with a Savitzky–Golay filter (10 kpc

window, second-order polynomial) for clarity. The unclassified debris are included as gray bands on the top—note that we argued in Section 3.2.10 that a majority of these stars can be reasonably attributed to GSE.

In agreement with local studies (e.g., Bonaca et al. 2017; Haywood et al. 2018; Di Matteo et al. 2019; Amarante et al. 2020; Belokurov et al. 2020), we find the high- α disk and its heated high-eccentricity tail (referred to as the “in situ halo” in this work and “Splash” in Belokurov et al. 2020) contribute the majority of stars at $|Z_{\text{gal}}| \approx 2 \text{ kpc}$. We separate the high- α disk from the in situ halo based on eccentricity ($e > 0.5$)—this is an arbitrary cut, because these populations define a continuous distribution in eccentricity (Figure 10). The eccentric in situ halo (blue hatched region) extends farther and rises to higher elevation than high- α disk. The high- α disk and in situ halo fraction falls rapidly from $\sim 50\%$ at $|Z_{\text{gal}}| = 2 \text{ kpc}$ to $< 5\%$ beyond $|Z_{\text{gal}}| = 15 \text{ kpc}$. At $|Z_{\text{gal}}| \approx 10 \text{ kpc}$, GSE takes over and composes $> 50\%$ of the stars, and at farther distances, between $|Z_{\text{gal}}| \approx 25\text{--}50 \text{ kpc}$, the majority of stars belong to Sagittarius. Similar trends are observed in the relative fractions as a function of r_{gal} as well. The span of GSE, largely contained within 35 kpc, is in excellent agreement with observational estimates of its spatial extent (e.g., Deason et al. 2018; Lancaster et al. 2019). Figure 19 shows an uptick in the GSE relative fraction past 35 kpc—this is mostly due to the fractions of all non-Sgr structures falling off and the large Poisson noise at these distances (depicted in Figure 19 as a golden envelope).

At all distances, the other structures comprise $< 25\%$ of the sample. Our fractional budget clearly confirms the prediction of various simulations that at $r_{\text{gal}} < 50 \text{ kpc}$ the accreted halo is built by a handful of massive ($M_{\text{star}} = 10^8\text{--}10^9 M_{\odot}$) progenitors (GSE and Sgr in the MW’s case) with a subdominant contribution from lower-mass galaxies and ultra-faints

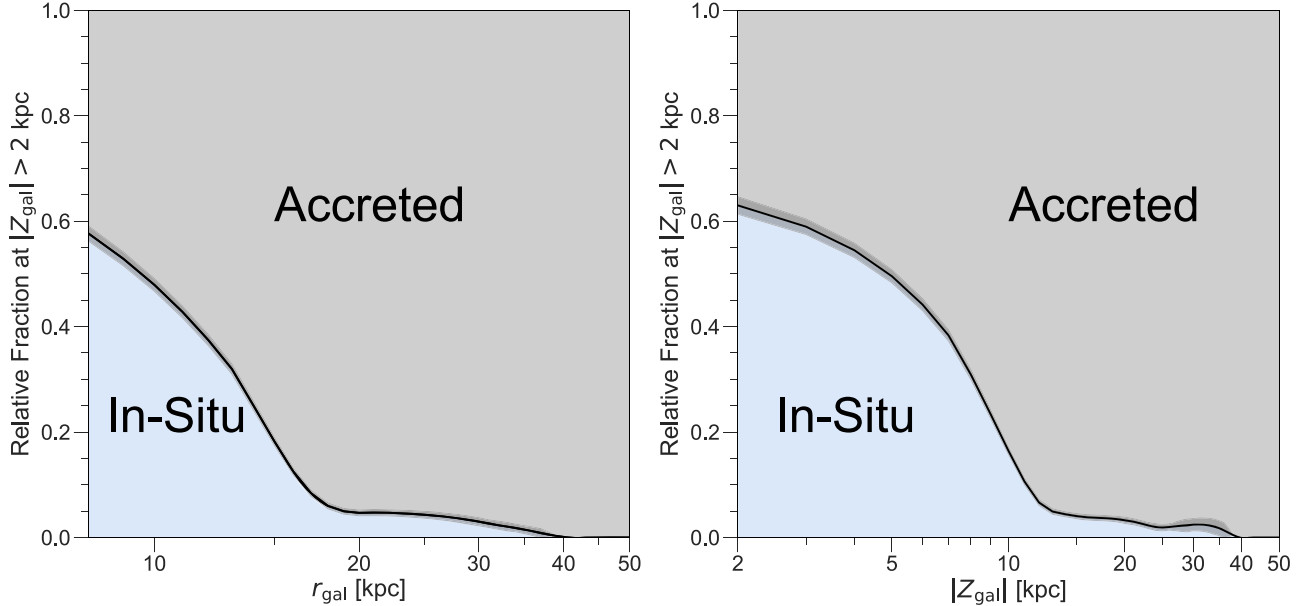


Figure 20. Relative fractions of accreted and in situ components as a function of total Galactocentric distance, r_{gal} (left) and distance from the plane, $|Z_{\text{gal}}|$ (right). The high- α disk and in situ halo, the metal-weak thick disk, Aleph, and unclassified disk debris are classed as “in situ” while the other components (including the unclassified halo debris) are classed as “accreted.” Poisson errors are shown as a gray envelope. The in situ components are largely confined within 20 kpc of the Galactic center and the Galactic plane. We caution that the in situ halo stars at $|Z| > 15$ kpc lie close to the selection boundary in Figure 10 and may belong to other structures, so the in situ relative fraction at these distances should be considered an upper limit. Simulations suggest that a high in situ fraction around the solar circle that rapidly tapers off within ~ 30 kpc suggests a quiescent recent accretion history and that the halo was largely built at early times (see Section 3.2.3).

($M_{\text{star}} < 10^5 M_{\odot}$) (e.g., Deason et al. 2016; Fattahi et al. 2020; Santistevan et al. 2020).

The three structures that together compose $\gtrsim 75\%$ of the sample at all distances (the high- α disk + in situ halo, GSE, Sgr) have particularly secure selections. Sgr, due to its recent accretion, is highly coherent in phase space; the high- α disk and in situ halo occupy a unique location in $[\text{Fe}/\text{H}]$ versus $[\alpha/\text{Fe}]$; and the GSE MDF shows one clear component that is well fit by a simple analytical model and is reminiscent of the narrow MDFs of local dwarfs like Fornax and Leo I (Kirby et al. 2013). The robustness of these selections inspires confidence in our conclusion that the mass function of accreted material is indeed “top heavy.” In fact, the dominance of these three components is even more pronounced ($>80\%$) if a large fraction of the “unclassified debris,” as we have argued in Section 3.2.10, is allocated to GSE.

4.2. The Origin of the Stellar Halo

As per our accounting of structures, the halo is built almost entirely by the accretion of dwarf galaxies (e.g., GSE, Sgr, Arjuna) and the response of the Galaxy to their accretion (e.g., the heating of the high- α disk). The in situ halo is an important component at $r_{\text{gal}} < 10$ kpc, but its relative fraction rapidly falls off at larger radii (Figure 19). This can also be seen in Figure 20, where we combine all the components that likely originated in the Galaxy (high- α disk and in situ halo, the metal-weak thick disk, Aleph, the unclassified disk debris) and compare their extent to the accreted components. As we detail in the remainder of this section, our inventory of structure leaves little room for other proposed in situ (e.g., a smooth “collapsed halo,” outflows that deposit stars in the halo) or ex situ components (e.g., dissolved globular clusters, an $[\text{Fe}/\text{H}] \sim -2.2$ spherical “outer halo”).

4.2.1. The In Situ Halo

The mass budget and origin of the in situ halo—not just the heated disk, but also stars forming from gas that is smoothly accreted, stripped from infalling galaxies, or ejected in outflows—are debated across simulations and may help constrain subgrid physics such as star formation and feedback prescriptions (e.g., Font et al. 2011, 2020; Cooper et al. 2015; Pillepich et al. 2018; Fattahi et al. 2020; Yu et al. 2020). The extent and relative fraction of the in situ halo (in particular, the heated disk) are also sensitive probes of the accretion history of the MW (e.g., Zolotov et al. 2009; Monachesi et al. 2019).

We find that other than the heated high- α disk, the $r_{\text{gal}} < 50$ kpc halo does not contain any other in situ populations (Figures 19, 20). Aleph, which may have been heated or kicked from the disk may be an exception, but more work needs to be done to ascertain its nature. In any case, the high- α disk + in situ halo and Aleph combined form a significant fraction of the halo only at $r_{\text{gal}} \lesssim 15$ kpc. We do not see a substantial fraction of eccentric stars with low- α or high- α disk-like chemistry in the distant halo (see hatched blue band in Figure 18) as might be expected if stars in outflows formed a significant component of the halo (e.g., Yu et al. 2020). Nor do we see a significant smoothly accreted component built out of cooling gas from the circumgalactic medium and cosmological inflows whose relative fraction is comparable to accreted material (e.g., Cooper et al. 2015). These stars would resemble a smooth, isotropic, relatively metal-poor halo from monolithic collapse and not show the cogent structure associated with chemical evolution in dwarf galaxies in $[\text{Fe}/\text{H}]$ versus $[\alpha/\text{Fe}]$. The final category of in situ halo stars, stars formed from stripped gas from a dwarf galaxy, would be very difficult to tell apart from the debris of the dwarf, as they are likely to be aligned in phase space as well as chemically—progress could be made with precise ages to isolate stars that formed after the

satellite’s infall, as has been done for Sgr (e.g., Siegel et al. 2007; de Boer et al. 2015; Alfaro-Cuello et al. 2019).

The in situ halo can also be used to constrain the MW’s merger history. Monachesi et al. (2019) found that galaxies in the Auriga simulation suite with high in situ fractions ($>50\%$) beyond their optical radii ($\gtrsim 30$ kpc) either underwent a recent violent merger or a very early (>8 Gyr ago) merger that ejected disk stars to large radii. Similarly Zolotov et al. (2009) noted that simulated galaxies with quiescent merger histories (most of the mass in their halos was in place at ~ 9 Gyr) have a higher fraction of in situ stars in their inner halo ($\sim 20\%–50\%$) that rapidly tapers off by ~ 30 kpc. This is very similar to what we find (Figure 20), suggesting the bulk of the halo was already in place at early times and that the MW’s recent growth has largely been quiescent (modulo Sgr, which is an important perturber of the disk, but due to its polar orbit, not a major contributor to the in situ halo). This is a completely complementary way of accessing the MW’s merger history and is in excellent agreement with the picture of a quiet merger history at later times inferred from GCs (Kruijssen et al. 2019, 2020), precise ages of the MW’s various components (Bonaca et al. 2020), and the presence of a prominent break in the density profile (Deason et al. 2013). This qualitative finding can be further refined through more detailed comparisons with simulations after accounting for the simple H3 selection function.

4.2.2. The Ex Situ Halo

The fact that the distant halo is clumpy and highly structured has long been interpreted as strong evidence for an accretion origin of the halo (e.g., Newberg et al. 2002; Bell et al. 2008; Starkenburg et al. 2009; Xue et al. 2011; Schlaufman et al. 2012). Here we confirm this picture and further refine this finding by quantifying the proportions of various in situ and ex situ components. As described in Section 4.1 and Figure 19, we find that the accreted component almost entirely arises from a handful of massive ($M_* \sim 10^8–10^9 M_\odot$) dwarfs. In the rest of this section, we examine two popular scenarios about the nature of the accreted component in the context of our findings (the “dual halo” and disrupting GCs).

Carollo et al. (2007, 2010) and Beers et al. (2012) used a local sample ($d_{\text{helio}} < 4$ kpc) and integrated orbits to infer that the halo was best described as a “dual halo” (but see Schönrich et al. 2011). In their picture, the dual halo comprises an inner in situ halo ($r_{\text{gal}} \lesssim 15$ kpc, $[\text{Fe}/\text{H}] = -1.6$, small net prograde motion, high eccentricity) and an outer accreted halo ($r_{\text{gal}} \sim 20–50$ kpc, $[\text{Fe}/\text{H}] = -2.2$, mean retrograde motion, wide range of eccentricities) that are two fundamentally different populations. With the benefit of a post-Gaia perspective, Helmi (2020) interpret the outer retrograde halo as GSE with a steep metallicity gradient and the inner halo as the heated high- α disk. This is partially motivated by the Gaia color-magnitude diagram in the local halo, which shows two prominent sequences that have been attributed to GSE and the heated high- α disk. Belokurov et al. (2020), on the other hand, argue the “inner halo” is in fact GSE.

Figures 18 and 20 help clarify this debate. The “inner halo” ($r_{\text{gal}} \lesssim 15$ kpc) is predominantly built by GSE and the heated high- α disk, with GSE contributing a larger relative fraction. This is exactly as expected from simulations that find the inner halo to be a mixture of heated disk stars and accreted material, with the proportion varying with details of the accretion history

of the galaxy (e.g., Zolotov et al. 2009; Tissera et al. 2014; Monachesi et al. 2019). As for the Carollo et al. (2010) “outer halo” ($r_{\text{gal}} \sim 20–50$ kpc), after setting Sagittarius aside, as it does not pass through the local halo, GSE is still a major component, but the retrograde Arjuna, Sequoia, and I’itoi contribute a significant fraction, too, and perhaps explain the finding of a net retrograde motion. We note, however, that considering only these structures at $r_{\text{gal}} \sim 20–50$ kpc produces only a mildly retrograde $\langle V_\phi \rangle = 12.5_{-6}^{+6}$ km s $^{-1}$ (weighted). Also, at no distance does a very metal-poor (e.g., $[\text{Fe}/\text{H}] < -2$) component comprise a significant fraction of the Galaxy. We conclude by noting that no single population—neither the in situ halo nor GSE—neatly maps onto either component of the dual halo, and more work needs to be done to understand the effects of extrapolating the nature of the distant Galaxy from energetic local halo orbits.

Several authors have hypothesized that stars born in GCs might contribute significantly to the stellar halo mass budget—with estimates ranging from $\lesssim 10\%$ to $\lesssim 50\%$ (e.g., Gnedin & Ostriker 1997; Martell et al. 2011, 2016; Schaefer & Charbonnel 2011; Carretta 2016; Schiavon et al. 2017; Fernández-Trincado et al. 2019; Koch et al. 2019). GCs are attractive candidates for building up at least some fraction of the halo because several of them are in the process of being tidally disrupted (e.g., Grillmair & Dionatos 2006; Myeong et al. 2017; Malhan et al. 2018; Shipp et al. 2018). Further, several popular scenarios for GC formation assume they underwent drastic mass loss at some point in their early history (see Bastian & Lardo 2018 for a recent review).

Post-Gaia DR2, almost all halo GCs (those at high energy that are not on disk-like orbits) have been associated with phase-space structures seen in stars, strongly suggesting they were accreted along with some dwarf Galaxy (Kruijssen et al. 2019, 2020; Massari et al. 2019; Myeong et al. 2019; Forbes 2020). This complicates the evaluation of the halo fraction arising from GCs, because in their phase-space coordinates, these accreted GCs resemble field stars from their parent dwarf galaxies.

However, there may still be a contribution from GCs associated with low-mass accreted dwarfs or ancient in situ GCs that may have dissolved in the MW halo in the distant past. We find that at least within 50 kpc, such GCs play a very limited role in building the halo. Being very conservative and allowing all the unclassified “halo-like” debris (Section 3.2.10) to emanate from GCs limit their contribution to $< 6\%$ (weighted) at all distances. This upper limit is in excellent agreement with high-resolution simulations (Reina-Campos et al. 2020) that find similarly low fractions (2%–5%), with recent searches for second-generation GC stars in the halo (Koch et al. 2019; Hanke et al. 2020) that find a low observed fraction of $2.6\% \pm 0.2\%$ that they adjust to $< 11\% \pm 1\%$ to account for first-generation stars, and arguments based on BHB to blue-straggler ratios that found the halo ratio resembled dwarf galaxies and not GCs (Deason et al. 2015).

4.3. Prograde versus Retrograde and the Net Rotation of the Halo

In local halo studies, there appears to be an asymmetry in the distribution of accreted stars, with more retrograde than prograde structure. For instance, Helmi et al. (2017) find 58%–73% of high-energy halo stars are retrograde (see also Myeong et al. 2018c, 2018d). More recently, Yuan et al. (2020b) recovered six

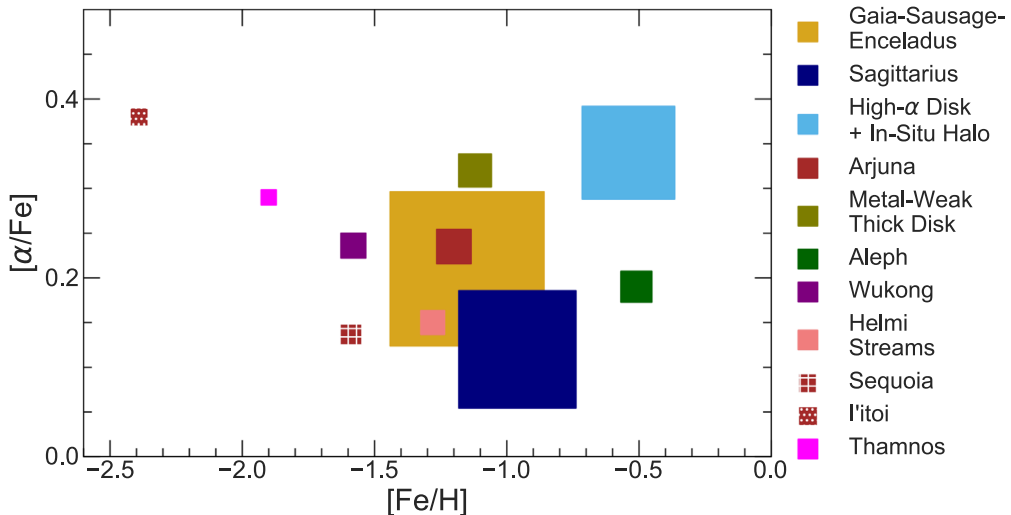


Figure 21. Median $[\alpha/\text{Fe}]$ vs. median $[\text{Fe}/\text{H}]$ for all structures identified in this work. The symbols are scaled linearly by the fractions in Table 1, and the legend is sorted by decreasing fraction. The three main components of the $|\text{Z}_{\text{gal}}| > 2$ Galaxy—GSE, Sgr, the high- α disk, and in situ halo—all lie at $[\text{Fe}/\text{H}] > -1.5$, producing a halo that is metal rich to at least 50 kpc. Sgr has the lowest $[\alpha/\text{Fe}]$ consistent with it being accreted relatively recently. On the other hand, I'itoi and Thamnos are highly α enhanced and were perhaps accreted quite early in the history of the Galaxy.

new retrograde “dynamically tagged groups” compared to two prograde groups in LAMOST DR3. These findings bear echoes of the Carollo et al. (2007, 2010) “dual halo,” whose “outer halo” is retrograde. This asymmetry may simply be a selection effect, because it is easier to avoid contamination from the disk and in situ halo on the retrograde side, and because some structures, such as Sgr, are not represented in the local halo. It might also be physical—some models predict that the disk is more efficient at mixing structure accreted on prograde orbits compared to retrograde orbits (e.g., Byrd et al. 1986; Quinn & Goodman 1986; Norris & Ryan 1989; D’Onghia et al. 2010).

We observe no significant asymmetry in the distant halo. Setting the disk populations and unclassified debris aside, we find three prograde (Sagittarius, Helmi Streams, Wukong) and four retrograde (Arjuna, Sequoia, I'itoi, Thamnos) accreted structures. GSE shows a net rotation consistent with zero ($\langle V_{\phi} \rangle = 1.04^{+1.26}_{-1.25} \text{ km s}^{-1}$). If Sequoia and Arjuna are indeed associated with GSE, the net rotation combining these two components is weakly retrograde ($\langle V_{\phi} \rangle = 9.4^{+1.7}_{-1.6} \text{ km s}^{-1}$). In terms of relative fractions, after setting the $\langle V_{\phi} \rangle \sim 0$ GSE aside, prograde stars outnumber retrograde stars $\approx 3:2$ (mostly due to Sgr, excluding it results in $\approx 1:1$). The net rotation of accreted material (also counting the halo-like unclassified debris) is $\langle V_{\phi} \rangle = -25.23^{+2.54}_{-2.71} \text{ km s}^{-1}$ with Sgr, and $\langle V_{\phi} \rangle = 5.7^{+1.7}_{-1.6} \text{ km s}^{-1}$ when Sgr is excluded. All numbers quoted here have been weighted to correct for the selection function. Assuming an isotropic distribution of infalling satellites, the numbers in this section suggest that the prograde satellites are not more efficiently disrupted than retrograde satellites and that there is no strong mean rotation signal.

4.4. Interpreting the Halo in Chemical Space

The locations of various structures in $[\text{Fe}/\text{H}]$ versus $[\alpha/\text{Fe}]$, as listed in Table 1, are depicted in Figure 21. The markers representing the structures are sized linearly as per their weighted relative fractions. The markers are all square and not intended to reproduce the spread in abundances—because we make hard cuts on the MDF to select some structures, we are not well positioned to make fair estimates of the spread.

Broadly, in the $[\text{Fe}/\text{H}]$ – $[\alpha/\text{Fe}]$ plane, galaxies are expected to start off in the top left ($[\alpha/\text{Fe}]$ rich and $[\text{Fe}/\text{H}]$ poor) and end up toward the bottom right ($[\alpha/\text{Fe}]$ poor and $[\text{Fe}/\text{H}]$ rich) as they evolve and Type Ia supernovae take over from Type II supernovae as the chief pollutants of the ISM (e.g., Tinsley 1980; Matteucci & Gregg 1986; Maiolino & Mannucci 2019). This journey is interrupted when a galaxy is accreted and shredded by the MW, and to first order, its abundances are frozen in place.

We highlight some features of this space, while noting that detailed modeling (e.g., Fernández-Alvar et al. 2018; Vincenzo et al. 2019; Lian et al. 2020) is required to deduce finer details. Thamnos and I'itoi are the most α -rich and metal-poor structures. Based on its depth in the potential, we argued Thamnos was accreted at high redshift ($z \approx 1.5$), i.e., early in its chemical evolution. This may be the case for I'itoi as well, though it occurs at higher energy, which may mean it was accreted relatively recently but is simply very low-mass and formed stars inefficiently. At the other extreme of the plot, Sagittarius is the most α poor and metal rich of all the structures in the halo, likely because it was accreted very recently ($z < 1$, e.g., Laporte et al. 2018; Kruijssen et al. 2020; Ruiz-Lara et al. 2020), after undergoing significant enrichment by Type Ia supernovae. GSE, with mass comparable to Sagittarius, is relatively α enhanced and metal poor, which fits with the recent finding that it began interacting with the MW at $z \approx 2$ (Bonaca et al. 2020), when we expect its chemical evolution to have been interrupted. The Helmi Streams, accreted at $z \sim 0.5$ –1 (Koppelman et al. 2019b), i.e., at a similar epoch as Sgr, have $[\alpha/\text{Fe}]$ similar to Sgr, but are about 0.3 dex more metal poor, exactly as expected for a structure $\sim 10 \times$ less massive (Lee et al. 2015, their Figure 2). Wukong, Sequoia, and Arjuna are at intermediate locations between the two extremes of I'itoi and Sagittarius, and finer estimates of their masses and accretion redshifts are required to further interpret their $[\text{Fe}/\text{H}]$ versus $[\alpha/\text{Fe}]$ locations.

This figure is another way to see that the halo, at least out to 50 kpc, as seen in our sample, is relatively metal rich compared to several earlier studies (e.g., Carollo et al. 2007, 2010; Xue et al. 2015; Das & Binney 2016; Liu et al. 2018). The three

main components—GSE, Sgr, the high- α disk, and in situ halo (those with the largest marker sizes in Figure 21)—all lie almost entirely at $[\text{Fe}/\text{H}] > -1.5$. Only a small fraction of material can be attributed to the debris of metal-poor structures like I’itoi and Thamnos ($[\text{Fe}/\text{H}] \lesssim -2$). Even setting our definitions of various structures aside, we compute $\langle [\text{Fe}/\text{H}] \rangle = -1.18^{+0.01}_{-0.01}$ (weighted) for all the accreted material taken together—i.e., Sgr, GSE, Arjuna, Helmi Streams, Sequoia, Wukong, I’itoi, Thamnos, and the unclassified halo-like debris (see also Conroy et al. 2019b).

4.5. Caveats and Limitations

Our census of the stellar halo is incomplete owing to the H3 Survey field locations, which are currently restricted to $|b| > 40^\circ$ and $\text{decl.} > -20^\circ$ (see Figure 1). An accreted structure completely confined to in-plane orbits or the bulge, e.g., the “*ex situ disk*” (Gómez et al. 2017) and “Kraken”/“Koala” (Kruijssen et al. 2019, 2020; Forbes 2020), would be missed. Furthermore, we systematically undercount stars from structures on orbits that spend most of their time close to the plane or in the Southern Hemisphere. Finally, recently accreted structures that have a strong on-sky coherence may be missed or biased in our existing fields. Assessing and correcting these biases will be the subject of future work.

The number of halo stars in our current sample sets an effective limit on the lowest stellar mass system we could plausibly detect. We can estimate the mass completeness as follows: if the halo has $\sim 10^9$ stars (e.g., Deason et al. 2019; Mackereth & Bovy 2020) and we are tracing it with 5684 stars, for every structure with $\sim 175,000$ stars, we find 1 star in the survey (assuming all structures are isotropic and completely mixed—in detail, we observe more stars from nearby structures). That is, from a $10^6 M_\odot$ accreted galaxy, we expect ~ 10 stars in the sample. The detectability of such a structure would depend strongly on its location in phase space/chemistry, e.g., the $\sim 10^6 M_\odot$ Thamnos stands out due to it being very metal poor/ α rich in a region of phase space that is populated by metal-rich GSE stars. Even if we are currently unable to identify some low-mass structures as distinct components of the halo, it is clear that taken together, they play only a subdominant role in the overall mass budget (Figures 19, 21, Section 4.1).

Another limitation of this work is our decision to apply hard cuts to select various structures. Due to this choice we miss the tails of various distributions. This is particularly evident for GSE, whose low-eccentricity ($e < 0.7$) tail appears as a contaminant in, e.g., the initial phase-space selections for Thamnos and Wukong (see dashed histogram in the MDF panels of Figures 13, 15). These GSE stars end up classed as “unclassified halo debris.” On the other hand, because we attribute all $e > 0.7$ stars to GSE (after excluding the in situ halo and Sgr), we miss the high-eccentricity tails of all the structures that follow it in our inventory. These stars are likely a very insignificant fraction of the GSE sample, as our GSE MDF is smooth, well behaved, and modeled well as a single population. However, what is a small fraction for GSE might be a significant fraction of the other low-mass structures. And so, the structure identification in this work should be considered preliminary and requires further investigation. This aspect of our work may be improved with probabilistic

methods (discussed in Section 3.2), but for now we list it as a caveat.

Our adopted Galactic potential (Section 2.2), in keeping with the bulk of the halo substructure literature (e.g., Helmi et al. 2018; Koppelman et al. 2019b; Myeong et al. 2019; Helmi 2020; Koppelman & Helmi 2020; Yuan et al. 2020b), does not include a bar. This is a caveat to consider, because the bar, due to its time-dependent potential, may launch halo stars that pass through the bar region, particularly those in resonance with the bar, on chaotic orbits (e.g., Price-Whelan et al. 2016a, 2016b; Pearson et al. 2017; Mestre et al. 2020). However, some simulations suggest only a negligible effect on halo substructure as the chaotic behavior kicks in on timescales larger than the Hubble time (e.g., Maffione et al. 2015, 2018). The bar likely causes some stars, particularly those on radial orbits passing close to the Galactic center (e.g., from GSE, the in situ halo) and in resonance with the bar, to be categorized as unclassified disk/halo material (Section 3.2.10) and also dilutes the coherence of substructure in integrals of motion. As the parameters of the bar (mass, pattern speed, extent) become clearer (Bovy et al. 2019; Kipper et al. 2020; Queiroz et al. 2020), detailed simulations that extend work on its effect on cold, GC stellar streams to debris from massive dwarf galaxies, especially in terms of integrals of motion, would inform how best to incorporate the bar in analyses of halo substructure.

Finally, we caution that individual structures identified in this work may not necessarily correspond to unique, accreted dwarf galaxies. It is possible that, e.g., Wukong comprises multiple subpopulations corresponding to the modes in its MDF, or that GSE and Arjuna are linked. Simulations show that the same accreted structure can deposit stars in surprisingly disparate regions of phase space (e.g., Jean-Baptiste et al. 2017; Elias et al. 2020; Lilleengen et al. 2020), though this is typically not the case (e.g., Bullock & Johnston 2005; Font et al. 2006; Pfeffer et al. 2020). Further analysis of these individual structures is necessary in order to link them to unique accreted systems.

5. Summary

We have used the H3 Survey in combination with Gaia data to conduct a detailed census of substructure beyond the solar neighborhood. Our sample extends to 50 kpc, is unbiased in metallicity, arises from a simple selection function, and has full 6D phase-space coordinates along with $[\text{Fe}/\text{H}]$ and $[\alpha/\text{Fe}]$. We find the following:

1. The distant Galaxy displays a high degree of structure in integrals of motion (energy, actions, angular momenta) and chemistry ($[\text{Fe}/\text{H}]$, $[\alpha/\text{Fe}]$)—spaces in which coeval stars are expected to cluster for timescales longer than the age of the universe. [Figures 5, 6, 7].
2. Of our sample, 92% can be assigned to one of the following structures: Sagittarius, Aleph, the high- α disk + in situ halo (the heated high- α disk), the Helmi Streams, Thamnos, Arjuna, Sequoia, I’itoi, Wukong, Gaia–Sausage–Enceladus, and the metal-weak thick disk. Our key findings on each structure are distilled in Section 3.3. This leaves us with 8% of the sample (“unclassified debris,” 2% disk like and 6% halo like) that can be largely accounted for as artifacts of our sharp selection boundaries. (Section 3.3, Table 1).

3. The high- α disk, the in situ halo, GSE, and Sgr account for $\gtrsim 75\%$ of all stars at all distances. The high- α disk and in situ halo are a major component at $\lesssim 10$ kpc ($\approx 50\%$), but their relative fraction rapidly declines to $\lesssim 10\%$ beyond 15 kpc. GSE dominates between ≈ 15 –25 kpc and Sgr forms the bulk of the halo beyond 30 kpc. The accreted halo within 50 kpc is therefore mainly built out of a small number of 10^8 – $10^9 M_\odot$ galaxies (GSE, Sgr). That is, the mass function of accreted material is “top heavy.” This explains the metallicity of the halo ($[\text{Fe}/\text{H}] \approx -1.2$; see also Conroy et al. 2019b) that we find to be more metal rich than several previous studies. (Section 4.1, Figures 19, 20, 21).
4. This inventory of substructure leaves very limited room for other proposed constituents of the halo, including a spherical, retrograde, $[\text{Fe}/\text{H}] \sim -2.2$ “dual halo” beyond 25 kpc, dissolved globular clusters, stars deposited by outflows, or stars born from smoothly accreted gas. (Section 4.2, Figure 19).
5. There is no preference for retrograde orbits in the distant Galaxy as has been observed in the local halo. GSE shows a net rotation consistent with zero ($V_\phi = 1.0 \pm 1.3 \text{ km s}^{-1}$). In fact, setting the disk populations aside, prograde stars outnumber retrograde stars $\approx 3: 2$. (Section 4.3, Table 1).

It has long been recognized that the distant halo is highly structured and that this likely indicates an accretion origin. Here, we have confirmed this picture and further refined it by quantifying the exact proportions and extents of various in situ and ex situ components. In forthcoming work, we will present detailed characterizations of the identified structures. With future Gaia data releases, we will extend this work even farther into the halo using the ~ 1000 H3 giants extending out to 100 kpc that were excluded from this work due to uncertain proper motions. By resolving the stellar halo into its constituent pieces, we are delivering on the promise of Galactic Archaeology as a powerful tool to determine the assembly history of our Galaxy.

We thank the anonymous referee for a timely report that improved the clarity of this work. It is a pleasure to acknowledge illuminating conversations with Marion Dierickx, Diederik Kruijssen, GyuChul Myeong, Kareem El-Badry, Helmer Koppelman, Peter Senchyna, and Vasily Belokurov. R.P.N. gratefully acknowledges an Ashford Fellowship and Peirce Fellowship granted by Harvard University. C.C. acknowledges funding from the Packard foundation. Y.S.T. is supported by the NASA Hubble Fellowship grant HST-HF2-51425.001 awarded by the Space Telescope Science Institute. We thank the Hectochelle operators Chun Ly, ShiAnne Kattner, Perry Berlind, and Mike Calkins, and the CfA and U. Arizona TACs for their continued support of the H3 Survey. This paper uses data products produced by the OIR Telescope Data Center, supported by the Smithsonian Astrophysical Observatory. The computations in this paper were run on the

FASRC Cannon cluster supported by the FAS Division of Science Research Computing Group at Harvard University.

This work has made use of data from the European Space Agency (ESA) mission Gaia (<https://www.cosmos.esa.int/gaia>), processed by the Gaia Data Processing and Analysis Consortium (DPAC, <https://www.cosmos.esa.int/web/gaia/dpac/consortium>) (Gaia Collaboration et al. 2016, 2018). Funding for the DPAC has been provided by national institutions, in particular the institutions participating in the Gaia Multilateral Agreement.

Facilities: MMT (Hectochelle), Gaia.

Software: IPython (Pérez & Granger 2007), matplotlib (Hunter 2007), numpy (Oliphant 2006), scipy (Virtanen et al. 2020), jupyter (Kluyver et al. 2016), dynesty (Speagle 2019), gala (Price-Whelan 2017; Price-Whelan et al. 2017), GalPot (Dehnen & Binney 1998; McMillan 2017), Astropy (Astropy Collaboration et al. 2013, 2018).

Appendix A

Error Propagation in Phase Space

Here we explore how measurement errors—the $\lesssim 10\%$ distance uncertainty and the error on Gaia PMs—distort substructure in phase space. We use stellar halos built through hierarchical accretion from the Bullock & Johnston (2005), Robertson et al. (2005), and Font et al. (2006) simulations. These halos feature a realistic, evolving potential, including a disk component. Using the default settings of Galaxia, a code to generate synthetic surveys of the MW from analytical and N -body models (Sharma et al. 2011), we generate an H3-like survey—with a 10% error on distances, and errors on PMs as per the Gaia DR2 error model. Potential-dependent phase-space quantities are computed using the $z = 0$ potential described in Bullock & Johnston (2005).

Figure A1 shows E – L_z diagrams for three halos, both for the noiseless mock catalogs (top panels) and noisy mocks (center and bottom panels). We also highlight GSE-like, Sgr-like, and high-energy retrograde halo-like progenitors. While GSE-like and Sagittarius-like progenitors, which have comparatively lower L_z , retain their general morphology, the strongly retrograde progenitors are significantly smeared out along diagonal tracks in E – L_z . This is likely why we find it difficult to differentiate between Arjuna, Sequoia, and I’itoi in phase space even though they are chemically distinct. The GSE-like progenitors in Halo17 and Halo14 have halo masses of $\sim 10^{11} M_\odot$, were accreted at $z \sim 2$, are largely comprised of eccentric orbits ($> 70\%$ at $e > 0.7$), and have a spread in $|L_z|$ of $\sim 800 \text{ kpc km s}^{-1}$ and $\sim 1300 \text{ kpc km s}^{-1}$ (84th – 16th percentile), respectively while that of GSE is $\sim 500 \text{ kpc km s}^{-1}$. By comparing the center panels (noisy PMs and noisy distances) and bottom panels (perfect PMs and noisy distances), we see the distance errors are the most significant component of the error budget.

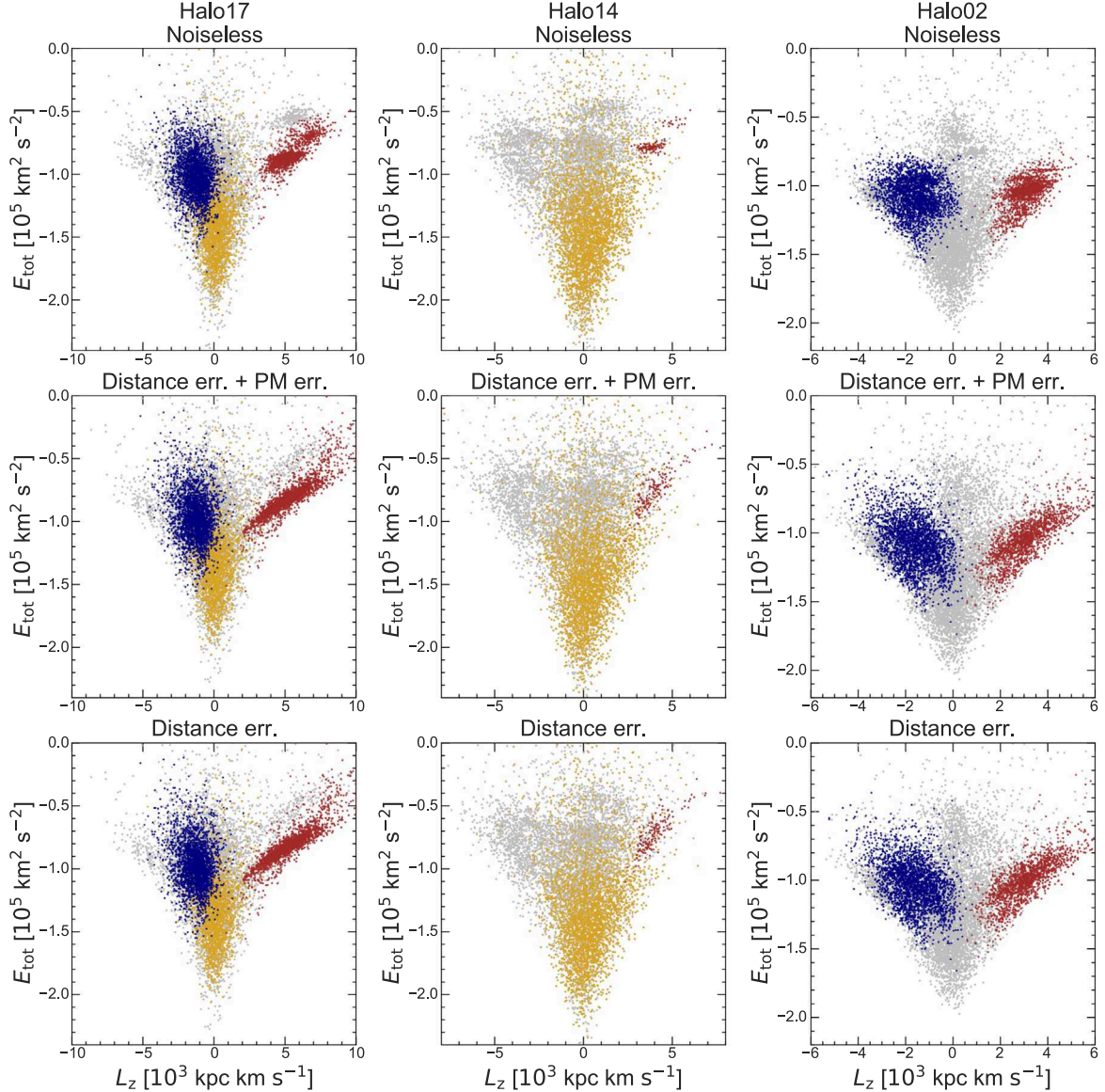


Figure A1. Comparison of mocks from three different halos in the Bullock & Johnston (2005) suite with no errors (top), with distance and PM errors (center), and with only distance errors (bottom). Sgr-like (navy blue), high-energy retrograde halo-like (brown), and GSE-like (golden) progenitors are highlighted here. While the Sgr-like and GSE-like locii retain their morphology to first order across all three rows, the retrograde progenitors with high L_z are dispersed dramatically along a diagonal track in $E-L_z$. This is likely why disambiguating the various components of the high-energy retrograde halo (Arjuna+Sequoia+I'itoi) purely in phase space without relying on chemistry is challenging. The center and bottom panels are virtually indistinguishable, emphasizing that the 10% distance error is the dominant piece of the error budget.

Appendix B Comparison with Alternate Potential

Here we provide a comparison against the McMillan (2017) potential which is widely employed in the halo literature (e.g., Koppelman et al. 2019a; Myeong et al. 2019) and features a more massive MW than in the adopted fiducial potential ($1.3 \times 10^{12} M_\odot$ versus $9.9 \times 10^{11} M_\odot$ within 200 kpc), with several differences in how the potential

is parameterized (thick and thin disks, gas disks, a different form for the bulge). Figure B1 allows for a straightforward visual conversion between the locations of various substructures across these two potentials. L_z is independent of the potential and thus is the same in the left and right panels. It is encouraging that the structures identified in our fiducial potential remain coherent and well defined in the alternative potential.

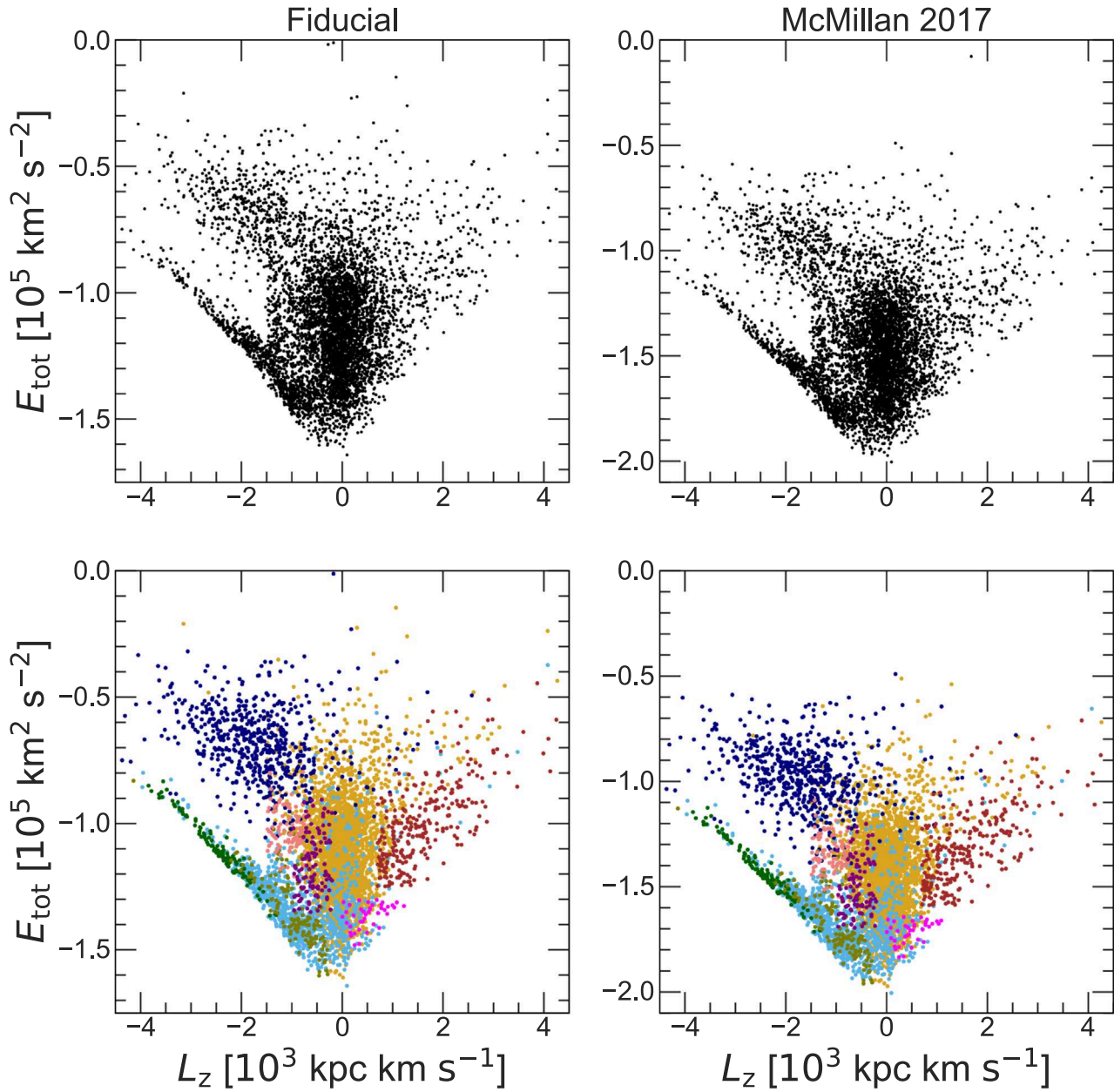


Figure B1. $E-L_z$ diagrams in the fiducial potential (left) compared against the McMillan (2017) potential (right). In the top row, we show the data as is and in the bottom row colored as per the substructure to which we have assigned these stars (same as Figure 18). $E-L_z$ appears clumpier in the McMillan (2017) potential due to the larger virial mass (e.g., Sanderson et al. 2015). Importantly, all the proposed structures (e.g., Wukong, Thamnos, the retrograde shards) correspond to clear clumps and overdensities in this potential.

ORCID iDs

Rohan P. Naidu  <https://orcid.org/0000-0003-3997-5705>
 Charlie Conroy  <https://orcid.org/0000-0002-1590-8551>
 Ana Bonaca  <https://orcid.org/0000-0002-7846-9787>
 Benjamin D. Johnson  <https://orcid.org/0000-0002-9280-7594>
 Yuan-Sen Ting (丁源森)  <https://orcid.org/0000-0001-5082-9536>
 Nelson Caldwell  <https://orcid.org/0000-0003-2352-3202>
 Dennis Zaritsky  <https://orcid.org/0000-0002-5177-727X>
 Phillip A. Cargile  <https://orcid.org/0000-0002-1617-8917>

References

Adibekyan, V. Z., Sousa, S. G., Santos, N. C., et al. 2012, *A&A*, **545**, A32
 Alfaro-Cuello, M., Kacharov, N., Neumayer, N., et al. 2019, *ApJ*, **886**, 57
 Amarante, J. A. S., Smith, M. C., & Boeche, C. 2020, *MNRAS*, **492**, 3816
 Amorisco, N. C. 2017, *MNRAS*, **464**, 2882
 Astropy Collaboration, Price-Whelan, A. M., Sipőcz, B. M., et al. 2018, *AJ*, **156**, 123
 Astropy Collaboration, Robitaille, T. P., Tollerud, E. J., et al. 2013, *A&A*, **558**, A33
 Barkana, R., & Loeb, A. 1999, *ApJ*, **523**, 54
 Bastian, N., & Lardo, C. 2018, *ARA&A*, **56**, 83
 Baumgardt, H., Hilker, M., Sollima, A., & Bellini, A. 2019, *MNRAS*, **482**, 5138

Beane, A., Sanderson, R. E., Ness, M. K., et al. 2019, *ApJ*, **883**, 103

Beers, T. C., Carollo, D., Ivezić, Ž, et al. 2012, *ApJ*, **746**, 34

Bell, E. F., Zucker, D. B., Belokurov, V., et al. 2008, *ApJ*, **680**, 295

Bellazzini, M., Newberg, H. J., Correnti, M., Ferraro, F. R., & Monaco, L. 2006, *A&A*, **457**, L21

Belokurov, V., Erkal, D., Evans, N. W., Koposov, S. E., & Deason, A. J. 2018, *MNRAS*, **478**, 611

Belokurov, V., Koposov, S. E., Evans, N. W., et al. 2014, *MNRAS*, **437**, 116

Belokurov, V., Sanders, J. L., Fattahi, A., et al. 2020, *MNRAS*, **494**, 3880

Bennett, M., & Bovy, J. 2019, *MNRAS*, **482**, 1417

Bensby, T., Feltzing, S., & Lundström, I. 2003, *A&A*, **410**, 527

Bergemann, M., Sesar, B., Cohen, J. G., et al. 2018, *Natur*, **555**, 334

Bian, F., Kewley, L. J., Groves, B., & Dopita, M. A. 2020, *MNRAS*, **493**, 580

Bignone, L. A., Helmi, A., & Tissera, P. B. 2019, *ApJL*, **883**, L5

Binney, J., & Tremaine, S. 2008, *Galactic Dynamics*: Second Edition (Princeton, NJ: Princeton Univ. Press)

Boberg, O. M., Friel, E. D., & Vesperini, E. 2015, *ApJ*, **804**, 109

Boberg, O. M., Friel, E. D., & Vesperini, E. 2016, *ApJ*, **824**, 5

Bonaca, A., Conroy, C., Cargile, P. A., et al. 2020, *ApJL*, **897**, L18

Bonaca, A., Conroy, C., Wetzel, A., Hopkins, P. F., & Kereš, D. 2017, *ApJ*, **845**, 101

Bovy, J. 2015, *ApJS*, **216**, 29

Bovy, J., Leung, H. W., Hunt, J. A. S., et al. 2019, *MNRAS*, **490**, 4740

Bovy, J., Nidever, D. L., Rix, H.-W., et al. 2014, *ApJ*, **790**, 127

Boylan-Kolchin, M., Weisz, D. R., Bullock, J. S., & Cooper, M. C. 2016, *MNRAS*, **462**, L51

Boylan-Kolchin, M., Weisz, D. R., Johnson, B. D., et al. 2015, *MNRAS*, **453**, 1503

Brown, A. G. A., Velázquez, H. M., & Aguilar, L. A. 2005, *MNRAS*, **359**, 1287

Bullock, J. S., & Johnston, K. V. 2005, *ApJ*, **635**, 931

Byrd, G. G., Saarinen, S., & Valtonen, M. J. 1986, *MNRAS*, **220**, 619

Caplar, N., & Tacchella, S. 2019, *MNRAS*, **487**, 3845

Cargile, P. A., Conroy, C., Johnson, B. D., et al. 2020, *ApJ*, **900**, 28

Carlin, J. L., Majewski, S. R., Casetti-Dinescu, D. I., et al. 2012, *ApJ*, **744**, 25

Carollo, D., Beers, T. C., Chiba, M., et al. 2010, *ApJ*, **712**, 692

Carollo, D., Beers, T. C., Lee, Y. S., et al. 2007, *Natur*, **450**, 1020

Carollo, D., Chiba, M., Ishigaki, M., et al. 2019, *ApJ*, **887**, 22

Carraro, G., Zinn, R., & Moni Bidin, C. 2007, *A&A*, **466**, 181

Carretta, E. 2016, in IAU Symp. 317, The General Assembly of Galaxy Halos: Structure, Origin and Evolution, ed. A. Bragaglia et al. (Cambridge: Cambridge Univ. Press), 97

Chambers, K. C., Magnier, E. A., Metcalfe, N., et al. 2016, arXiv:1612.05560

Chen, Y. Q., Nissen, P. E., Zhao, G., Zhang, H. W., & Benoni, T. 2000, *A&AS*, **141**, 491

Chiba, M., & Beers, T. C. 2000, *AJ*, **119**, 2843

Choi, J., Dotter, A., Conroy, C., et al. 2016, *ApJ*, **823**, 102

Chou, M.-Y., Majewski, S. R., Cunha, K., et al. 2007, *ApJ*, **670**, 346

Cohen, J. G., Sesar, B., Bahnlözer, S., et al. 2017, *ApJ*, **849**, 150

Conroy, C., Bonaca, A., Cargile, P., et al. 2019a, *ApJ*, **883**, 107

Conroy, C., Bonaca, A., Naidu, R. P., et al. 2018, *ApJL*, **861**, L16

Conroy, C., Naidu, R. P., Zaritsky, D., et al. 2019b, *ApJ*, **887**, 237

Cooper, A. P., Parry, O. H., Lowing, B., Cole, S., & Frenk, C. 2015, *MNRAS*, **454**, 3185

Cui, X.-Q., Zhao, Y.-H., Chu, Y.-Q., et al. 2012, *RAA*, **12**, 1197

D’Onghia, E., Springel, V., Hernquist, L., & Keres, D. 2010, *ApJ*, **709**, 1138

D’Souza, R., & Bell, E. F. 2018, *MNRAS*, **474**, 5300

Das, P., & Binney, J. 2016, *MNRAS*, **460**, 1725

Das, P., Williams, A., & Binney, J. 2016, *MNRAS*, **463**, 3169

de Boer, T. J. L., Belokurov, V., & Koposov, S. 2015, *MNRAS*, **451**, 3489

De Silva, G. M., Freeman, K. C., Bland-Hawthorn, J., et al. 2015, *MNRAS*, **449**, 2604

Deason, A. J., Belokurov, V., & Evans, N. W. 2011, *MNRAS*, **416**, 2903

Deason, A. J., Belokurov, V., Evans, N. W., & Johnston, K. V. 2013, *ApJ*, **763**, 113

Deason, A. J., Belokurov, V., Koposov, S. E., & Lancaster, L. 2018, *ApJL*, **862**, L1

Deason, A. J., Belokurov, V., Koposov, S. E., & Rockosi, C. M. 2014, *ApJ*, **787**, 30

Deason, A. J., Belokurov, V., & Sanders, J. L. 2019, *MNRAS*, **490**, 3426

Deason, A. J., Belokurov, V., & Weisz, D. R. 2015, *MNRAS*, **448**, L77

Deason, A. J., Mao, Y.-Y., & Wechsler, R. H. 2016, *ApJ*, **821**, 5

Dehnen, W., & Binney, J. J. 1998, *MNRAS*, **298**, 387

Di Matteo, P., Haywood, M., Lehnert, M. D., et al. 2019, *A&A*, **632**, A4

Dierickx, M. I. P., & Loeb, A. 2017, *ApJ*, **836**, 92

Diermond, J. R., & Prince, P. J. 1978, *CeMec*, **18**, 223

Drimmel, R., & Poggio, E. 2018, *RNAAS*, **2**, 210

Edvardsson, B., Andersen, J., Gustafsson, B., et al. 1993, *A&A*, **500**, 391

Eggen, O. J., Lynden-Bell, D., & Sandage, A. R. 1962, *ApJ*, **136**, 748

Elias, L. M., Sales, L. V., Helmi, A., & Hernquist, L. 2020, *MNRAS*, **495**, 29

Evans, N. W. 2020, arXiv:2002.05740

Everall, A., & Das, P. 2020, *MNRAS*, **493**, 2042

Fardal, M. A., van der Marel, R. P., Law, D. R., et al. 2019, *MNRAS*, **483**, 4724

Fattahi, A., Deason, A. J., Frenk, C. S., et al. 2020, *MNRAS*, **497**, 4459

Fernández-Alvar, E., Carigi, L., Schuster, W. J., et al. 2018, *ApJ*, **852**, 50

Fernández-Trincado, J. G., Beers, T. C., Placco, V. M., et al. 2019, *ApJL*, **886**, L8

Feuillet, D. K., Feltzing, S., Sahlholdt, C., & Casagrande, L. 2020, arXiv:2003.11039

Flewelling, H. A., Magnier, E. A., Chambers, K. C., et al. 2016, arXiv:1612.05243

Font, A. S., Johnston, K. V., Bullock, J. S., & Robertson, B. E. 2006, *ApJ*, **638**, 585

Font, A. S., McCarthy, I. G., Crain, R. A., et al. 2011, *MNRAS*, **416**, 2802

Font, A. S., McCarthy, I. G., Poole-Mckenzie, R., et al. 2020, arXiv:2004.09194

Forbes, D. A. 2020, *MNRAS*, **493**, 847

Forbes, D. A., & Bridges, T. 2010, *MNRAS*, **404**, 1203

Fraix-Burnet, D., & Davoust, E. 2015, *MNRAS*, **450**, 3431

Frebel, A., Simon, J. D., Geha, M., & Willman, B. 2010, *ApJ*, **708**, 560

Freeman, K., & Bland-Hawthorn, J. 2002, *ARA&A*, **40**, 487

Fuhrmann, K. 1998, *A&A*, **338**, 161

Gaia Collaboration, Brown, A. G. A., Vallenari, A., et al. 2018, *A&A*, **616**, A1

Gaia Collaboration, Prusti, T., de Bruijne, J. H. J., et al. 2016, *A&A*, **595**, A1

Gallart, C., Bernard, E. J., Brook, C. B., et al. 2019, *NatAs*, **3**, 932

Gibbons, S. L. J., Belokurov, V., & Evans, N. W. 2017, *MNRAS*, **464**, 794

Gnedin, O. Y., & Ostriker, J. P. 1997, *ApJ*, **474**, 223

Gómez, F. A., Grand, R. J. J., Monachesi, A., et al. 2017, *MNRAS*, **472**, 3722

Gómez, F. A., Helmi, A., Brown, A. G. A., & Li, Y.-S. 2010, *MNRAS*, **408**, 935

Gómez, F. A., Helmi, A., Cooper, A. P., et al. 2013, *MNRAS*, **436**, 3602

Gravity Collaboration, Abuter, R., Amorim, A., et al. 2019, *A&A*, **625**, L10

Grillmair, C. J., & Dionatos, O. 2006, *ApJL*, **643**, L17

Hanke, M., Koch, A., Prudil, Z., Grebel, E. K., & Bastian, U. 2020, *A&A*, **637**, A98

Hayes, C. R., Majewski, S. R., Hasselquist, S., et al. 2020, *ApJ*, **889**, 63

Haywood, M., Di Matteo, P., Lehnert, M. D., et al. 2018, *ApJ*, **863**, 113

Helmi, A. 2020, arXiv:2002.04340

Helmi, A., Babusiaux, C., Koppelman, H. H., et al. 2018, *Natur*, **563**, 85

Helmi, A., & de Zeeuw, P. T. 2000, *MNRAS*, **319**, 657

Helmi, A., Veljanoski, J., Breddels, M. A., Tian, H., & Sales, L. V. 2017, *A&A*, **598**, A58

Helmi, A., White, S. D. M., de Zeeuw, P. T., & Zhao, H. 1999, *Natur*, **402**, 53

Hernitschek, N., Sesar, B., Rix, H.-W., et al. 2017, *ApJ*, **850**, 96

Hernquist, L. 1990, *ApJ*, **356**, 359

Hunter, J. D. 2007, *CSE*, **9**, 90

Ibata, R. A., Gilmore, G., & Irwin, M. J. 1994, *Natur*, **370**, 194

Iorio, G., & Belokurov, V. 2019, *MNRAS*, **482**, 3868

Ivezić, Ž, Sesar, B., Jurić, M., et al. 2008, *ApJ*, **684**, 287

Janesh, W., Morrison, H. L., Ma, Z., et al. 2016, *ApJ*, **816**, 80

Jean-Baptiste, I., Di Matteo, P., Haywood, M., et al. 2017, *A&A*, **604**, A106

Johnson, B. D., Conroy, C., Naidu, R. P., et al. 2020, *ApJ*, in press (arXiv: 2007.14408)

Johnston, K. V., Spergel, D. N., & Hernquist, L. 1995, *ApJ*, **451**, 598

Kafle, P. R., Sharma, S., Lewis, G. F., & Bland-Hawthorn, J. 2012, *ApJ*, **761**, 98

Kipper, R., Tenjes, P., Tuvikene, T., Ganeshaiyah Veena, P., & Tempel, E. 2020, *MNRAS*, **494**, 3358

Kirby, E. N., Cohen, J. G., Guhathakurta, P., et al. 2013, *ApJ*, **779**, 102

Kirby, E. N., Lanfranchi, G. A., Simon, J. D., Cohen, J. G., & Guhathakurta, P. 2011, *ApJ*, **727**, 78

Kluyver, T., Ragan-Kelley, B., Pérez, F., et al. 2016, in *Positioning and Power in Academic Publishing: Players, Agents and Agendas*, ed. F. Loizides & B. Schmidt (Amsterdam: IOS Press), 87

Koch, A., Grebel, E. K., & Martell, S. L. 2019, *A&A*, **625**, A75

Koposov, S., de Jong, J. T. A., Belokurov, V., et al. 2007, *ApJ*, **669**, 337

Koppelman, H., Helmi, A., & Veljanoski, J. 2018, *ApJL*, **860**, L11

Koppelman, H. H., & Helmi, A. 2020, arXiv:2004.07328

Koppelman, H. H., Helmi, A., Massari, D., Price-Whelan, A. M., & Starkenburg, T. K. 2019a, *A&A*, **631**, L9

Koppelman, H. H., Helmi, A., Massari, D., Roelenga, S., & Bastian, U. 2019b, *A&A*, **625**, A5

Kroupa, P. 2001, *MNRAS*, **322**, 231

Kruijssen, J. M. D., Pfeffer, J. L., Chevance, M., et al. 2020, arXiv:2003.01119

Kruijssen, J. M. D., Pfeffer, J. L., Reina-Campos, M., Crain, R. A., & Bastian, N. 2019, *MNRAS*, **486**, 3180

Lancaster, L., Koposov, S. E., Belokurov, V., Evans, N. W., & Deason, A. J. 2019, *MNRAS*, **486**, 378

Laporte, C. F. P., Johnston, K. V., Gómez, F. A., Garavito-Camargo, N., & Besla, G. 2018, *MNRAS*, **481**, 286

Law, D. R., Johnston, K. V., & Majewski, S. R. 2005, *ApJ*, **619**, 807

Law, D. R., & Majewski, S. R. 2010, *ApJ*, **714**, 229

Lee, D. M., Johnston, K. V., Sen, B., & Jessop, W. 2015, *ApJ*, **802**, 48

Leja, J., Carnall, A. C., Johnson, B. D., Conroy, C., & Speagle, J. S. 2019, *ApJ*, **876**, 3

Li, J., FELLOW, L., Liu, C., et al. 2019, *ApJ*, **874**, 138

Li, T. S., Sheffield, A. A., Johnston, K. V., et al. 2017, *ApJ*, **844**, 74

Lian, J., Thomas, D., Maraston, C., et al. 2020, arXiv:2003.11549

Lilleengen, S., Trick, W., & van de Ven, G. 2020, in IAU Symp. 353, Galactic Dynamics in the Era of Large Surveys, ed. M. Valluri & J. A. Sellwood (Cambridge: Cambridge Univ. Press), 266

Liu, S., Du, C., Newberg, H. J., et al. 2018, *ApJ*, **862**, 163

Lynden-Bell, D. 1975, *VA*, **19**, 299

Ma, X., Hopkins, P. F., Faucher-Giguère, C.-A., et al. 2016a, *MNRAS*, **456**, 2140

Ma, X., Hopkins, P. F., Kasen, D., et al. 2016b, *MNRAS*, **459**, 3614

Mackereth, J. T., & Bovy, J. 2020, *MNRAS*, **492**, 3631

Mackereth, J. T., Bovy, J., Schiavon, R. P., et al. 2017, *MNRAS*, **471**, 3057

Mackereth, J. T., Schiavon, R. P., Pfeffer, J., et al. 2019, *MNRAS*, **482**, 3426

Maffione, N. P., Gómez, F. A., Cincotta, P. M., et al. 2015, *MNRAS*, **453**, 2830

Maffione, N. P., Gómez, F. A., Cincotta, P. M., et al. 2018, *MNRAS*, **478**, 4052

Maiolino, R., & Mannucci, F. 2019, *A&ARv*, **27**, 3

Majewski, S. R., Schiavon, R. P., Frinchaboy, P. M., et al. 2017, *AJ*, **154**, 94

Majewski, S. R., Skrutskie, M. F., Weinberg, M. D., & Ostheimer, J. C. 2003, *ApJ*, **599**, 1082

Malhan, K., Ibata, R. A., & Martin, N. F. 2018, *MNRAS*, **481**, 3442

Martell, S. L., Shetrone, M. D., Lucatello, S., et al. 2016, *ApJ*, **825**, 146

Martell, S. L., Smolinski, J. P., Beers, T. C., & Grebel, E. K. 2011, *A&A*, **534**, A136

Massari, D., Koppelman, H. H., & Helmi, A. 2019, *A&A*, **630**, L4

Masseron, T., & Hawkins, K. 2017, *A&A*, **597**, L3

Matsuno, T., Aoki, W., & Suda, T. 2019, *ApJL*, **874**, L35

Matteucci, F., & Greggio, L. 1986, *A&A*, **154**, 279

McMillan, P. J. 2017, *MNRAS*, **465**, 76

Mestre, M., Llinares, C., & Carpintero, D. D. 2020, *MNRAS*, **492**, 4398

Miyamoto, M., & Nagai, R. 1975, *PASJ*, **27**, 533

Monachesi, A., Gómez, F. A., Grand, R. J. J., et al. 2019, *MNRAS*, **485**, 2589

Monaco, L., Bellazzini, M., Bonifacio, P., et al. 2007, *A&A*, **464**, 201

Monty, S., Venn, K. A., Lane, J. M. M., Lokhorst, D., & Yong, D. 2019, arXiv:1909.11969

Myeong, G. C., Evans, N. W., Belokurov, V., Amorisco, N. C., & Koposov, S. E. 2018a, *MNRAS*, **475**, 1537

Myeong, G. C., Evans, N. W., Belokurov, V., Sanders, J. L., & Koposov, S. E. 2018b, *ApJL*, **863**, L28

Myeong, G. C., Evans, N. W., Belokurov, V., Sanders, J. L., & Koposov, S. E. 2018c, *MNRAS*, **478**, 5449

Myeong, G. C., Evans, N. W., Belokurov, V., Sanders, J. L., & Koposov, S. E. 2018d, *ApJL*, **856**, L26

Myeong, G. C., Jerjen, H., Mackey, D., & Da Costa, G. S. 2017, *ApJL*, **840**, L25

Myeong, G. C., Vasiliev, E., Iorio, G., Evans, N. W., & Belokurov, V. 2019, *MNRAS*, **488**, 1235

Naidu, R. P., Tacchella, S., Mason, C. A., et al. 2020, *ApJ*, **892**, 109

Navarro, J. F., Frenk, C. S., & White, S. D. M. 1997, *ApJ*, **490**, 493

Necib, L., Ostdiek, B., Lisanti, M., et al. 2020, *NatAs*, **tmp**, 137

Newberg, H. J., Yanny, B., Grebel, E. K., et al. 2003, *ApJL*, **596**, L191

Newberg, H. J., Yanny, B., Rockosi, C., et al. 2002, *ApJ*, **569**, 245

Niederste-Ostholt, M., Belokurov, V., Evans, N. W., et al. 2010, *MNRAS*, **408**, L66

Norris, J. E., & Ryan, S. G. 1989, *ApJL*, **336**, L17

Oke, J. B., & Gunn, J. E. 1983, *ApJ*, **266**, 713

Oliphant, T. 2006, NumPy: A Guide to NumPy (USA: Trelgol Publishing), <http://www.numpy.org/>

Ostdiek, B., Necib, L., Cohen, T., et al. 2020, *A&A*, **636**, A75

Pearson, S., Price-Whelan, A. M., & Johnston, K. V. 2017, *NatAs*, **1**, 633

Pérez, F., & Granger, B. E. 2007, *CSE*, **9**, 21

Pfeffer, J. L., Trujillo-Gomez, S., Kruijssen, J. M. D., et al. 2020, arXiv:2003.00076

Pillepich, A., Madau, P., & Mayer, L. 2015, *ApJ*, **799**, 184

Pillepich, A., Nelson, D., Hernquist, L., et al. 2018, *MNRAS*, **475**, 648

Price-Whelan, A. M., Sipocz, B., Major, S., & Oh, S. 2017, *adrn/gala*: v0.2.1, Zenodo, doi:10.5281/zenodo.833339

Price-Whelan, A. M. 2017, *JOS*, **2**, 388

Price-Whelan, A. M., Johnston, K. V., Sheffield, A. A., Laporte, C. F. P., & Sesar, B. 2015, *MNRAS*, **452**, 676

Price-Whelan, A. M., Johnston, K. V., Valluri, M., et al. 2016a, *MNRAS*, **455**, 1079

Price-Whelan, A. M., Sesar, B., Johnston, K. V., & Rix, H.-W. 2016b, *ApJ*, **824**, 104

Purcell, C. W., Bullock, J. S., & Kazantzidis, S. 2010, *MNRAS*, **404**, 1711

Queiroz, A. B. A., Anders, F., Chiappini, C., et al. 2020, *A&A*, **638**, A76

Quinn, P. J., & Goodman, J. 1986, *ApJ*, **309**, 472

Reina-Campos, M., Hughes, M. E., Kruijssen, J. M. D., et al. 2020, *MNRAS*, **493**, 3422

Robertson, B., Bullock, J. S., Font, A. S., Johnston, K. V., & Hernquist, L. 2005, *ApJ*, **632**, 872

Rosenberg, A., Piotto, G., Saviane, I., Aparicio, A., & Gratton, R. 1998, *AJ*, **115**, 658

Ruiz-Lara, T., Gallart, C., Bernard, E. J., & Cassisi, S. 2020, *NatAs*, **tmp**, 111

Sahlholdt, C. L., Casagrande, L., & Feltzing, S. 2019, *ApJL*, **881**, L10

Sakari, C. M., Venn, K. A., Irwin, M., et al. 2011, *ApJ*, **740**, 106

Sanders, J. L., & Binney, J. 2016, *MNRAS*, **457**, 2107

Sanders, J. L., & Das, P. 2018, *MNRAS*, **481**, 4093

Sanders, R. L., Shapley, A. E., Kriek, M., et al. 2015, *ApJ*, **799**, 138

Sanderson, R. E., Helmi, A., & Hogg, D. W. 2015, *ApJ*, **801**, 98

Santistevan, I. B., Wetzel, A., El-Badry, K., et al. 2020, arXiv:2001.03178

Sarajedini, V. L., Koo, D. C., Klesman, A. J., et al. 2011, *ApJ*, **731**, 97

Schaerer, D., & Charbonnel, C. 2011, *MNRAS*, **413**, 2297

Schiavon, R. P., Zamora, O., Carrera, R., et al. 2017, *MNRAS*, **465**, 501

Schlafman, K. C., Rockosi, C. M., Lee, Y. S., et al. 2012, *ApJ*, **749**, 77

Schönrich, R., Asplund, M., & Casagrande, L. 2011, *MNRAS*, **415**, 3807

Searle, L., & Zinn, R. 1978, *ApJ*, **225**, 357

Sesar, B., Hernitschek, N., Dierckx, M. I. P., Fardal, M. A., & Rix, H.-W. 2017a, *ApJL*, **844**, L4

Sesar, B., Hernitschek, N., Mitrović, S., et al. 2017b, *AJ*, **153**, 204

Sesar, B., Jurić, M., & Ivezić, Ž. 2011, *ApJ*, **731**, 4

Sharma, S., Bland-Hawthorn, J., Johnston, K. V., & Binney, J. 2011, *ApJ*, **730**, 3

Shipp, N., Drlica-Wagner, A., Balbinot, E., et al. 2018, *ApJ*, **862**, 114

Siegel, M. H., Dotter, A., Majewski, S. R., et al. 2007, *ApJL*, **667**, L57

Simpson, C. M., Gargiulo, I., Gómez, F. A., et al. 2019, *MNRAS*, **490**, L32

Simpson, J. D., & Martell, S. L. 2019, *MNRAS*, **490**, 741

Speagle, J. S. 2019, arXiv:1904.02180

Starkenburg, E., Helmi, A., Morrison, H. L., et al. 2009, *ApJ*, **698**, 567

Steidel, C. C., Rudie, G. C., Strom, A. L., et al. 2014, *ApJ*, **795**, 165

Steidel, C. C., Strom, A. L., Pettini, M., et al. 2016, *ApJ*, **826**, 159

Steinmetz, M., Zwitter, T., Siebert, A., et al. 2006, *AJ*, **132**, 1645

Stonkutė, E., Koposov, S. E., Howes, L. M., et al. 2016, *MNRAS*, **460**, 1131

Ting, Y.-S., & Rix, H.-W. 2019, *ApJ*, **878**, 21

Tinsley, B. M. 1980, *FCPh*, **5**, 287

Tissera, P. B., Beers, T. C., Carollo, D., & Scannapieco, C. 2014, *MNRAS*, **439**, 3128

Torrey, P., Vogelsberger, M., Marinacci, F., et al. 2019, *MNRAS*, **484**, 5587

van den Bergh, S., & Mackey, A. D. 2004, *MNRAS*, **354**, 713

Vasiliev, E. 2019, *MNRAS*, **484**, 2832

Venn, K. A., Irwin, M., Shetrone, M. D., et al. 2004, *AJ*, **128**, 1177

Vickers, J. J., & Smith, M. C. 2018, *ApJ*, **860**, 91

Vincenzo, F., Spitoni, E., Calura, F., et al. 2019, *MNRAS*, **487**, L47

Virtanen, P., Gommers, R., Oliphant, T. E., et al. 2020, *NatMe*, **17**, 261

Weisz, D. R., Dolphin, A. E., Skillman, E. D., et al. 2014, *ApJ*, **789**, 148

Woolley, R. V. D. R. 1957, *MNRAS*, **117**, 198

Xue, X.-X., Rix, H.-W., Ma, Z., et al. 2015, *ApJ*, **809**, 144

Xue, Y. Q., Luo, B., Brandt, W. N., et al. 2011, *ApJS*, **195**, 10

Yang, C., Xue, X.-X., Li, J., et al. 2019, *ApJ*, **886**, 154

Yanny, B., Rockosi, C., Newberg, H. J., et al. 2009, *AJ*, **137**, 4377

Yu, S., Bullock, J. S., Wetzel, A., et al. 2020, *MNRAS*, **494**, 1539

Yuan, Z., Chang, J., Banerjee, P., et al. 2018, *ApJ*, **863**, 26

Yuan, Z., Chang, J., Beers, T. C., & Huang, Y. 2020a, [ApJL](#), **898**, L37
Yuan, Z., Myeong, G. C., Beers, T. C., et al. 2020b, [ApJ](#), **891**, 39
Zahid, H. J., Dima, G. I., Kudritzki, R.-P., et al. 2014, [ApJ](#), **791**, 130

Zaritsky, D., Conroy, C., Zhang, H., et al. 2020, [ApJ](#), **888**, 114
Zolotov, A., Willman, B., Brooks, A. M., et al. 2009, [ApJ](#), **702**, 1058
Zuo, W., Du, C., Jing, Y., et al. 2017, [ApJ](#), **841**, 59